POWER ELECTRONICS TOPOLOGIES

FOR SOLAR PHOTOVOLTIAC ENERGY SYSTEM APPLICATIONS

A Dissertation

by

SINAN ASAAD SABEEH

Submitted to the Office of Graduate and Professional Studies of
Texas A&M University
in partial fulfillment of the requirements for the degree of

DOCTOR OF PHILOSOPHY

Chair of Committee, Prasad N. Enjeti
Committee Members, Mehrdad Ehsani
 Christi Madsen
 Rabi Mohtar
Head of Department, Miroslav M. Begovic

December 2018

Major Subject: Electrical Engineering

ABSTRACT

Owing to economic aspects, Central inverter is the dominating candidate in large-scale PV installations despite its lower energy harvest compared to other topologies like string inverters especially under partial shading conditions. This dissertation focuses on developing a new fractional rated converter to harvest maximum power point from PV systems for different environmental conditions e.g. dust, temperature, and shading effects. The first approach emphasizes on balancing the voltages from different strings in a PV farm and ensure higher energy yield from central inverters. The voltage approach balancing has a higher efficiency and energy density at lower cost. A new MPPT algorithm has been designed and tested through simulation to conform the functionality of the proposed topology.

The second approach is an extension to voltage balancing topology to develop based on it a complete energy harvesting system that balances the voltage and current from the non-linear source which is the PV. The two-stage converter characterized by the fractional power rating, high efficiency, scalability and lower cost of the energy produced. The approach is designed for PV strings with voltage of 1500V DC to achieve maximum power point tracking (MPPT) through the fractionally rated stages mitigating the effects of environmental conditions. The proposed system is shown to be scalable to suite large-scale solar PV power plants. A design example of 1.1 MW PV power and lab-prototype of 400 W has been built to validate the proposed concept.

The third part theme investigated a dual phase output inverter actively decouples the double line frequency harmonics integrated with power optimizer. The inverter employs a half bridge with passive elements (L-C) to balance the output to actively decouple the double line frequency. The closed loop control adjusts for varying load conditions. Further, an integrated power optimizer (PO) provides interface of solar-pv and battery to the dc-link. The PO stage (half bridge) is

controlled such that maximum power point tracking (MPPT) is achieved for the connected pv-array and independent charge/discharge functions of the battery. Simulation and experimental results verify the performance of the proposed technique under balanced, unbalanced load, non-linear conditions as well as fault condition.

DEDICATION

I dedicate this work to almighty Allah whom without Allah blessings this work would not have

been possible.

ACKNOWLEDGEMENTS

CONTRIBUTORS AND FUNDING SOURCES

TABLE OF CONTENTS

LIST OF FIGURES

LIST OF TABLES

I.   INTRODUCTION

The global trend of shifting from using fossil fuels to alternative sources of energy to produce electricity puts a lot of pressure on the science community to explore different options that will facilitate the integration of renewable energy with the gird. In 2010 only 0.1% of the United States' electricity supplied by solar energy. The U.S department of Energy recognized the urgency of addressing the future demands of energy and created the SunShot Initiative to reduce price of kW/hr/$ produced by photovoltaic (PV) energy systems. The initiative achieved 85% from its solar cost target goal by 2020 for residential-scale and residential-scale applications. In 2017, National Renewable Energy Laboratory (NREL) reports confirm the price of electricity produced from solar energy dropped as low as 9.2-6.1 cents a kWh for commercial systems, 5.0-6.6 cents a kWh for utility-scale fixed-tilt systems, and 4.4-6.1 cents a kWh for utility-scale one-axis tracking systems[2] as presented in Figure. 1.
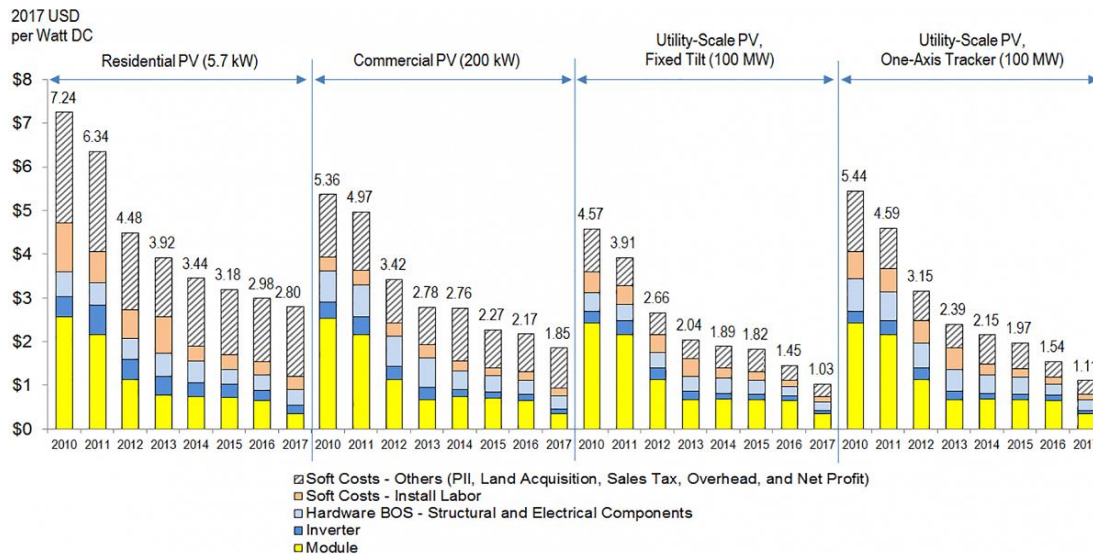
Figure. 1 The trend of PV system prices for residential, commercial, and utility scale [2] (© 2018 – Adapted with permission Fraunhofer Institute for Solar Energy Systems)

1

The advancement of energy harvesting technologies considered the main factor behind the price drop of the PV systems. The energy harvesting part within the PV system consist of energy production, which is the PV module and the inverter side. The field of power electronics focus on the advancement of the energy harvesting by operating the system at lower cost and higher efficiency. Thus, power electronics plays a vital role in the future of energy sector since power converters process the power from solar to electric and further interfaces with the electric grid.

1.1 Applications Involving Utility Interface

The utility interface has become an essential part of the grid. Today there are several applications are directly connected with the grid such as the Electric Vehicles (EV), Solar Power Plants, Wind Turbine Farms, Data Centers, Battery storage units…etc as shown in Figure.2 All of these applications interfere with the grid dynamically and it requires complex control mechanisms to handle multiple loads and multiple generation points. All these points of interfaces should match the grid standards according to the IEEE 1547 for grid-connected applications where inverters should comply.
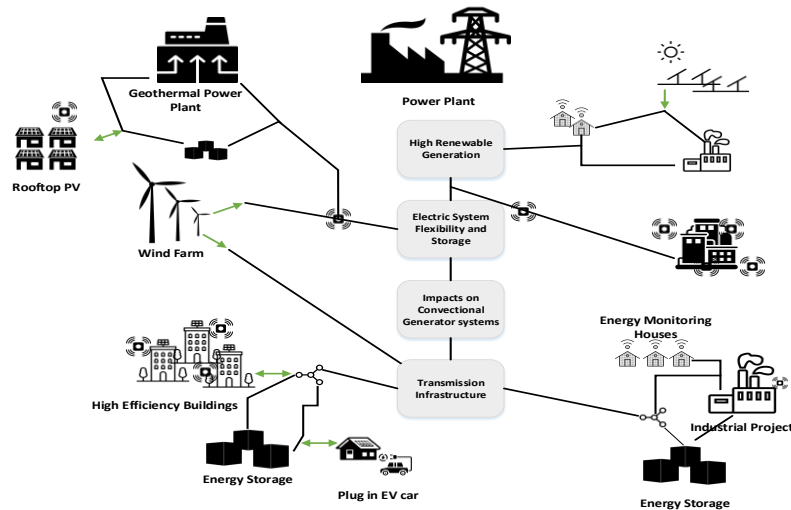
Figure. 2 An Overview picture of the grid connected systems [1] (© 2017-Reprinted with permission from NERL).

Designing a dynamic grid with multiple generation points or loads introduce new types of challenges. The level of reliability and power quality is distinctive based on the load classification and service differentiation for multiple users of the gird. Problems like demand for peak shaving, grid isolation, and independent mode of operation must be dealt with in real time. Therefore, restructuring the electricity network system is a necessity, which it could be done through introducing distributed energy resources (DER) to deal with renewable energy sources (RES).

1.2 PV Systems

1.2.1   Photovoltaic Cells

Photovoltaic (PV) cells are the smallest component in PV systems where the solar energy (light) converted to electricity. PV cells are semiconductor devices made with pure silicon or doped with other materials. The classifications of the PV cells are monocrystalline, polycrystalline, and thin film. Each type of PV panels has an energy efficiency for its solar energy conversion rate as presented in Figure. 3. It shows n-type semiconductors HJT/IBC has the highest energy efficiencies in comparison to other types. However, the multi-Si PV types are dominating the commercial PV market according to the [31] as shown in Figure. 4.
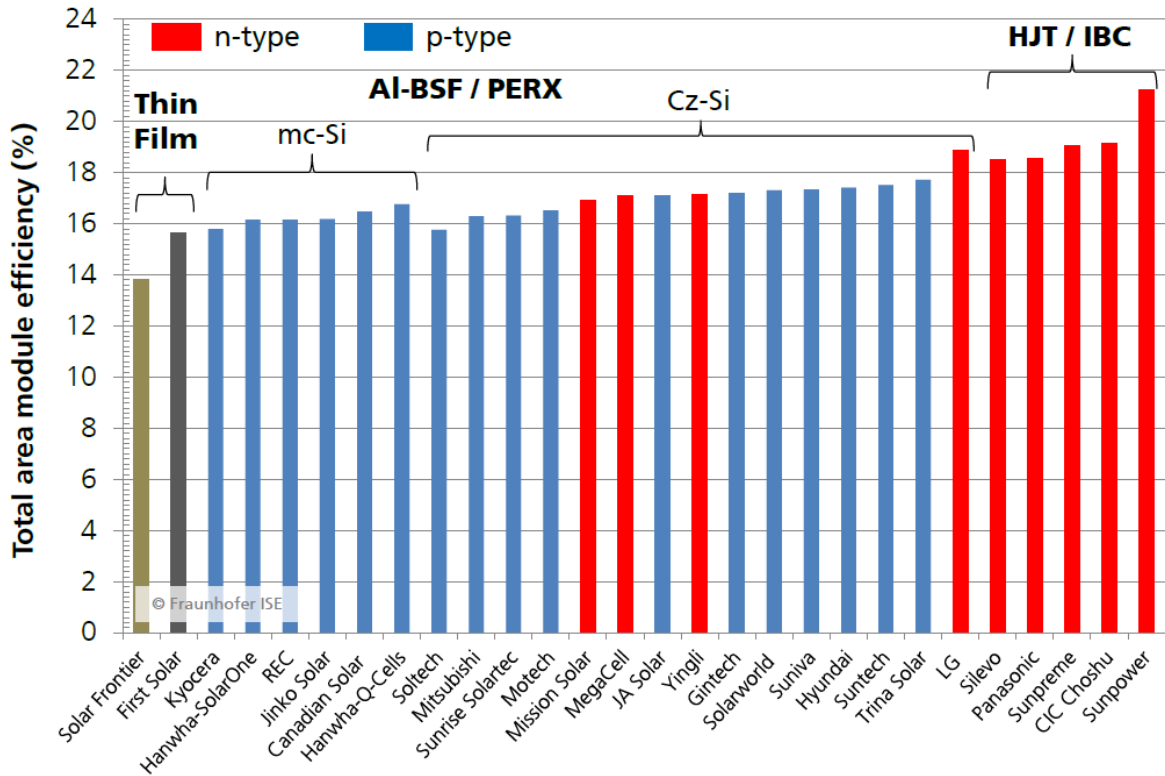
Figure. 3 Current energy conversion efficiencies of selected PV commercial modules [2] (© 2018 – Adapted with permission Fraunhofer Institute for Solar Energy Systems)
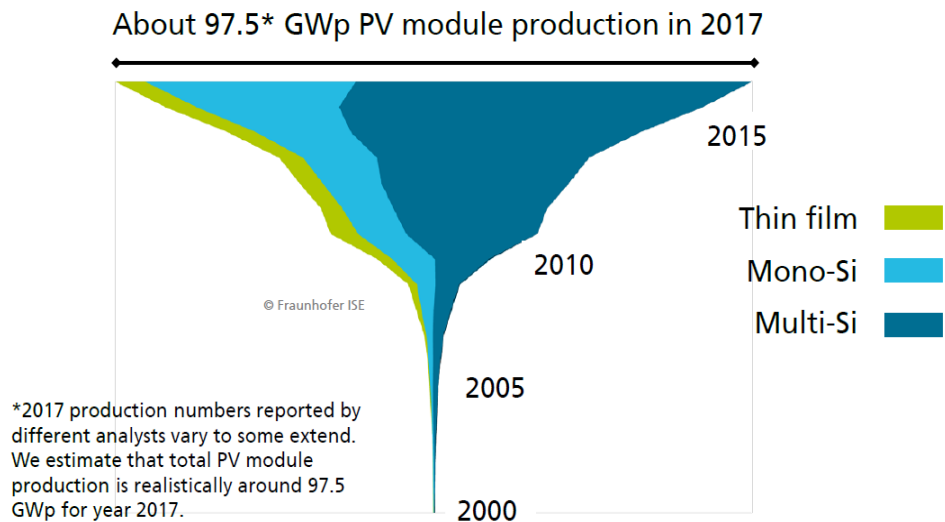
Figure. 4 Global PV module power produced from different materials[2] (© 2018 – Adapted with permission Fraunhofer Institute for Solar Energy Systems).

1.2.2 PV system sizing

There are several types of PV systems that are grid-connected and isolated systems. Each of the systems can have their own power scales. A system that is less than 50kW power rating is considered small scale, and system that has considered larger than 1 MW is considered either large scale or utility scale system. Systems that are in between 50kW and 1 MW are classified as intermediate scale .A PV system can be qualified as large-scale PV system by having accumulated small groups of PV system that add up to 1MW PV system. Most of the inverter design of large-scale systems are rated for less than 1 MW capacity[4].

The grid-connected systems can have an energy storage unit as battery that can be utilized in either standalone conditions or grid-connected mode. Having distributed energy storage units with PV systems help with building virtual power plants that can contribute to the gird reliability and address power surges to meet the demands of the future grid [3,31].

The recent PV system classifications focuses on the voltage level of the point of common coupling (PCC). However, a unity power factor still stays a challenge in most system designs, which is required at the PCC. Recent development of the PV systems enabled achieving higher string rating of 1500V directly interfaced with the inverter [7,38], which will be explored later in this work, which enables medium-voltage networks. Regardless of the size of the designed PV system, the system is controlled by MPPT algorithm that ensures optimum power is harvested for different environmental conditions. There are two types of MPPT classification for PV systems either centralized or distributed as presented in Figure. 5 [3, 4, 5,31].

Centralized MPPT
- Galvanic Isolation
  - Three Stage Conversion
  - Two-Stage Conversion
  - Single-Stage Conversion
- Non-Isolation
  - Two-Stage Conversion
  - Single-Stage Conversion

Distributed MPPT
- Single Level
  - DC/DC
  - DC/AC
- Module Level
  - DC/DC
  - DC/AC
- Submodule Level
  - DC/DC
- Cell Level
  - DC/DC
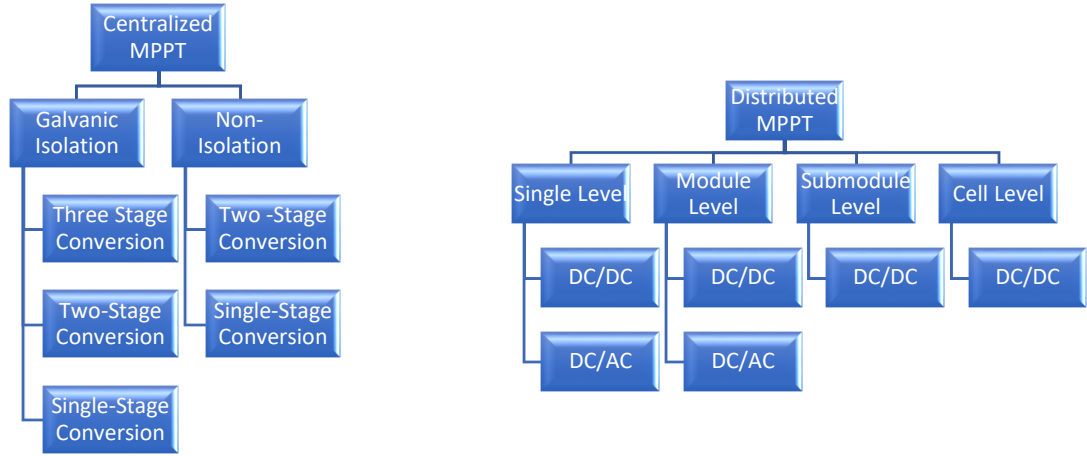
Figure. 5 Classification of grid-connected PV Power systems (a) Centralized MPPT (b) Distributed MPPT.

Figure. 5.(a) presents centralized type of maximum power point tracking techniques according to each type of converter. The galvanic isolation suits the gird tie applications and non-isolate CMMPT suits island applications. Designs tend to have an optimal number of stages in order to maximize the power density processed in a plant per square feet. As well as the fewer the number of stages the PV plan has the overall losses will be minimized. Figure. 5.(b) presents distributed approach of the maximum power point tracking techniques. The DMPPT operates either dependently or independently of each other depending on how many levels are involved or topology that is handling the PV plant energy harvesting. However, the DMPPT techniques are complicated and substantially increase the price of the produced kWh[31].

1.2.3 Types of Grid Tie PV Collection Topologies

Each PV plant has its own challenges from area, location, budget, etc... These challenges affect the overall design of the plant and the type of energy harvesting method that should be used. This section discusses several energy harvesting methods that has been used to harvest power from existing PV architectures. Figure. 6.(a) presents simple system where the energy is processed

6

through an inverter that has built-in MPPT. Although the system is simple; however, for large-scale applications, the system is not suitable because it needs large area due to the lack of storage systems on board. Figure. 6.b presents another system with battery storage which can provide a significant energy buffer. The presence of a battery enables the system operation either in gird-connected or standalone mode in case of power outage. The term standalone suggests an off-grid mode of operation. The battery can be fully utilized to supply critical loads at any time. During the grid-connected operation mode, the system can accommodate peak shaving effects or act as reactive power due to the existence of the energy storage. Despite Figure. 6.(b) presents a very flexible system; however, it's not optimum for commercial large-scale systems since a higher voltage output required to meet the medium voltage (MV) level. Figure. 6. (c) presents an energy harvesting stages where the voltage would be stepped up using a step-up transformer in spite of the transformer losses but the system is considered efficient for power transmission. In addition, this approach enables connecting hundreds of PV modules in series and parallel.

7

(c)
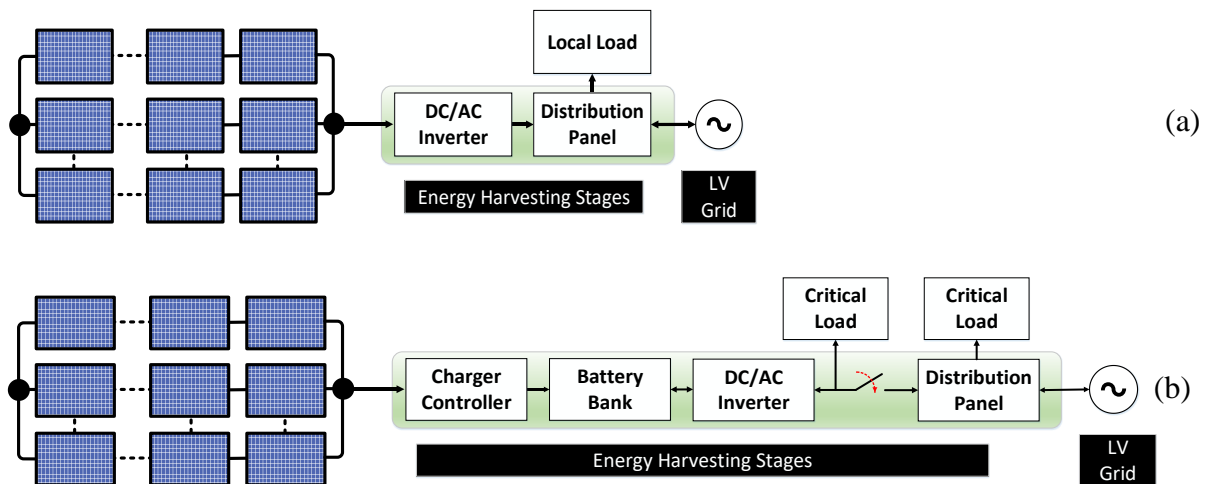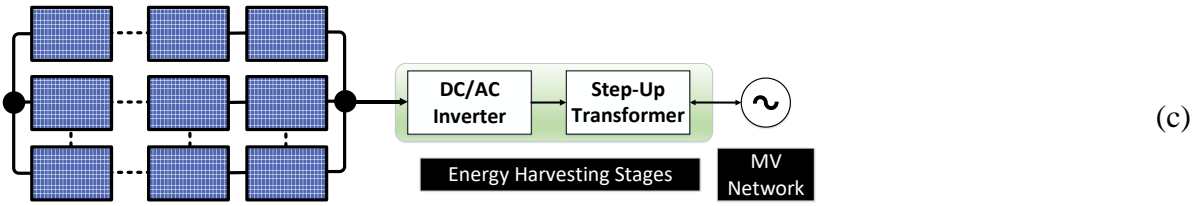
Figure. 6 Grid connected PV power systems with PV inverter and generator: (a) simple mode operation system, (b) grid-connected system with storage unit, (c) Large Scale PV

1.2.4 Types of MPPT Techniques

There are several techniques found in the literature suggests different types of maximum power point tacking (MPPT) methods. Brief description of each of these techniques is presented below:

1.2.4.1 Sampling method

From reading the past and current data of the PV system, the controller decides the tracking direction. The tracking process could be slow, and it might adjustments until maximum power point is achieved. There are several methods under this the sampling approach can be explored below:

1.2.4.1.1 Perturb and Observe Technique/Hill Climbing Technique

Many articles in the literature explore the perturb and observe (P&O) method and it's also called Hill Climbing (HC) but it depends on the nature of how the algorithm is doing the search mechanism. The algorithm relies on identifying the power difference between the current and past data point, thus it will direct the controller to keep iterating until it reaches the maximum available power. The main difference between P&O and HC is that the perturbation occurs on operating voltage and duty cycles of the converter respectively [6]. As it can be seen from Figure. 7 the power output conciliates between the left and right side of the P_{MPP} as the voltage changes. The

8

search algorithm of P&O and HC keeps tracking an accurate shift to harvest the maximum available power at all times. However, the problem of this approach, there might be minimal losses while oscillating around the P_{MPP} that dissipate in the form of heat. There would be a compromise between speed of the response to achieve the P_{MPP} and the step size of to avoid increasing losses. The method showed a poor response to drastic and sudden environmental changes[6, 7].
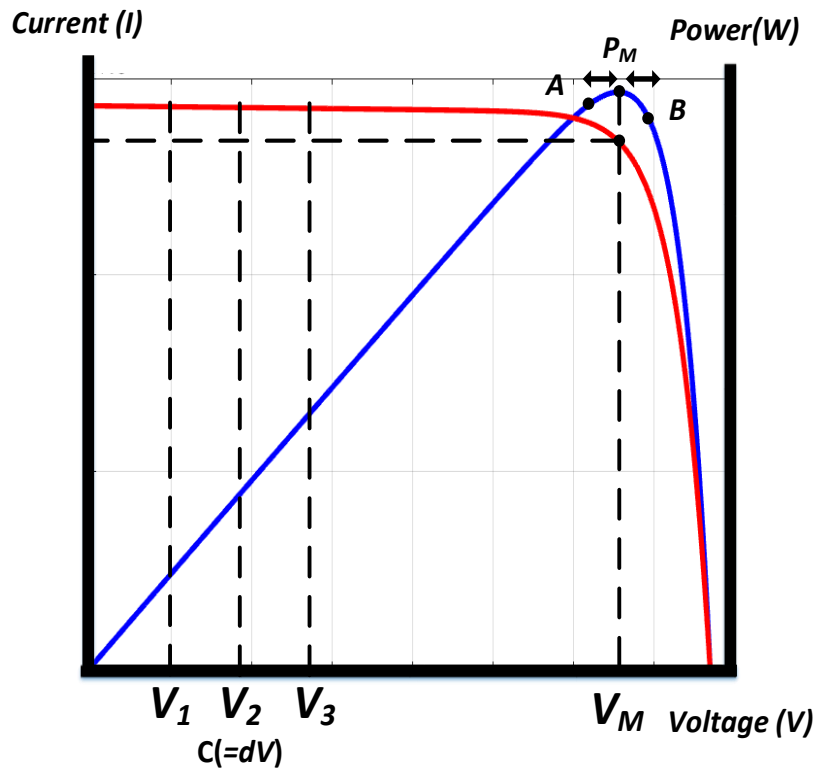
Figure. 7 Method of Perturb and Observe to track the MPP in PV systems

1.2.4.1.2   One Cycle Control (OCC) Technique

The method uses a switched variable where either current or voltage to force their average to a reference control. The reference control signal is generated based on the feedback from grid as well as to increase the maximum power extracted from the PV system[8]. The converter achieve balanced output current by regulating the PV system voltage. An advanced digital MPPT controller could be used with OCC to achieve less power oscillation and higher efficiency[6, 9, 10].

1.2.4.1.3 Differentiation Method

This method solves a group of differential equations to achieve MPPT for the PV system. The model used depends on the equivalent mathematical model of the PV system. The following equations represents the search problem:

$$\frac{dP}{dV} = \frac{d(VI)}{dV} = V\frac{dI}{dV} + I\frac{dV}{dV}$$

(1.1)

Either voltage or current can be adjusted in this method to achieve the maximum power point. The method requires complex calculations using digital signal process.

1.2.4.2 Incremental Conductance Method

The method has been explored by literature and it mainly focuses on varying the power. The voltage and current needed to be measured in real-time while the PV system operates. Once the conductance is achieved as show in Equation (1.2) then the incremental conductance is pursued. The MPP is achieved when the derivative of Equation 1.4 is zero and operation point is fixed[11].

$$G\frac{I_{PV}}{V_{PV}}$$

(1.2)

$$dG = \frac{dI_{PV}}{dV_{PV}}$$

(1.3)

$$\frac{dPpv}{dVpv} = 0$$

(1.4)

Once the current changes, the operation direction of MPP changes until MPP is achieved again as shown in Figure. 8 . The method showed its effectiveness to track the MPPT when the

environmental conditions changed quickly with minimal losses in comparison to the sampling methods.
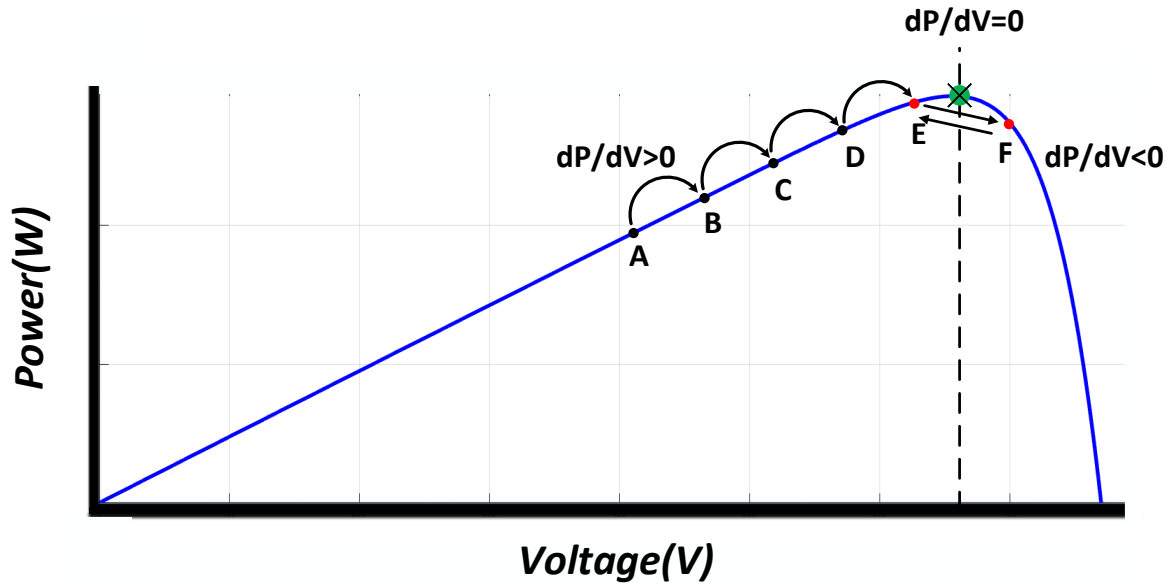
Figure. 8 MPPT technique of incremental conductance

1.3 Switching Devices

Since long time ago, Silicon (Si) has been the dominant semiconductor of choice for high voltage switching device. Due to the increased demands from industry to find a better performing devices that can handle higher current and voltage as well as able to process higher energy at smaller dimensions the Si-based devices reached their maximum industrial capacity. Therefore, wide-bandgap semiconductors, like Silicon Carbide (SiC) and Gallium Nitride (GaN) gained serious investigation from the industry in the field of power electronics. Wide-bandgap devices position themselves uniquely in the market due to their ability to handle high switching frequency, high operating temperature and higher blocking voltages[12, 13].

For the experimental work of this dissertation, two switching devices has been used to verify the concepts for laboratory small-scale systems. The selection of these switching devices was made base on several objectives: the required energy density, current industrial trends, switching frequency, and the power rating for the converter as shown in Figure. 9
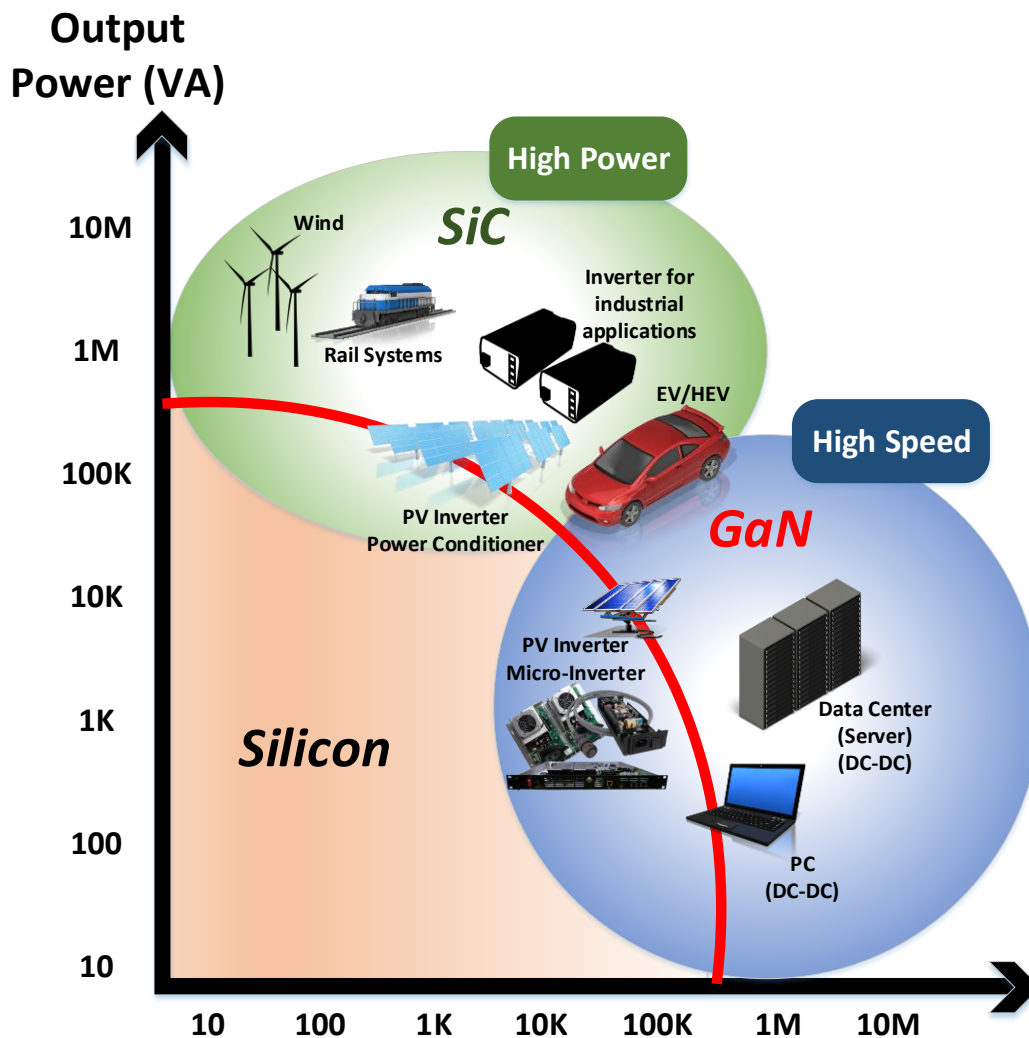
Figure. 9 Illustration of the possible industries that can utilize SiC,GaN or Si switching devices with their switching frequency and power boundaries[14] (© 2018 – Adapted with permission from IEEE).

1.4 Research Objective

The key is to find new ways of harvesting energy from renewable resources with minimal losses. Losses are generated due to different stages and processing the full power in each of the stages. The current industrial trends focuses developing the infrastructure renewable energy resources especially PV systems. PV has become the focus of many countries' R&D grants after the noticeable jump in energy conversion ratio from 15% to 22.5%, which means PV panels are able to produce 50% more kilowatt hours (kWh) of electricity under the same environmental conditions for the same area. In addition, advancing in power electronics enabled further to invest in the PV market and design new concepts that optimize energy harvesting at all times.

Since PV market is globally expanding and there is market need, this dissertation focuses on exploring new novel ways to harvesting solar energy by focusing on designing new circuit architectures that can manage high power processing, achieve high efficiency, minimize the losses through the stages, reliable systems and provide supply to end consumers.

In order to achieve these goals, we need to rethink the way energy harvested for PV systems. Therefore, this dissertation focuses on developing new topologies that use the most advance technologies in the market to address the future needs. The new energy harvesting system realizes maximum power point operation through fractionally rated converters by introducing passive elements (L-C) to balance string voltages and modules currents. The initial thought of the research started from developing a technique that can manage the power generated from different PV strings for a large-scale PV plant because existing solutions do not handle individual strings and the total power of the string will be lost. The new voltage-balancing converter increase the plant total power by switching between the strings such that each string would contribute to the total power harvested. This stage designed with fractional power from the total power produced

13

by the plant; therefore, the switch sizing and passive elements sizing would be small in comparison to the conventional systems thus the new fractional rated converter would reduce the overall design cost and produce higher energy yield.

The problem is not limited to voltage difference only between the different PV strings in a PV plant but the irradiance introduces current difference on the module level and that would limit the current following in the string to the lowest current available between the series connected modules. Therefore, the research theme needs to expand to address a wider problem and further optimize energy harvesting. Existing approaches do not count for the losses on the module level. In addition, there approaches are fully rated to harvest the available power; therefore, existing approaches are not the best commercially viable solution. Thus, there was a need to address both voltage and current differences between different PV strings to increase the total energy yield at a lower cost. The developed concept of two stage fractionally rated DC-DC converter manages the power between the strings and on the module level and each stage is fractionally rated from the total PV plant power. Having fractionally, rated approach distributed in the PV plant introduces a new way of maximizing energy harvest.

The second stage after optimizing the energy harvested from the PV systems, the inverter appears. The inverter plays a vital role in feeding loads and inverting the power from DC to AC. Existing solutions focuses on developing efficient central inverter with introducing any new dynamic approach to deal with different variables. Therefore, there is a need in coming with new approach that integrates with fractionally rated inverters. The existing inverter design works on integrating the fractionally rated current balancing stage with inverter. Due to the nature of switching devices, there is always an issue of double-line frequency power ripple generated. Mostly these power ripples are eliminated by throwing a huge DC-link capacitor, these capacitors

are bulky, and they introduce a reliability issue. Therefore, there is a need for a new system that can handle all of these variables. A new concept of dual phase output inverter designed with active decoupling that integrates with the current balancing stage for off-grid applications. The concept liberate existing inverter designs from many assumptions made and offers a wider range of operation.

1.5 Dissertation Outline

Section-I of the this dissertation presents the background information about photovoltaic systems, market size, current solutions, MPPT techniques used, and the current switching devices used in the industry. The section explores different types of MPPT and a general classification is done. As well as the section discusses the big picture of multi-generation point grid and shows how the different systems integrates to feed the gird.

Section-II focuses on the fractional rated DC-DC converter used for balancing the string voltages for large-scale PV system. The section provides in-depth analysis of the modeling equations used to derive the equations that controls the overall system. The MPPT technique used has been explored and analyzed. The designed fractional rated voltage balancing system was build using SiC switches based on the current industrial trends. The design was verified through simulation and experimental results.

Section-III is an extended work to Section-II where the voltage balancing stage is not enough to deal with different environmental conditions (irradiance and temperature); therefore, a new two stage fractional rated DC-DC converter is proposed. Section-III explores the two-stage fractional rated converter operation for different environmental conditions for homogenous PV power plant as well as heterogeneous PV power plant. This section introduces a new novel approach where a large-scale PV system can have different types of PV systems from different

15

manufactures. A full modeling equations, analysis, simulation and small-scale lab prototype using SiC switches is built to verify the approach.

To enable energy harvesting through PV systems, there is a need for designing an inverter. Therefore, section-IV explores a new dual-phase output 4-leg inverter with active decoupling that is integrated with power optimizer for off-grid applications. The inverter uses a half bridge with passive elements (L-C) to balance the output and actively decoupling the double line frequency power ripples in the DC-link. The inverter design includes a closed-loop control adjusts for varying load conditions (linear, non-linear, balanced, and non-balanced). Further, the integrated power optimizer works to handle the power between the battery and PV system to achieve extracting the maximum power operation points. The inverter operation is verified using simulation and experimental setup using GaN switching devices at high switching frequency.

Finally, Section V and Section VI present an overall conclusion, remarks obtained from this work and suggest future work.

II. APPLICATION-I: FRACTION POWER RATED MODULAR VOLTAGE BALANCING CONVERTER FOR LARGE SCALE PV PLANTS *

2.1 Introduction

One of the important technologies of solar energy is photovoltaic technology, which has become the fastest growing renewable energy. Continuous drop in PV panel cost followed by inverter cost has resulted in widespread deployment of large-scale PV power plants all over the world. According to the GTM research over 100 gigawatts of PV will be coming online during 2018. It is well known that minimizing number of conversion stages improves conversion efficiency as well as reduces the cost of the system. Conventional large-scale PV power systems are configured with 1000 V DC primarily due to safety[20] with a DC-AC central inverter followed by a step-up transformer interface to electric utility. Beginning 2012 PV manufactures enabled PV panels to be connected in series for 1500V DC[18,21,38,44]. The higher DC voltage contributes to reduced current and improves dc-bus utilization in the central inverter [22].

A conventional large-scale solar power plant consists of several series parallel connection arrangement of PV panels (Figure. 11.a , Figure. 11.c) with 1000V/1500V DC collection voltage [23, 24, 44]. The international electrotechnical commission (IEC) approved with new nominal voltage limit of 1500 V; this new voltage limit enabled further cost reduction and improvements to conversion efficiency[20].

_____

The terminal characteristics (I-V relation) of the overall series/parallel PV strings (Fig. 2.b) is nonlinear and influenced by the external environmental factors such as solar irradiance; temperature and partial shading due to cloud movement[26]. Figure. 11.b shows the I-V curve under uniform insolation and partially shaded conditions. It is clear that the I-V curve under partial shading is non-uniform. Further, the power vs voltage (P-V) curve depicts multiple peaks under shading conditions[27]. In addition to shading, temperature difference also plays vital role in power availability. The central inverter in Figure. 11.a is controlled to deliver the available power to the utility. It is clear from this arrangement (Figure. 11 a-b) the power harvested under partial shading conditions is much lower than the available power.

In order to improve energy harvesting efficiency, references [19,26-29] propose a multistring PV system (Figure. 11.c) arrangement that enables MPPT of each individual series connected string via a boost converter. Several commercial PV inverters that enable string MPPT control are now available [27]. This approach (Figure. 11.c) suffers from the following disadvantages: a) the volt-ampere (VA) rating of the boost converter is same as the PV string; b) the boost switch voltage rating is same as the string voltage rating (V_{string}); c) the efficiency of the boost converter is low under light load conditions.

In view of the above disadvantages, this section proposes a new fractional power rated modular voltage balancing converter topology. Figure. 10.a and Figure. 10.b shows the proposed approach suitable for adjusting individual string MPPT of a large-scale PV plant. Figure. 10.a, shows the proposed approach for two strings. The voltage rating of the required IGBTs (S1, S2) is equal to the voltage difference between the adjacent two strings (i.e. ΔV_{String}) which is low. Further, the proposed approach [41] only processes the difference in power between the strings to adjust individual string MPPT with the PWM control. In addition, the required capacitance (Cb)

is small and film type capacitors can be employed. Additionally, under fault condition, the switching IGBTs can be bypassed to restore parallel operation of the PV stings to resume energy production. Figure. 10.b shows the proposed concept extended to several multiple strings with individual string MPPT adjustment capability.

(a)   **(b)**
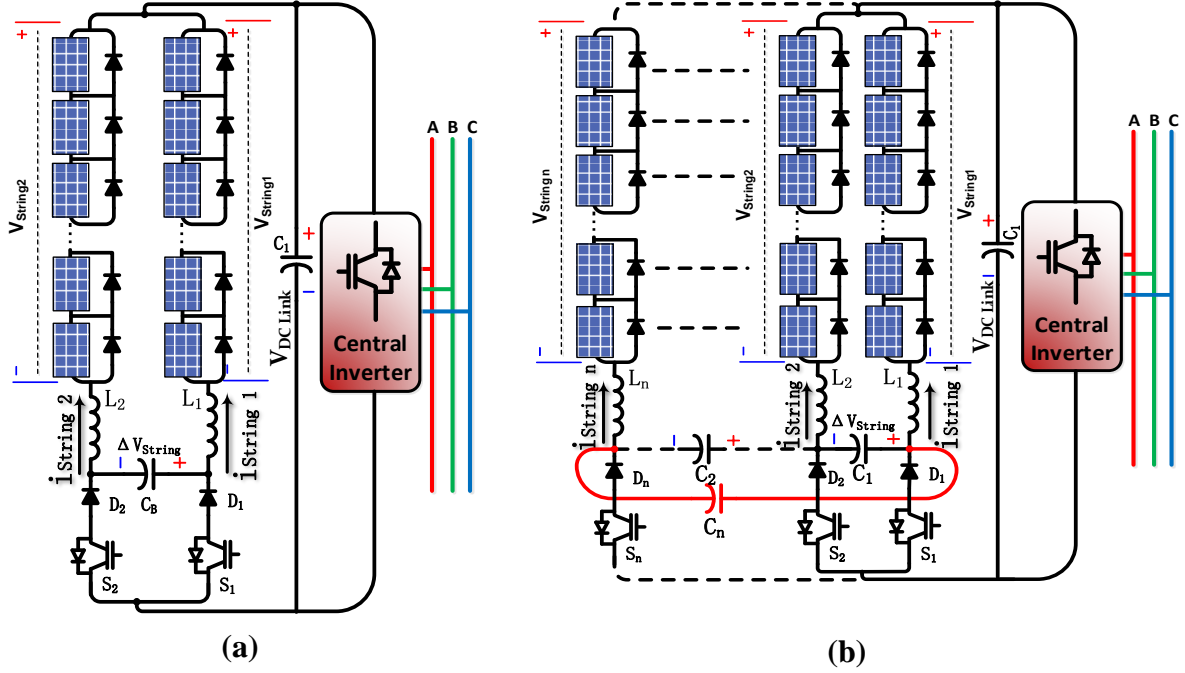
Figure. 10 Proposed fractional power rated converter topology (a) voltage balancing circuit topology for a pair of strings (b) multiple strings approach. Note the IGBTs are rated for the difference in string voltage (i.e. ΔV_String)

The following are the advantages of the proposed modular voltage balancing approach:

- The voltage rating of the required IGBTs is low and is equal to the voltage difference between the adjacent two strings (i.e. ΔV_{String}).

- The proposed approach processes the difference in power between the strings to adjust individual string MPPT with the PWM control.

- Central inverter would see a single peak P-V curve.

19

- A decentralized controller optimizes energy harvesting from each string.

- Cost effective solution that is scalable to multiple parallel strings connected to a central inverter.

(a)

(b)

(c)
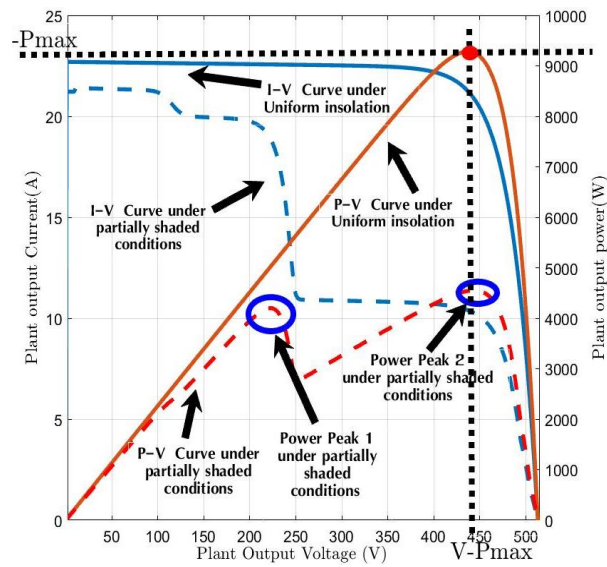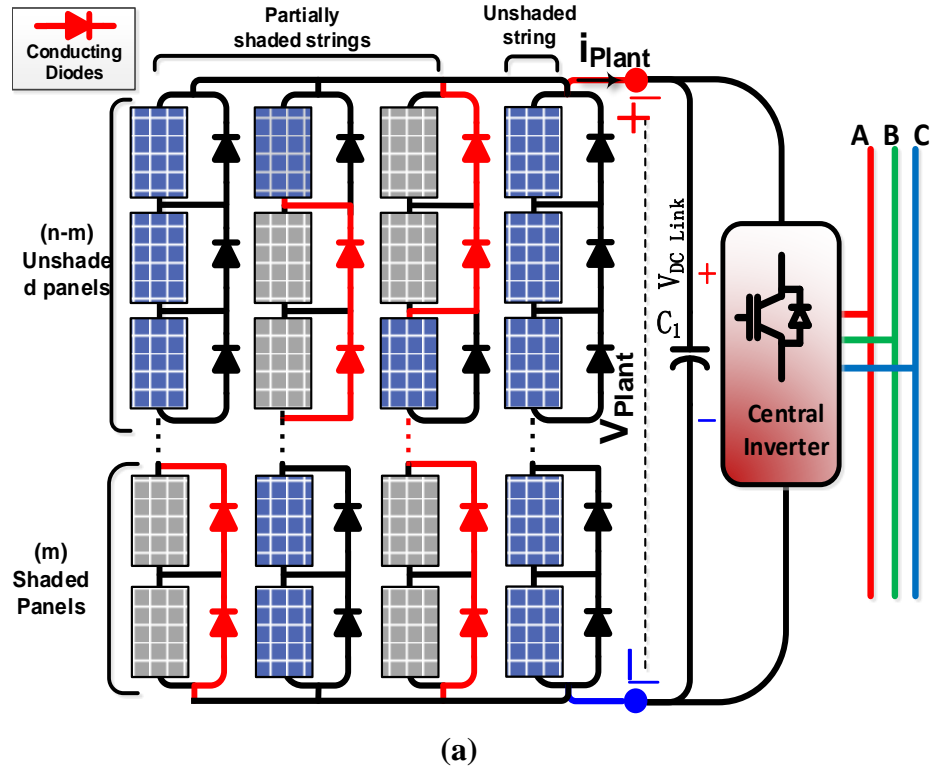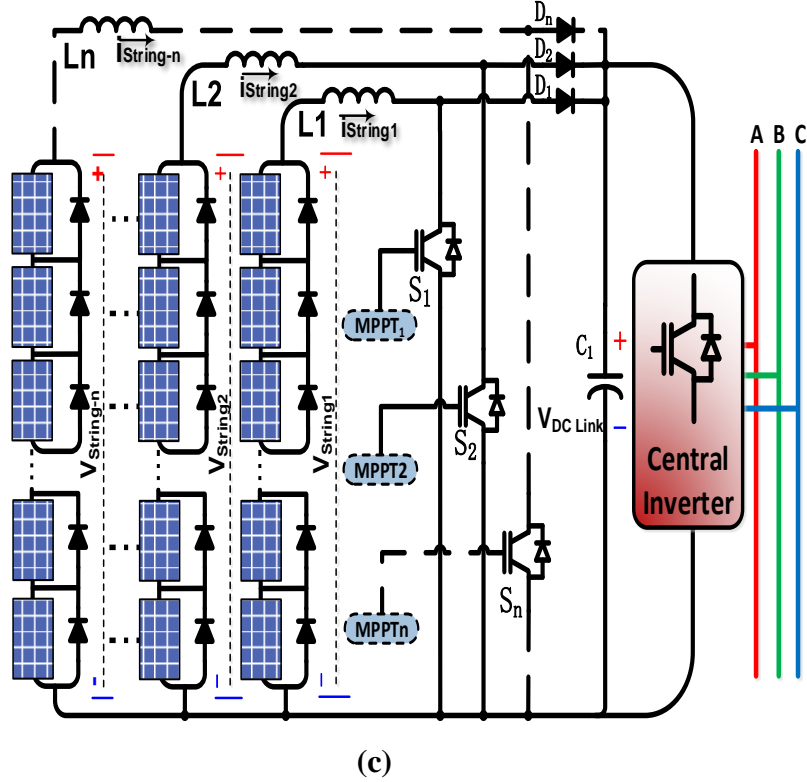
Figure. 11 Conventional series parallel connection arrangement of a typical large-scale PV plant [5] (a) Partially shaded (b) I-V and P-V curve with uniform and partially shading conditions (c) A grid connected multi-stage multistring PV system with boost converter.

2.2 Proposed Voltage Balancing Topology

Figure. 10 shows the proposed modular voltage balancing converter topology. This circuit topology, shown in Figure. 10.a, consists of a reverse blocking switch (ex. IGBT series with a diode (S1, S2)) and a small L-C filter per string. The current flowing in each string is controlled by the duty ratio of the corresponding switch. The voltage difference between strings is built across the filter capacitors (C_b). The modular voltage balancing approach is designed to interact with the PV elements, and the main bus with a configuration enables a low voltage rating for the switches and local control. .b shows an extended architecture of the proposed modular voltage balancing

21

topology extended to several parallel strings. Table 1 shows comparative analysis for active and passive elements used in previously discussed approaches in Figure. 11.a and Figure. 11.C. I_{string} is the maximum string current, ΔV_{string} is the maximum allowed difference in string voltages, ΔI_{ripple} is the maximum allowed ripple in inductors current (i.e. half the string ripple current), and ΔV_{ripple} is the maximum allowed ripple in capacitor voltage.

Table 1 Comparative Ratings of the Presented Partial Shading Mitigation Approaches

		Figure. 10.a (1) balancing circuit for (2) strings	**Figure. 10.b** (N) balancing circuits for (N) strings	**Figure. 11.c** Boost-multistring PV system
Active Switches(S_n)	Number	2	N	N
	Voltage	$\pm \Delta V_{string}$		V_{string}
	Peak current	$2\,I_{string}$	I_{string}	I_{string}
	Average current	I_{string}	$I_{string}/2$	$I_{string}/2$
Inductor(L_n)	Number	2	N	N
	Current	I_{string}	$I_{string}/2$	I_{string}
	Inductance	$\dfrac{\Delta V_{string}}{2.\,\Delta I_{ripple}.\,f_{switching}}$		$\dfrac{V_{string}}{2.\,\Delta I_{ripple}.\,f_{switching}}$
Capacitor(C_b, C_n)	Number	1	N	Nil
	Voltage	ΔV_{string}		Nil
	Capcitance	$\dfrac{I_{string}}{2\Delta V_{ripple} f_{switching}}$		Nil

2.3 Modeling of The Modular Voltage Balancing Topology

The modular voltage balancing converter shown in Figure. 10 operates with high switching frequency with duty cycle control. To ensure current continuity of the inductor currents and

capacitor voltage of the balancing circuit, the two switches are alternatively turned on, i.e. sum of their duty ratios $(\delta_1 + \delta_2) = 1$. Current and voltage differential equations governing the operation of the balancing circuit are (2.1, 2.2):

$$\left[v_{c_b}^{\circ}\right] = \frac{1}{C_b} \begin{bmatrix} -\delta_2 & \delta_1 \end{bmatrix}. \begin{bmatrix} i_{string1} \\ i_{string2} \end{bmatrix}, \tag{2.1}$$

$$\begin{bmatrix} i_{string1}^{\circ} \\ i_{string2}^{\circ} \end{bmatrix} = \frac{1}{L1} \begin{bmatrix} -r & 0 \\ 0 & -r \end{bmatrix}. \begin{bmatrix} i_1 \\ i_2 \end{bmatrix} + \frac{1}{L} \begin{bmatrix} V_{string1} - V_{DClink} \\ V_{string2} - V_{DClink} \end{bmatrix} + \frac{1}{L1} \begin{bmatrix} \delta_2 \\ -\delta_1 \end{bmatrix} \begin{bmatrix} V_{c_b} \end{bmatrix}. \tag{2.2}$$

where (C_b) is filter capacitance, (L_1) is filter inductance, (r) the equivalent series resistance, ($V_{string1}$, $V_{string2}$) are the string voltages, (V_{DClink}) is the output voltage, and ($\delta1$, $\delta2$) are the switches' duty ratios.

From (2.3), each string current is proportional to its corresponding duty ratio the steady state; thus,

$$\frac{i_{string1}}{i_{string\,2}} = \frac{\delta_1}{\delta_2} \quad \text{i.e.} \quad \begin{bmatrix} i_{string1} \\ i_{string2} \end{bmatrix} = \begin{bmatrix} \delta_1 \\ \delta_2 \end{bmatrix}. \begin{bmatrix} i_{string1} + i_{string2} \end{bmatrix} \tag{2.3}$$

2.4 Maximum Power Point Tracking (MPPT) of The Proposed Voltage Balancing Topology

Consider having a number (N) of strings, and it is required to maximize the extracted power from each one of them. Therefore, minimally (N) degrees of freedom are required from the whole system to enable the maximization of (N) output power. The central inverter provides only one degree of freedom through its DC side voltage. The remaining degrees of freedom (i.e. N-1) are left for the balancing circuits, which are the voltage differences between strings (or in other terms, the proportionate ratios of the strings' currents).

To achieve maximum power from all strings, the power-current differential of each string should equal to zero,

$$\frac{\Delta P_1}{\Delta I_1} = 0, \quad \frac{\Delta P_2}{\Delta I} = 0, \quad \frac{\Delta P_3}{\Delta I} = 0, \quad \ldots \quad \frac{\Delta P_N}{\Delta I_N} = 0 \qquad (2.4)$$

The MPPT controller of the central inverter depends on the total power and current (or voltage) received by the inverter from all strings to achieve MPP (5), but this does not guarantee that all strings are operating at their individual MPP.

$$\frac{\Delta(P_1 + P_2 + P_3 \ldots P_N)}{\Delta(I_1 + I_2 + I_3 \ldots I_N)} = 0 \qquad (2.5)$$

The MPPT of the central inverter can be implemented using any of the state of the art MPPT techniques. However, since the voltage balancing topology is new to the literature, none of these techniques directly apply to the topology. In this section, maximum power point tracking based on the voltage balancing topology MPPT_bal is presented.

2.4.1 Traditional MPPT Approach

A traditional extension of the Perturb and Observe P&O MPPT Method in this topology would require a centralized controller that monitors all voltages and currents of strings, changes the duty ratio of one balancing circuit at a time, and loops over all balancing circuits until the maximum power from each string is reached. This will inhibit very slow performance and complicated searching methods due to the multidimensional nature of the search problem.

In this section, a new MPPT method is proposed that suits the suggested balancing topology and its multidimensional nature, but in a decentralized control form. The role of the balancing circuits, having (N-1) degrees of freedom, is to achieve MPP for individual strings with the cooperation of the central inverter MPPT (i.e. the control of each balancing circuit should not conflict with the MPPT of the central inverter or any other balancing circuit controller).

24

Since each balancing circuit is mainly affecting the operating points of its two attached strings, it is desirable to define a cost function for each balancing circuit that relates to the two attached strings without causing a counter effect on the neighboring balancing circuits. A proposed way of achieving this is by finding the power-current (or power-voltage) differentials of the two attached strings and adjusting the duty ratios (δ₁, δ₂) so that both power-current slopes (or power-voltage slopes) are equal. This will ensure that the increase in one of them translates to the increase in all of them. In other words, they act as one string, as seen by the central inverter, so that easier search for MPP of the whole PV plant can be achieved.

To maximize the power of a given string (k), the change in current should be proportional to its power-current derivative (i.e. $\Delta I_k \propto \frac{\Delta P_k}{\Delta I_k}$). As such, in order to achieve the proposed cost optimization function, (i.e. equal power-current slopes of two strings (k, m) attached to the same balancing circuit) the change in the difference between two string currents should be proportional to the difference in their corresponding power-current derivatives, i.e.

$$\Delta(I_k - I_m) \propto \left(\frac{\Delta P_k}{\Delta I_k} - \frac{\Delta P_m}{\Delta I_m} \right) \propto \Delta(\delta_k - \delta_m) \tag{2.6}$$

Since a string current is proportional to the duty ratio of the corresponding switch, then the change in the duty ratio difference can be set as

$$\Delta(\delta_k - \delta_m) = G \left(\frac{\Delta P_k}{\Delta I_k} - \frac{\Delta P_m}{\Delta I_m} \right), \tag{2.7}$$

where (G_i) is the controller proportional gain.

Solving (2.7) with ($\delta_k + \delta_m = 1$) results in

$$\begin{bmatrix} \delta_k \\ \delta_m \end{bmatrix} = \frac{1}{2} + \frac{G_i}{2} \int \begin{bmatrix} \left(\frac{\Delta P_k}{\Delta I_k} - \frac{\Delta P_m}{\Delta I_m} \right) \\ -\left(\frac{\Delta P_k}{\Delta I_k} - \frac{\Delta P_m}{\Delta I_m} \right) \end{bmatrix} \tag{2.8}$$

By applying similar cost functions for the rest of the balancing circuits, i.e. the difference in power-current differentials of all pairs of strings will equal to zero, this yields equal power-current differentials of all strings:

$$\left(\frac{\Delta P_1}{\Delta I_1} - \frac{\Delta P_2}{\Delta I_2} \right) = 0, \left(\frac{\Delta P_2}{\Delta I_2} - \frac{\Delta P_3}{\Delta I_3} \right) = 0, \left(\frac{\Delta P_3}{\Delta I_3} - \frac{\Delta P_4}{\Delta I_4} \right) = 0, \dots \left(\frac{\Delta P_{N-1}}{\Delta I_{N-1}} - \frac{\Delta P_N}{\Delta I_N} \right) = 0. \tag{2.9}$$

Therefore,

$$\frac{\Delta P_1}{\Delta I_1} = \frac{\Delta P_2}{\Delta I_2} = \frac{\Delta P_3}{\Delta I_3} = \frac{\Delta P_4}{\Delta I_4} = \dots \frac{\Delta P_N}{\Delta I_N} = \frac{\Delta(P_1 + P_2 + P_3 \dots P_N)}{\Delta(I_1 + I_2 + I_3 \dots I_N)} \tag{2.10}$$

The maximization of the overall power received by the central inverter is reflected to the maximization of power of all strings. It should be noted that the capability of the proposed MPPT algorithm of the balancing circuit is a function of the operating point set by the MPPT of the central inverter. Therefore, using MPPT_bal to control the balancing circuit may decrease the overall power from the strings if no MPPT of the central inverter is applied.

2.5 Control Strategy
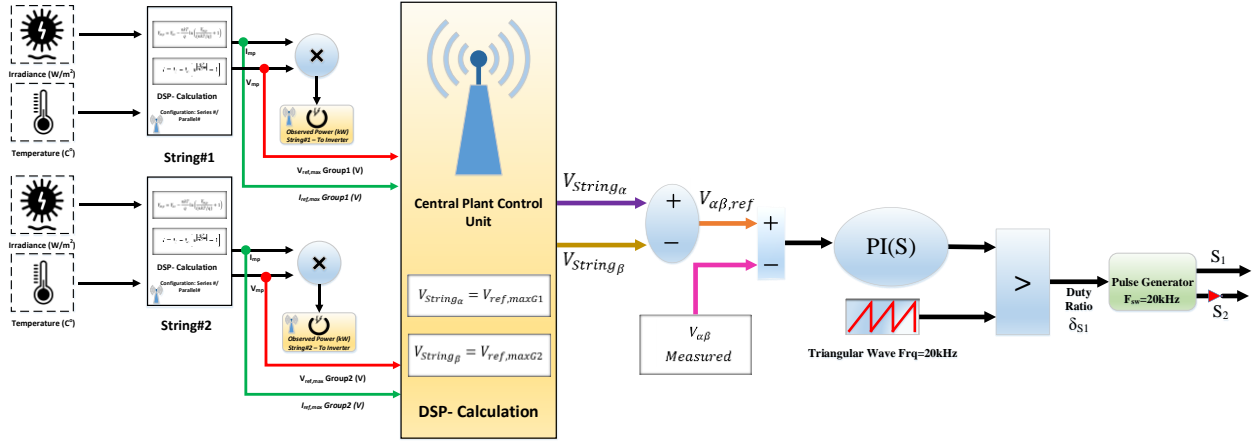
Figure. 12 Control strategy the fractionally rated voltage-balancing converter shown in Figure. 10

Base on the given environmental data, a reference current and voltage is generated to drive the current balancing approach to achieve extracting the maximum power available at all times.

2.6 Simulation and Design Example

A two group 500 KW PV power plant using SunPower SPR-305-WHT [46] design example with 1500 V DC bus is considered to demonstrate the operation of the proposed modular voltage balancing topology in Fig 1.a. The parameters in the Table 2 were used for simulation. Simulations of the proposed topology were performed using Matlab SIMULINK and PLECS. To have a robust design, the capacitor is designed at full insolation when the current is full since $C_b \propto I_{string}$. As well as the inductor is designed at worst operation condition when the voltage difference between the two string is maximum ΔV_{string} since $L_1, L_2 \propto \Delta V_{string}$. The simulation is testing the voltage balancing circuit under the following environmental conditions: $String_1 = 250$ W/m^2 and $String_2 = 1000$W/m^2 at 25C^o.Thus for this condition the $String_1$ should operate at V_{MPP} of 1443.29V and $String_2$ should operates at 1500 V to harvest maximum power. In order to achieve

27

the targeted maximum power, per the modular voltage balancing approach a voltage difference between the strings should be ΔV_{string}=53.71 V.

The proposed fractional power modular voltage balancing approach presented in Fig.1.a harvest energy higher than the conventional approach in Figure. 11.a and effectively mitigate the partial shading effects [25]. Moreover, it is evident that the central inverter would see only a single P-V curve which facilitates the search for the maximum power point. Figure. 7 and Figure .5 show that the maximum harvested power is evidently found at ΔV_{string}=53.71 V. Furthermore, Figure. 6 shows the maximum available current is extracted for the given environmental condition from each string. Another benefit from using the proposed topology is the switches in Fig 1.a are rated based on the maximum voltage difference would be reached between strings as shown in Fig.4. The proposed modular voltage balancing topology using the new MPPT algorithm is able to harvest 2000W extra as shown in Figure. 7. In fact this approach offered higher energy harvesting than Danfoss approach (Fig 2.c)[30] and this amount would be more significant for larger PV plant with multiple parallel strings.

Table 2 Specification & Operation Conditions used for the proposed topology in Figure. 10.a

Parameter	Component Rating
C_b	0.5mF
L_1,L_2	0.5mH
Switching frequency	20KHz
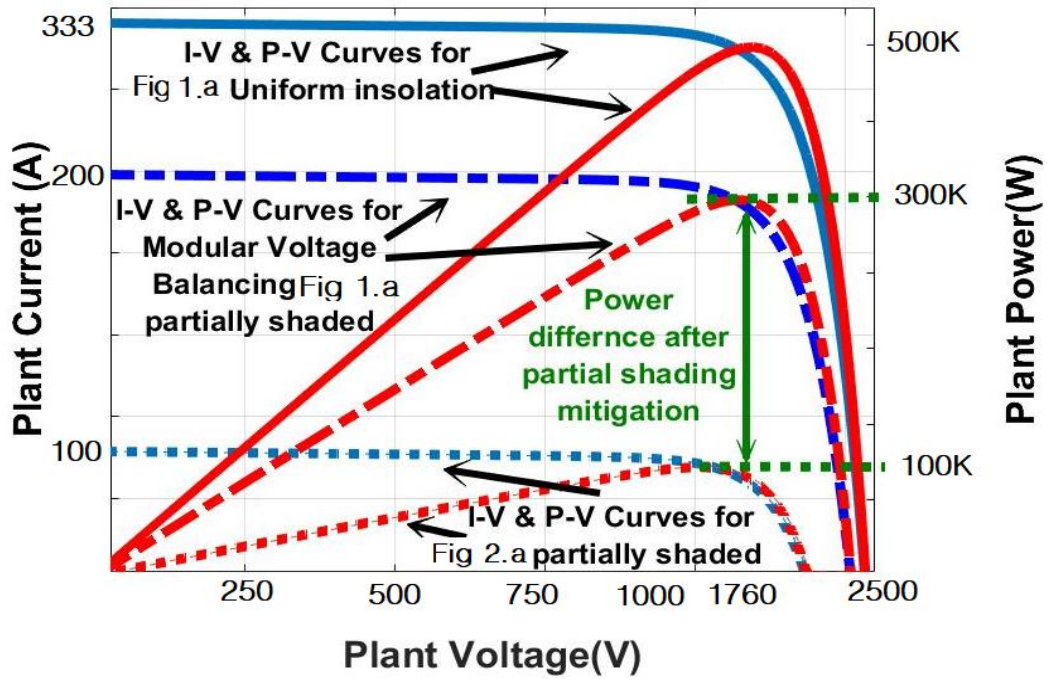
Figure. 13 I-V, P-V curves for 0.5 MW PV Power Plant with conventional design approach (Figure. 11.a) vs modular proposed voltage balancing (Figure. 10.a)
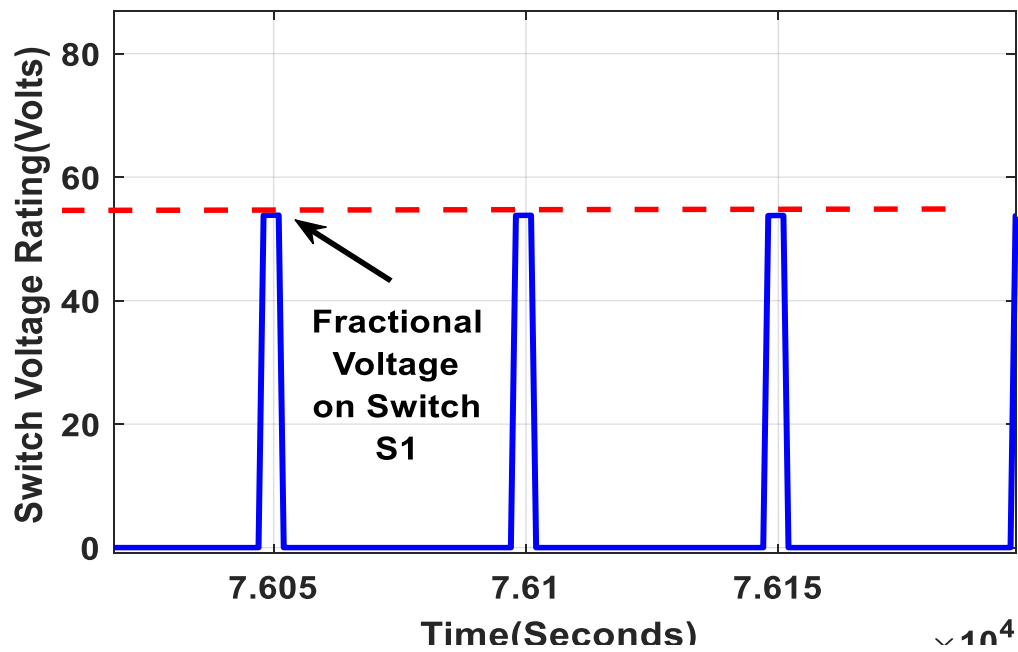
Figure. 14 Fractional voltage switch rating for proposed approach in Figure. 10.a for S1
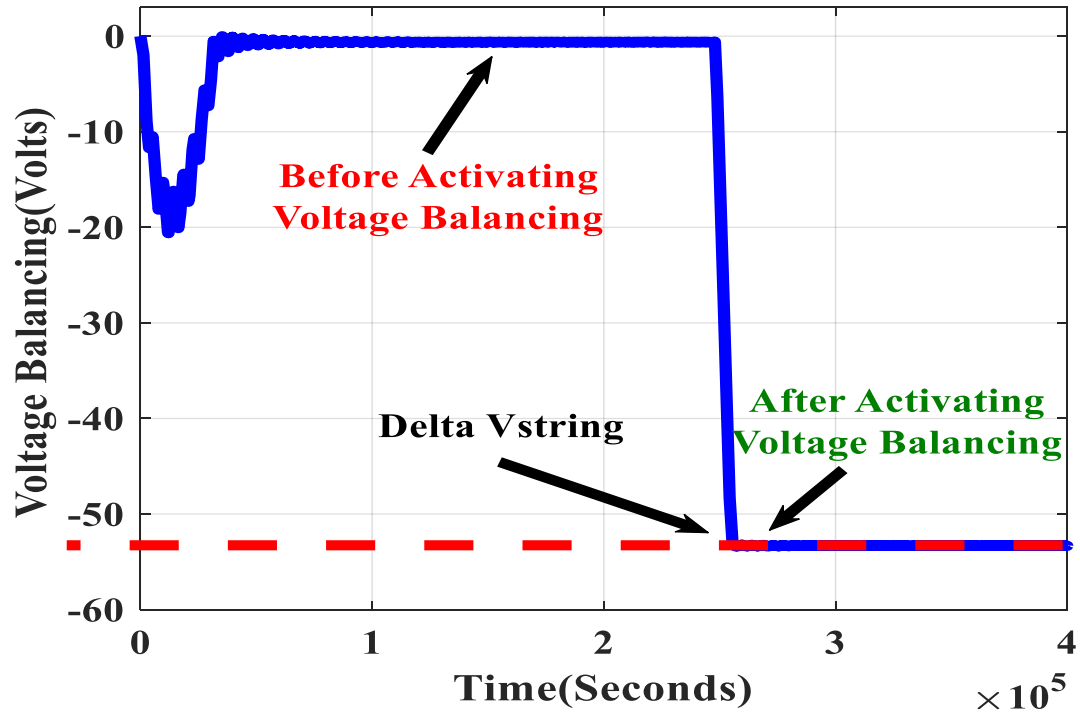
Figure. 15 ΔV_{string} **measured on the balancing capacitor** (C_b)
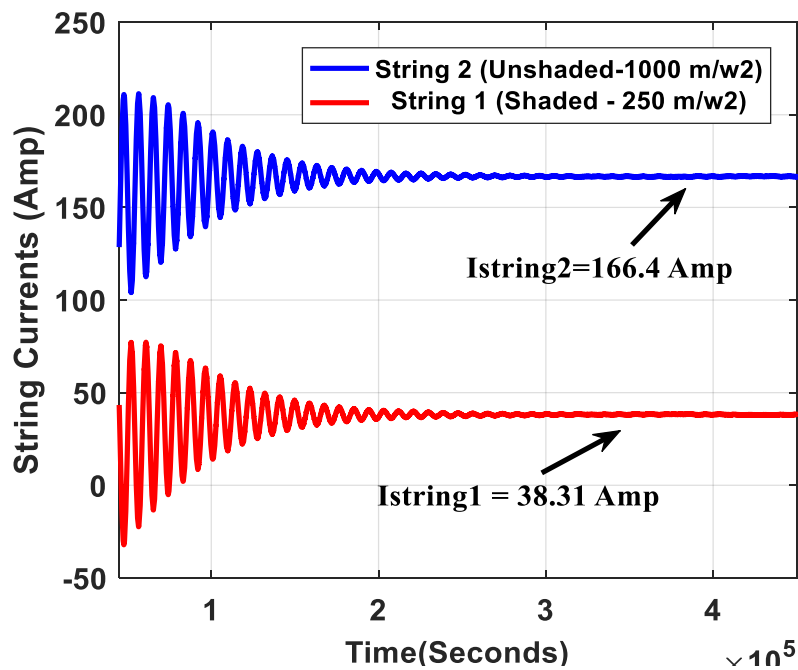
Figure. 16 Maximum currents extracted from String₁ and String₂ by the modular the

voltage balancing.
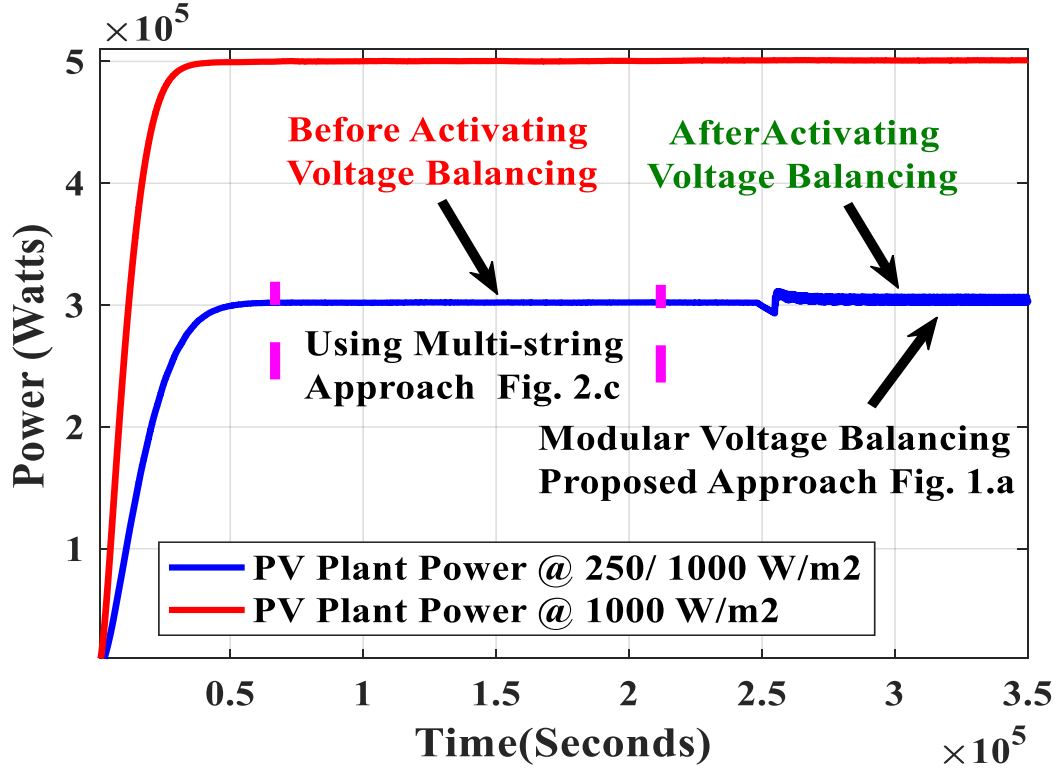
Figure. 17 The maximum total power harvested by the proposed modular voltage balancing topology (Figure. 10.a) vs. by the multi-stage multi-string multistage boost distributed PV system with string optimization (Figure.11.c).

2.7 Qatar Case

This section studies concept of fractional rated power converter for voltage balancing based on the practical data acquired from a small test bench setup in Qatar by the Qatar Energy and Environment Research Institute. The setup uses one kind of PV module where one is cleaned frequently and the other is left not cleaned. The data points are processed in the proposed balancing converter to test its operation for Qatar. Qatar geographical location gives it unfair advantage from utilizing the solar energy since it's sunny all year round. However, the average temperature is high during the year and that effect on the performance of the system.

The given data is for everyday of the year; however, for simplicity only the 1st, 15th and 28th of the month has been processed in the proposed approach. The data covers the ambient temperature of PV, irradiance, maximum power voltage, and maximum power current. The data points are processed through the SIMULINK module to check if the proposed approach would still work for the different environmental conditions for Qatar and produced the same power as the actual PV system installed on site in Qatar.

The PV panel used in the plant is multi-crystalline silicon, installed with a 22 degrees tilt toward the south. The module used is manufactured from Sharp with power rating of 220 Watts as presented in Figure. 18.

```
NOMINAL RATINGS:
MAXIMUM POWER (+10%/-5%) (Pmax)           220.0W
OPEN-CIRCUIT VOLTAGE      (Voc )           36.5V
SHORT-CIRCUIT CURRENT     (Isc )           8.20A
VOLTAGE AT POINT OF MAXIMUM POWER (Vmpp) 29.2V
CURRENT AT POINT OF MAXIMUM POWER (Impp) 7.54A
MAXIMUM SYSTEM VOLTAGE                     1000V
OVER-CURRENT PROTECTION                      15A
(IRRADIANCE OF 1000W/m², AM1.5 SPECTRUM
                  AND CELL TEMPERATURE OF 25°C)
```

Figure. 18 Sharp Solar Module ND 220E1F specifications
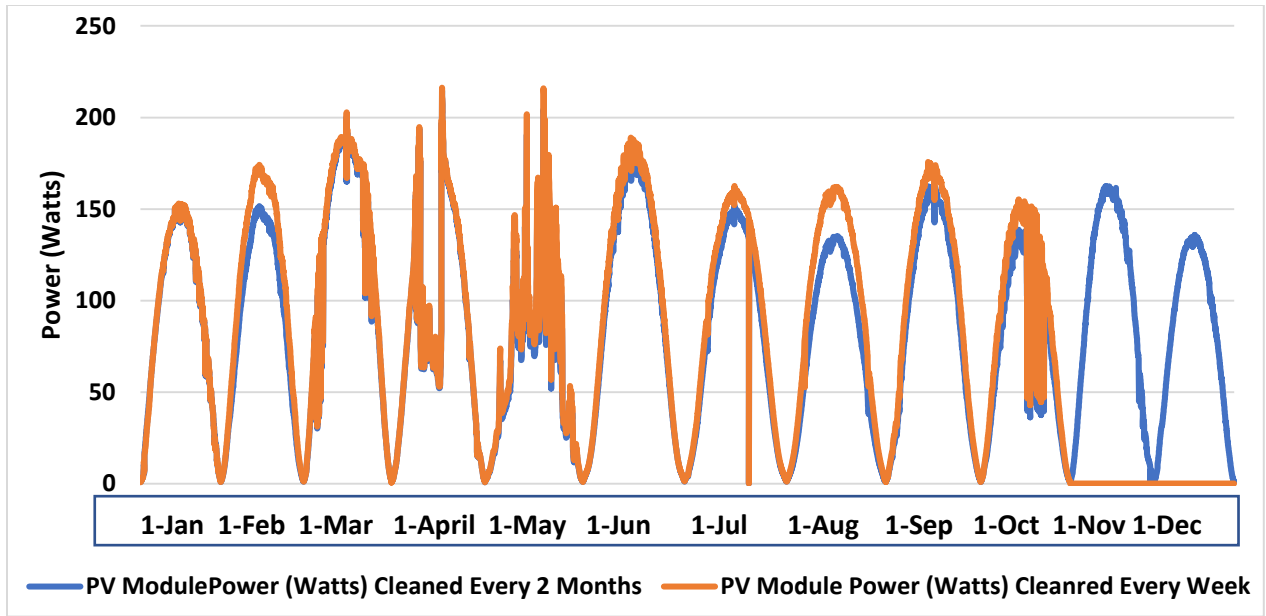
Figure. 19 Power Harvested on the first day of each month for 12 months from January to December 2017.
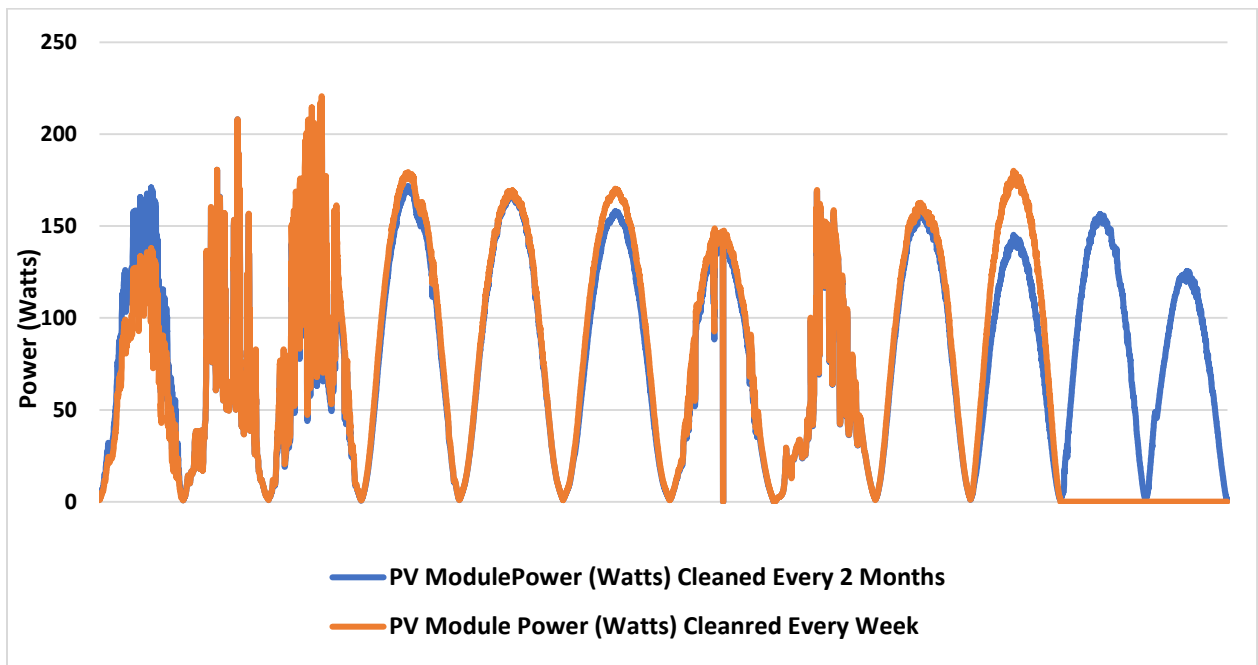
Figure. 20 Power Harvested on the 15th day of each month for 12 months from January to December 2017.
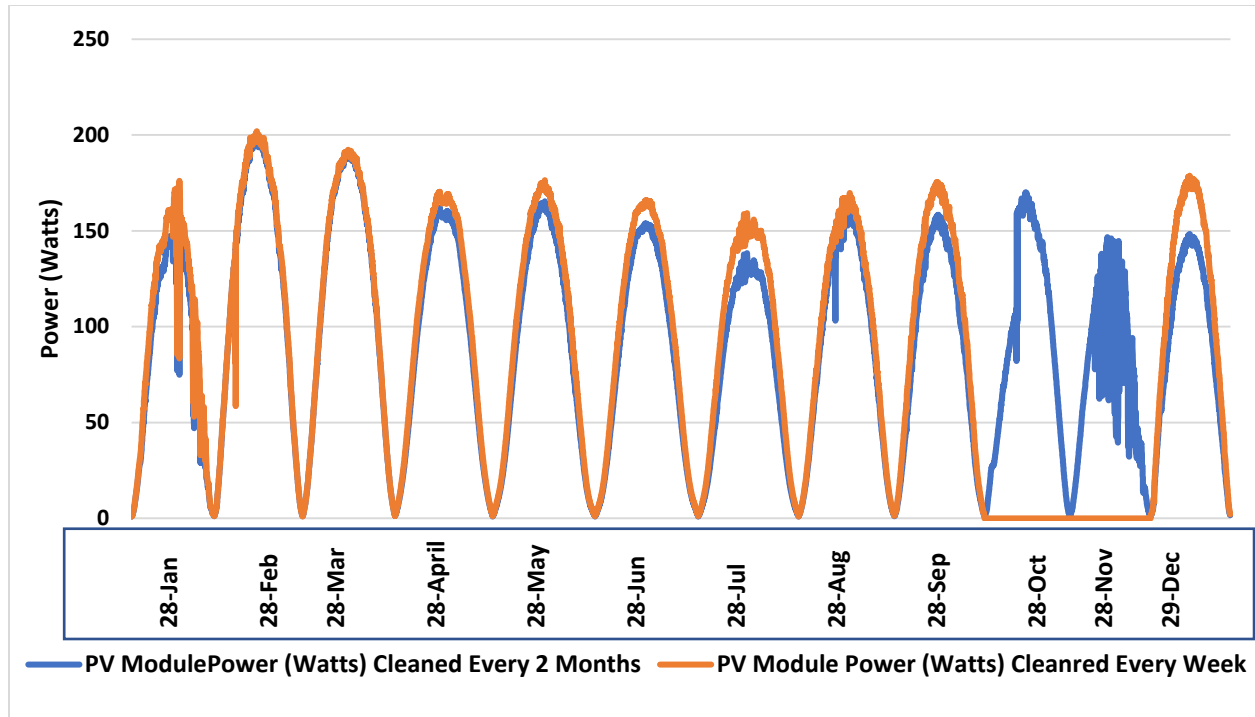
Figure. 21 Power Harvested on the 28th day of each month for 12 months from January to December 2017.

Figure. 19 Figure. 20, and Figure. 21 show the real operation of installed PV panel in QEERI testing facility. Each of these operation curves showed that the PV panels operate better when it has higher frequency in cleaning. In addition, for the selected dates, it showed that the PV panels never reached its maximum power point of operation per the manufacturer design as shown in Figure. 18.

Based on the given data from Qatar Energy Environment Research Institute without using the voltage balancing approach, the following results are presented for a single day operation in Figure. 21. However, if the voltage balancing approach is included then the power is harvested through a single Central Inverter and reliability is higher. Per the given environmental conditions, the data has been processed for the exact same PV module using SIMULINK/MATLAB and the results are presented below in

34
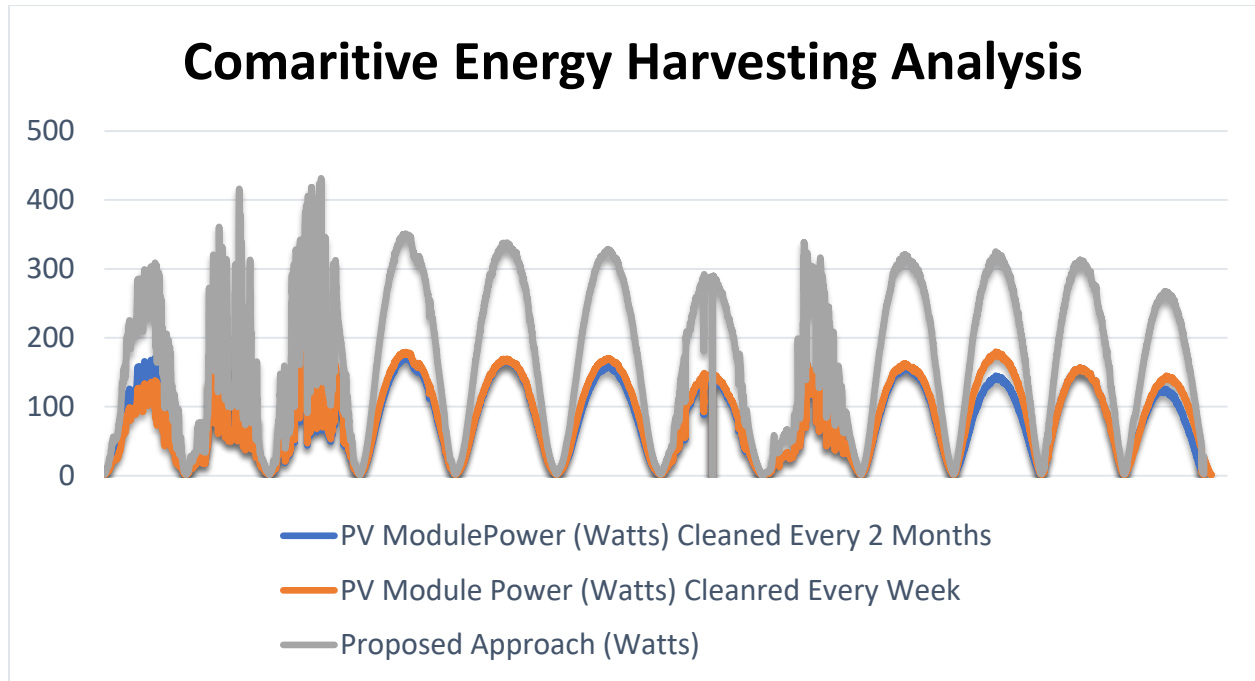
Figure. 22 Comparative Energy Harvesting approaches for the proposed system using the fractional voltage balancing approach.

The results in Figure. 22 show that the total power is harvesting through the voltage balancing matching the given environmental conditions to extract the maximum power point.

2.8 Experimental Verification

2.8.1 Verification-I

The proposed voltage balancing topology and its corresponding MPPT algorithm are verified experimentally. The PV modules are connected to form an array of three strings; each string consists of two series modules. Each PV module received from the manufacturer has two bypass diodes across its two series halves. The positive terminals of the three strings are solid connected to each other to form the positive DC rail, while the three negative terminals are connected to a set of three balancing circuits to form the negative DC rail. The DC link is feeding a buck converter, which is feeding a resistive load. The buck converter here is imitating the 'stand-alone' MPPT control operation of a central inverter, but without focusing on the grid interfacing issues.

To study the effect of partial shading on extracted power and verify the advantage of the proposed voltage balancing circuit, half of a PV panel in string #2 is shaded, i.e. it will be bypassed by its parallel diodes, and as such, this string will have lower voltage ($V_{open\ circuit} \approx 30V$) than the other two strings ($V_{open\ circuit} \approx 40V$).

Figure. 23.a show the traditional parallel operation of strings by turning on all the switches of the balancing circuits at the same time. The diode series with the IGBTs replaces the reverse blocking protection. Since string 2 is partially shaded, it has lower voltage than strings 1 and 3, which are not shaded. Thus, it does not contribute to any power (and its voltage does not drop) because its open circuit voltage is less than the maximum power point (MPP) voltage of the strings 1 and 3.

Figure. 23.b shows the effect of enabling the MPPT algorithm of the proposed voltage balancing topology on power extraction from the shaded and unshaded strings. Herein, although the open circuit voltage of string 2 (shaded) is lower than the MPP voltage of strings 1 and 3 (unshaded), the balancing circuits enable each string to operate at a different voltage that ensures its own MPP.
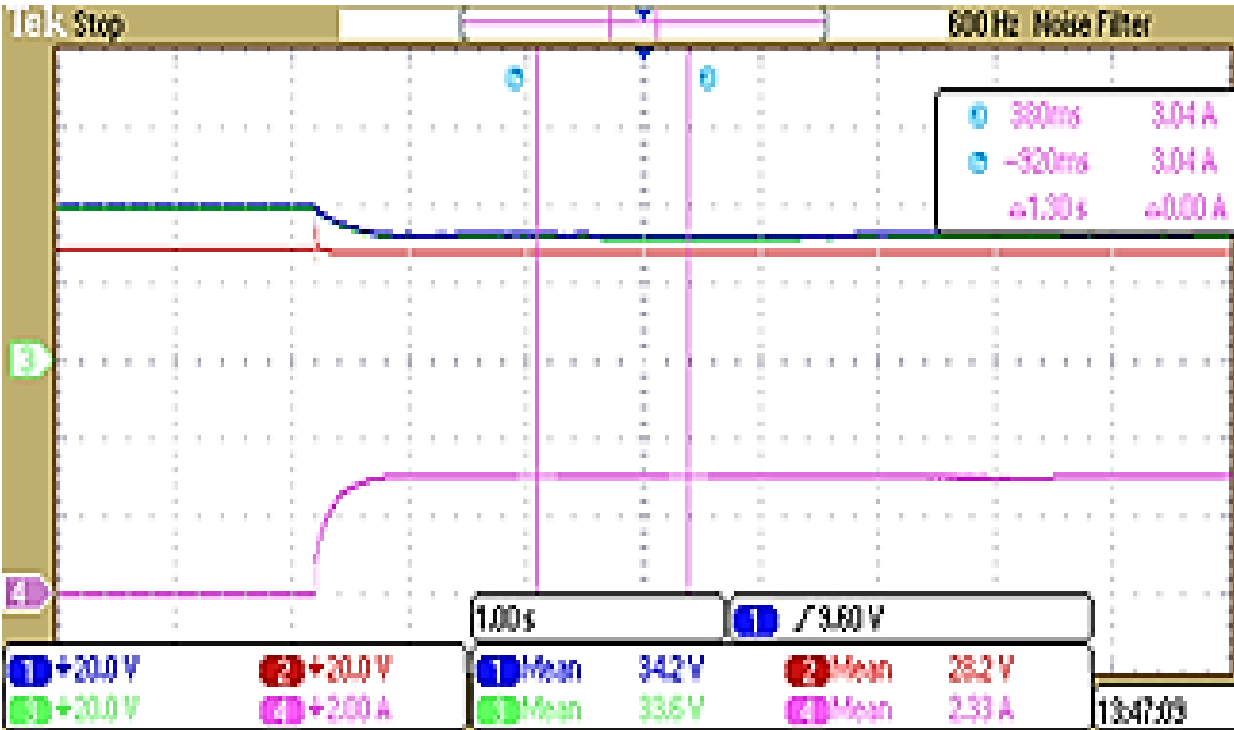
(a) Maximizing without balance the global MPPT is trapped at the MPP of strings 1 and 3, while string 2 (shaded) has lower $V_{Open\ Circuit}$ than the V_{MPP} of the other two strings; hence, string 2 is not sharing power.
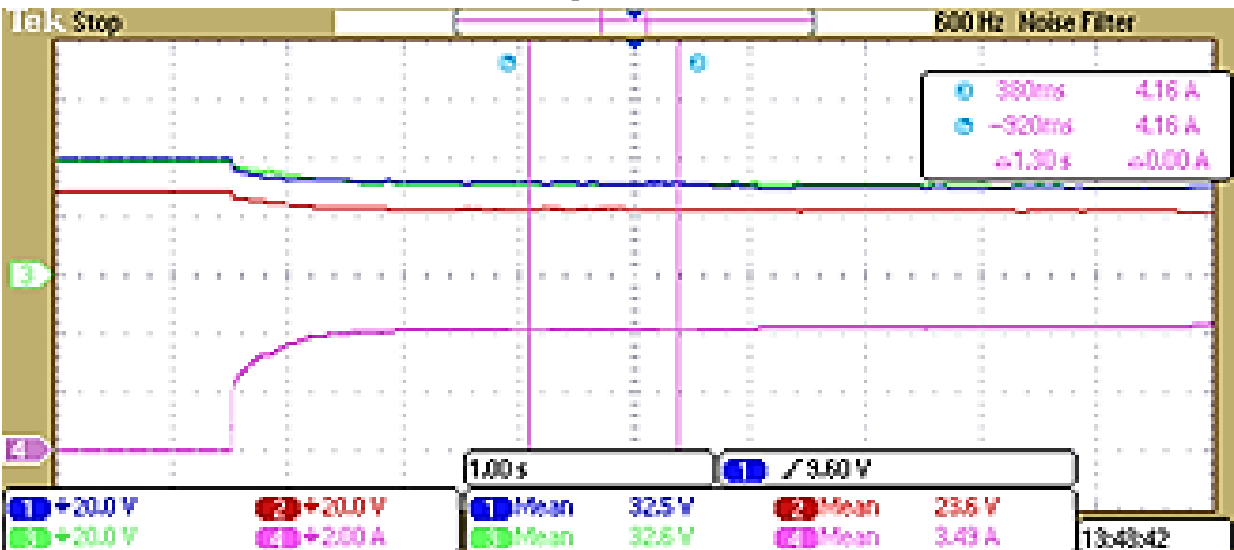
(b) Maximizing with balance the global MPPT is not trapped at the MPP of strings 1 &3, and each string operates at its preferred voltage; hence, string 2 is sharing power.

Figure. 23 Experimental results under partial shading conditions Channels 1, 2, & 3 represent the voltages of the three strings (20V/div). Channels 4 represents the resistive load current (1A/div) Time scale (2 second/division)

2.8.2 Verification-II

A small-scale laboratory porotype for Figure. 10 was developed and tested for functionality as shown in Figure. 24. The design prototype is set for 120 Voltage input and maximum power output is 400 Watts. The design can handle higher power ratings; however, the limitation is due the available power supplies in the lab. The prototype is built using SiC switches from Wolf Speed (C2M0080120D) and diodes from Little Fuse (APT60D120BG) as shown in Appendix-I. The gate driver used was from CREE (A3817210) to drive the two balancing switches S1, and S2. The balancing capacitor ($C_{\alpha\beta}$) was sized with 25uF. Both inductors L1 and L2 are designed for 0.5mH. Table 3 presented the design parameter for the designed fractionally rated voltage-balancing stage.

Table 3 Specification and values for design example for Voltage balancing stage using SiC switches

Design Parameters	
Power Rating	400 Watt
Switching (Fsw)	20kHz
Inductor current ripple	5%
Inductors (L1,L2)	0.5mH
Voltage Input	120 V
Capacitor C1	25uF
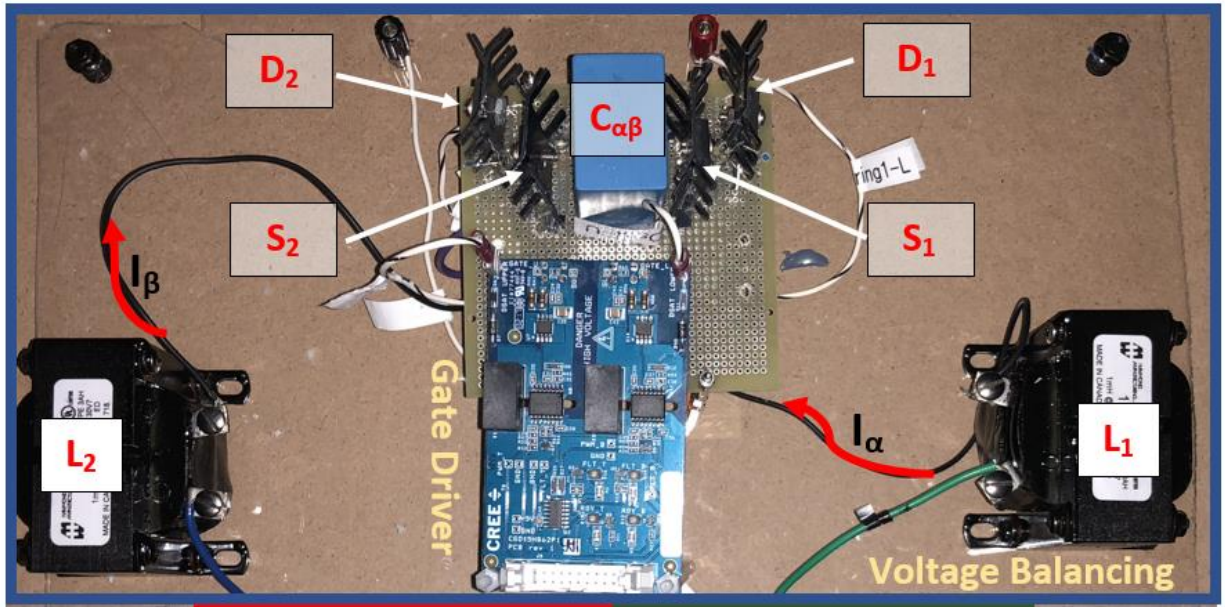
Figure. 24 Fractional rated voltage balancing DC-DC converter design for Large Scale PV plant using SiC switches.

When the Stringα and Stringβ available power matched the current Iα and Iβ should be equal as shown in Figure. 25. The current presented is DC with value of 1.35 A and 1.33 A on each of these strings and the duty ratio was set to 0.5 to hold equal amounts of current. As well as, it can be noticed that the output V_plant seen is 118V, which is equal to the string voltage. The total current of the plant was 2.71 A which is equal to the summation of the currents from Stringα and stringβ.
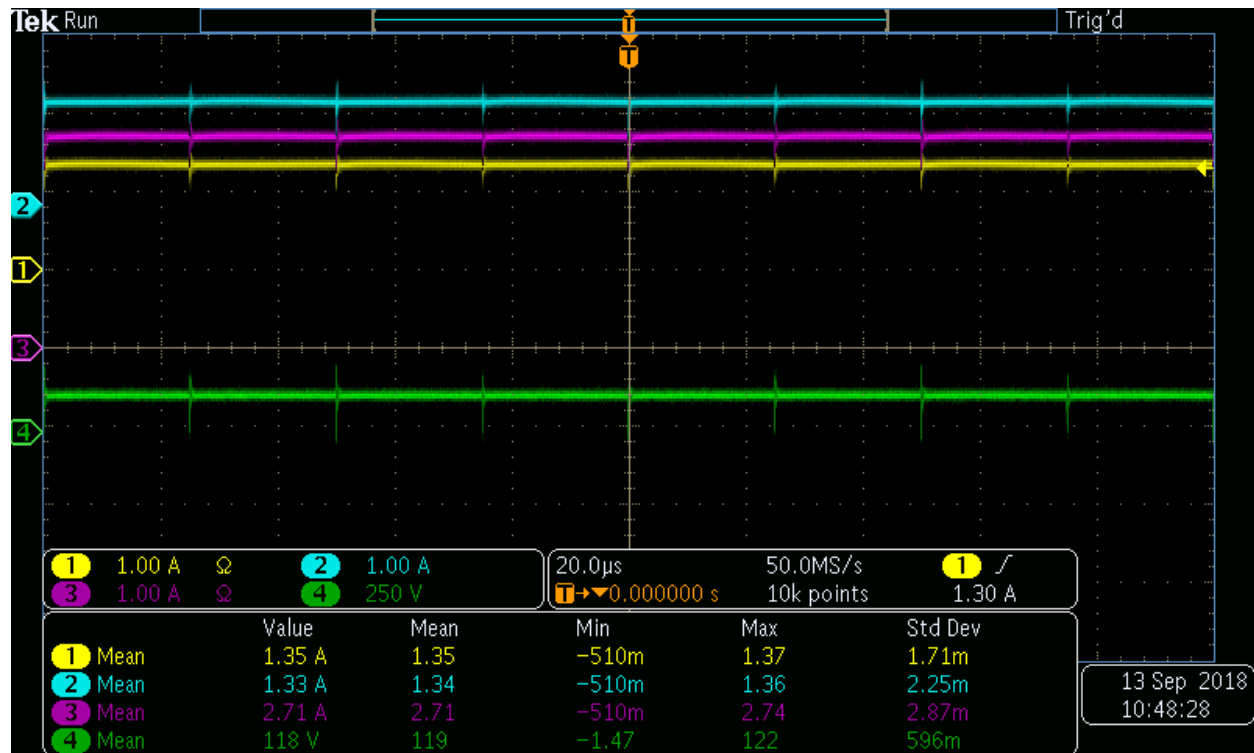
Figure. 25 Voltage balancing stage with equal current on each of the strings.

However, if the available power on Stringα and Stringβ is different, then the voltage balancing stage should allow each of these stages to act independently of other source and feed into the plant power. The presented results in Figure. 26 confirms that each string acted independently of the other with currents of 1.4 A and 1.29 A from each of these strings at duty ratio of 0.48. The total plant voltage was not affected with voltage of 120V. As well as it can be noticed the total current is equal to the summation of the currents from Stringα and Stringβ to add up to 2.7 A as show in Figure. 26. It can be noticed from Figure. 25 and Figure. 26 that the current value was reached by changing the duty ratio on S1 & S2.
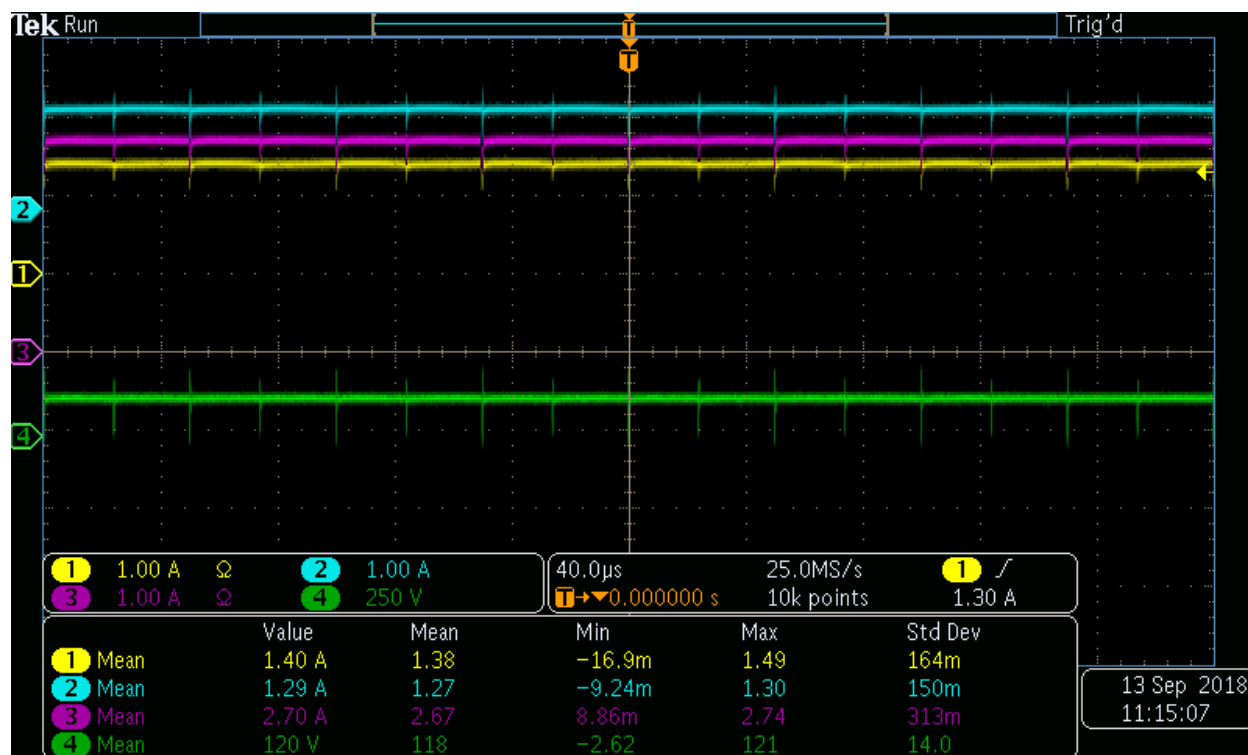
Figure. 26The Voltage balancing stage with non-equal currents on each of the strings.

For the voltage balancing stage to work, the capcitor **C$_{\alpha\beta}$** plays a vital rule because it handles the voltage different generated between the two strings. As it can be seen in Figure. 27, when there is voltage different between the two strings was built across the capacitor when the mean voltage on Stringα was 115 V and the mean voltage on String β was 108 V, a mean voltage difference of 10.4 V was built across the capacitor **C$_{\alpha\beta}$** as shown in Figure. 27.
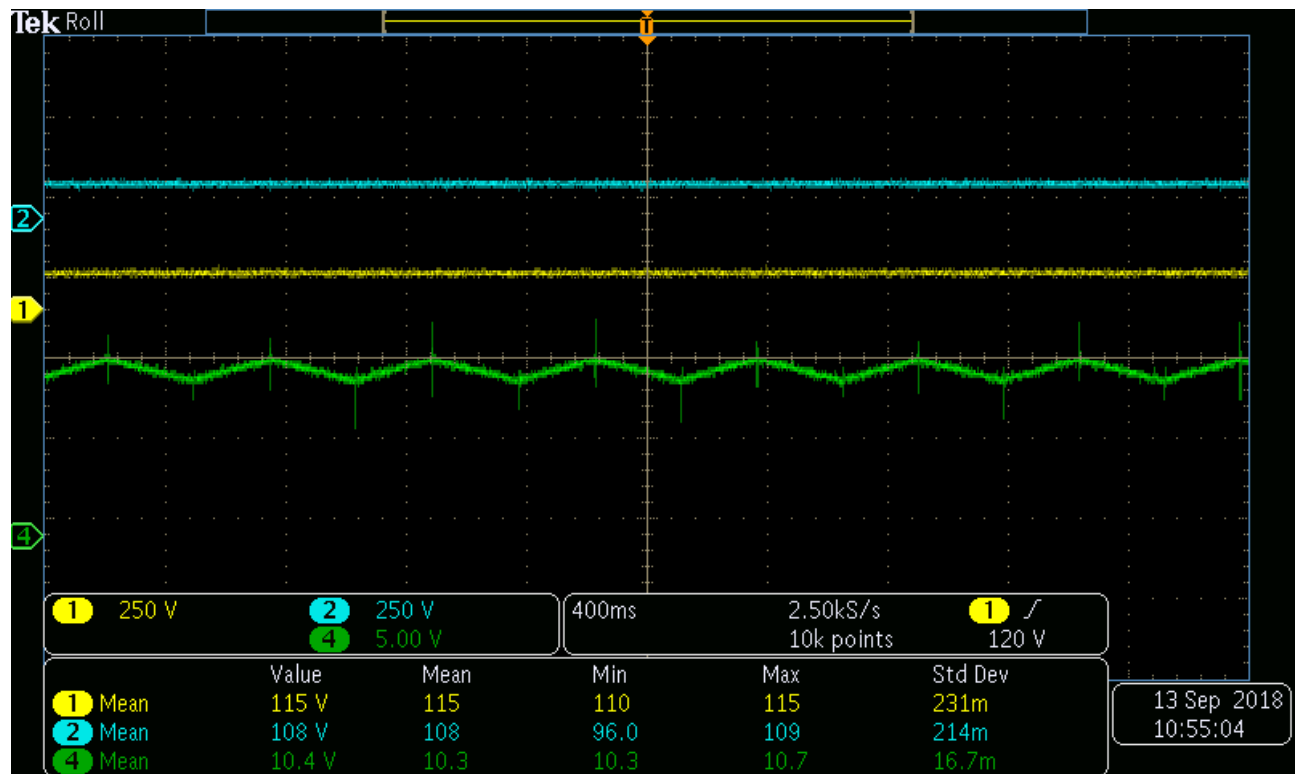
Figure. 27 Voltage Balancing Topology for two strings with voltage on String α= 115 V and String β= 108 and the Voltage on C$_b$.

However, when the voltage on Stringα equals to the voltage on Stringβ, the capacitor (**C$_{αβ}$**) voltage should equal to zero. Running the experiment with equal strings voltages such that Stringα mean voltage is 119V and Stringβ mean voltage is 118V, the capacitor (**C$_{αβ}$**) sees a mean voltage of 303.mV, which is approximately equal to zero.
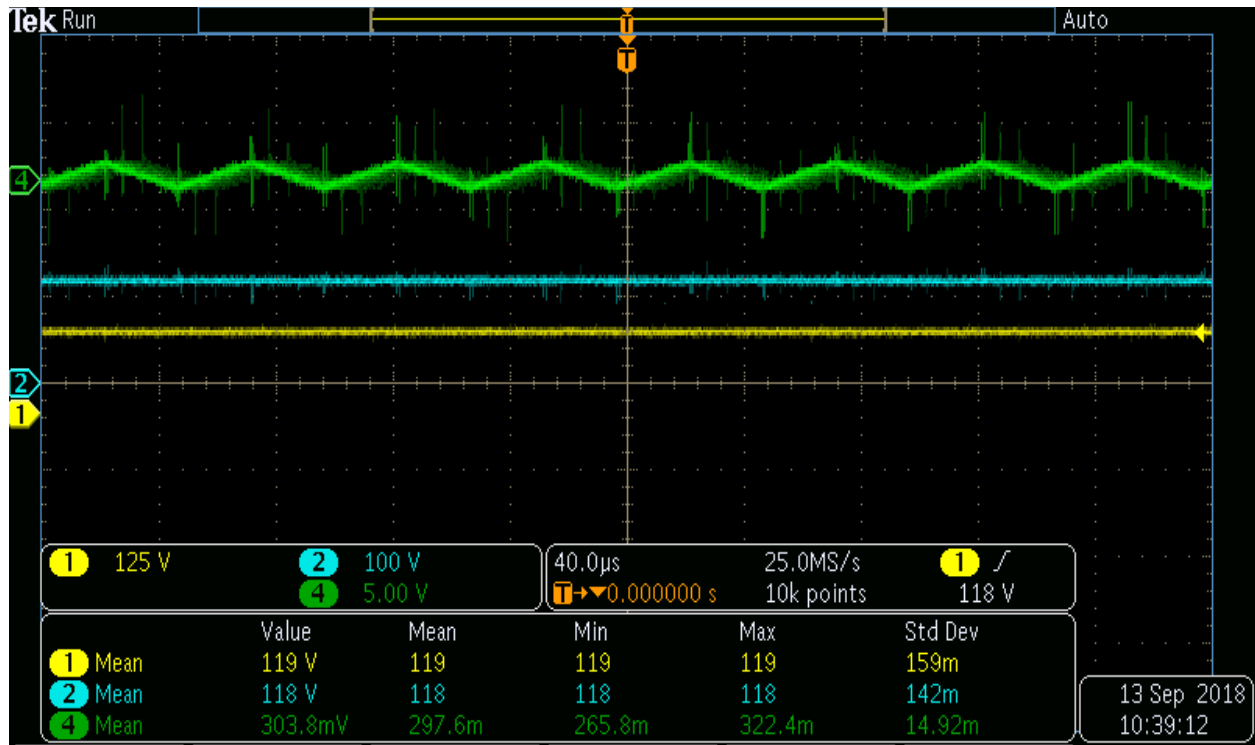
Figure. 28 Voltage Balancing Topology for two strings with balanced voltages on String α= 119 V and String β= 118 and the Voltage on C_b is equal to 303.8mV.

2.9 Conclusion

A new fractional power modular voltage balancing topology has been proposed for large scale PV power plants. The proposed approach has been shown to be modular and can extend to many parallel strings. It has been shown that the approach enables each string to operate at its own optimal voltage that corresponds to the string's Maximum Power Point. Also, a new industry friendly MPPT decentralized control approach has been shown to harvest maximum available power.

III.   APPLICATION-II: NEW TWO STAGE DIFFERENTIAL MODE POWER CONVERTER FOR LARGE SCALE PV PLANTS*

3.1 Introduction

In the recent past, PV power plant sizes have been growing and reaching hundreds of Mega-Watts [32]. Very Large-Scale PV (VLS-PV) plants assessed for their high efficiency when their architecture is upgradable and reliable [33]. In addition, power conversion cost is low and VLS-PV plant is able to mitigate the effects of partial shading. VLS-PV plants with distributed power electronics converters have demonstrated higher energy yields, better reliability, substantial reduction in design costs, and more flexibility in PV power plant designs [19,34,35,45].

Recent advancements in the power electronics has enabled designing central inverters with higher power density. ABB most recent high-power central inverter (PVS800) able to achieve maximum power output of 2MW from a maximum of 24 separate DC inputs from multiple PV strings [35,36]. Furthermore, with the advent of higher string voltage of 1500V, more number of PV modules can be connected in series, thereby reducing the number of combiner boxes, lowering the current and improving the overall efficiency [37].

Currently there are several types of energy harvesting architectures for large-scale PV power plants (Fig. 1) [42]. In Figure. 29.a , several PV modules are connected in series parallel groups are connected to a DC/DC converter and a central inverter.

―――――――――――――――

As shown, this approach employs a fully rated DC-DC converter followed by a DC-AC inverter to harvest different sections of a large solar field [42]. A main drawback of this approach is that it requires fully rated DC-DC converters and DC-AC inverters for each section of a solar filed.

Consequently, the capital cost of installation is high. In contrast Figure. 29.b shows a medium voltage DC collection grid approach in which sections of a solar filed and connected to a DC-DC converter that boost the PV plant voltage of 1500V DC to say 3000V DC. As shown, several groups of PV plants are connected in parallel to form a medium voltage DC collection grid. This particular architecture has several advantages of improved efficiency and the elimination of individual DC-AC inverters as described in reference [27]. The primary disadvantage of employing a fully rated DC-DC boost converter (Figure. 29.b) still exists.

(a)
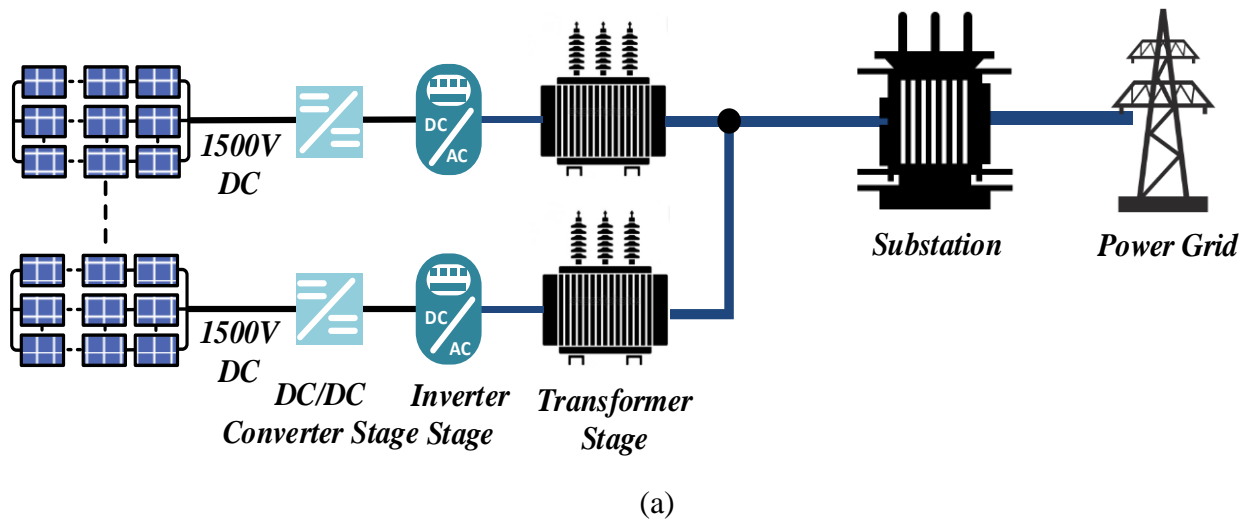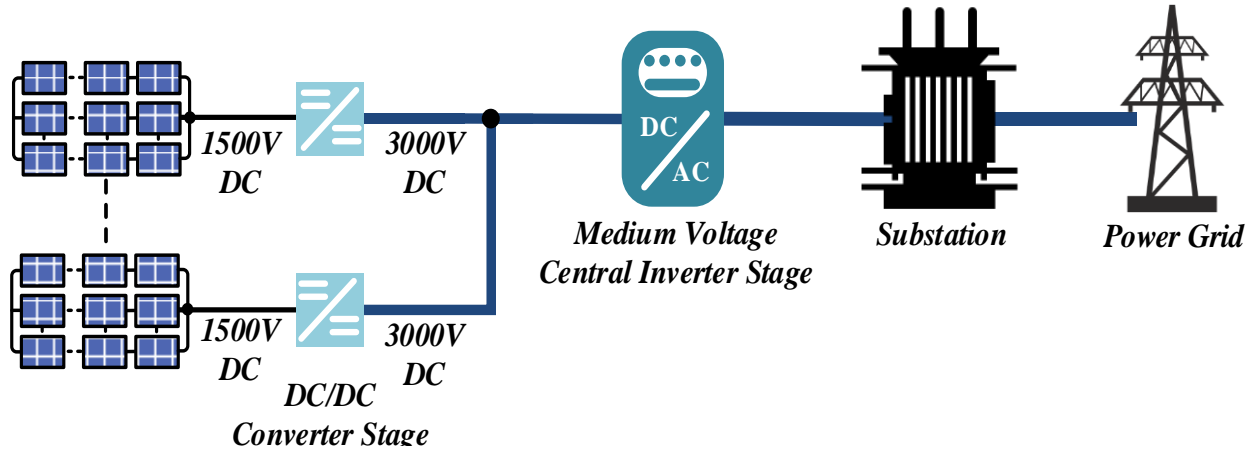
(b)
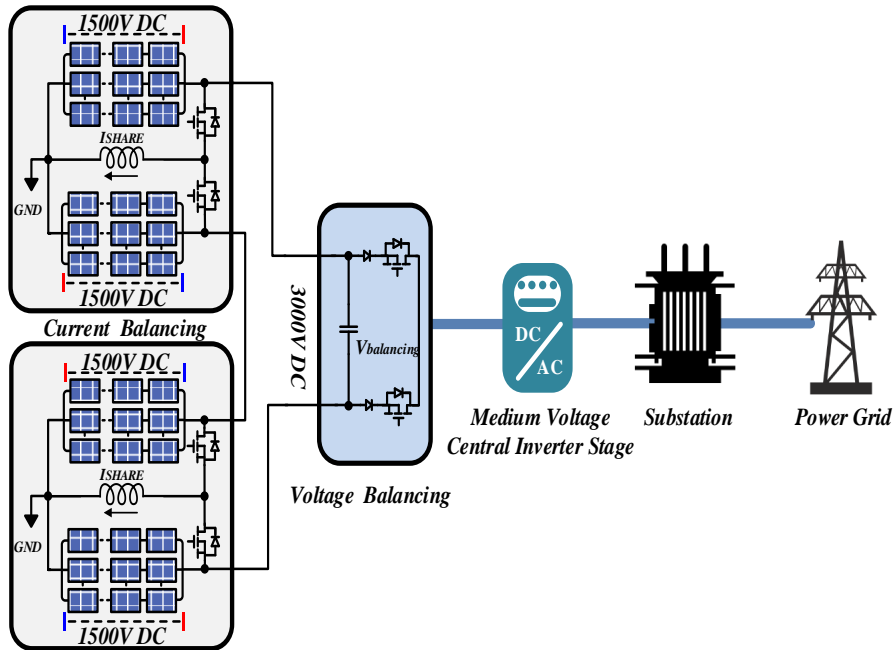
(c)

Figure. 29 Large Scale PV Power collection grid evolution: (a) conventional low voltage DC-Collection grid [43,44]; (b) parallel connected PV groups connected with high power central inverter [45]; (c) proposed new two-stage differential mode power converter.
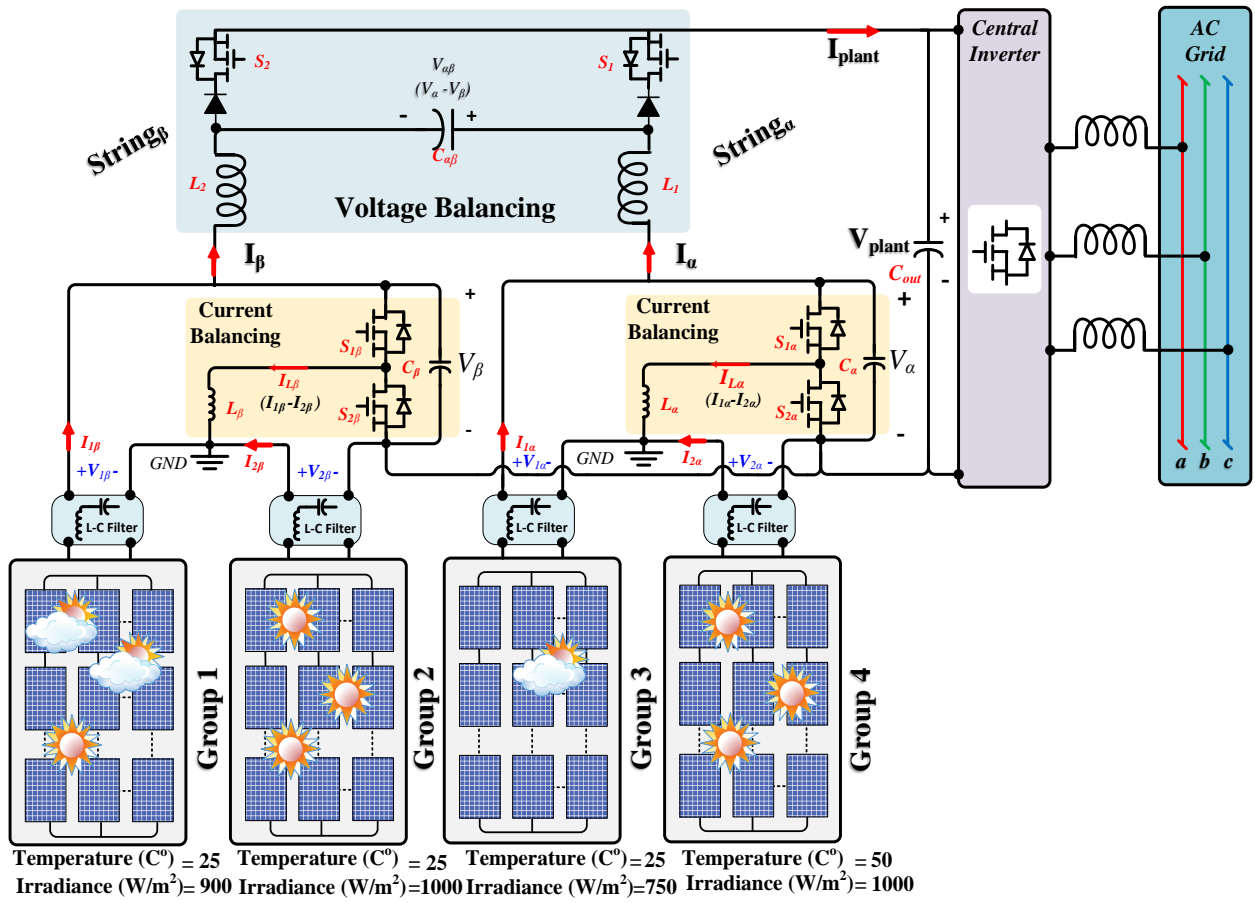
Figure. 30 Two-Stage Differential Power Converter for Large Scale PV Power Plants
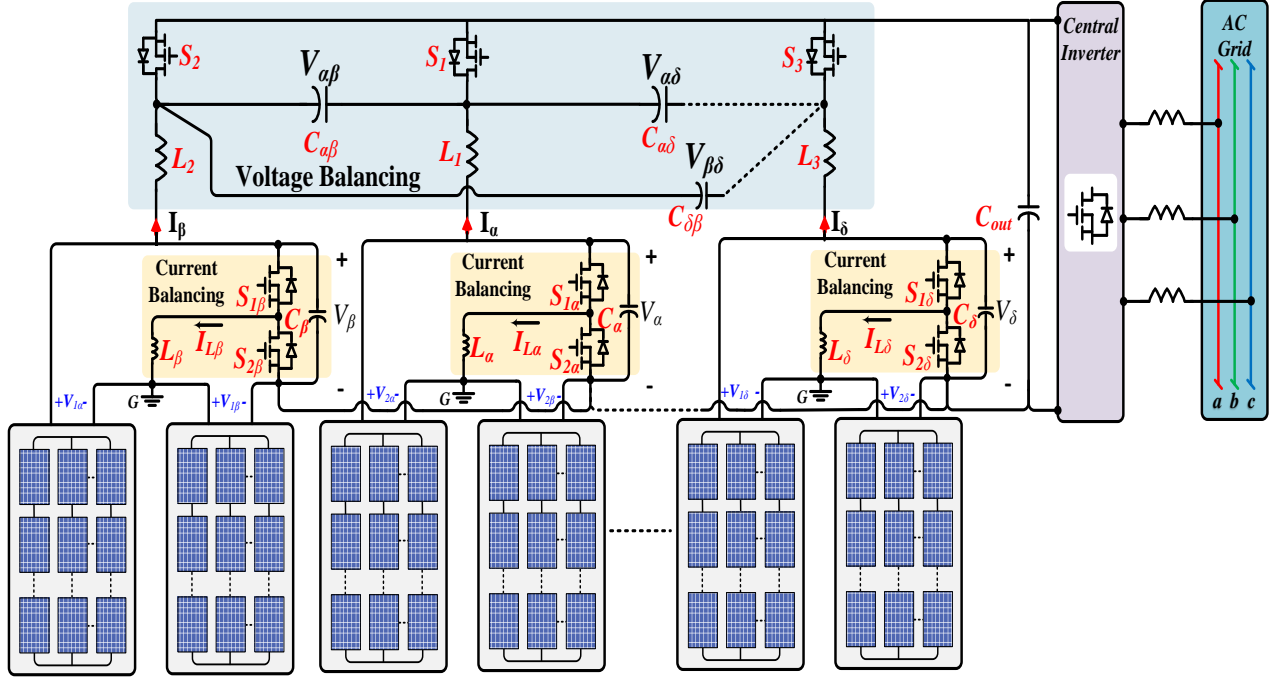
Figure. 31 Scalable architecture of the multistage differential power converter for large-scale PV power plants

In this section, a new two stage differential mode power converter topology is proposed with medium voltage DC collection grid features (Figure. 29.c, Figure. 30 and Figure. 31) [15,16,39,40] . As seen in Figure. 30, two sets of PV plants (Group 1 & 2) are series connected with center point grounded. They are intern connected to a fractionally rated current balancing converter that facilitates independent control of the PV plant currents ($I_{1\beta}$ and $I_{2\beta}$), thereby guaranteeing individual maximum power point tracking (MPPT) for Group 1 & 2 sections of the PV plant. It is noted that the current balancing stage employs two switches ($S_{1\beta}$ and $S_{2\beta}$) that are operated in pulse width modulated (PWM) mode to control the inductor (L_{β}) current $I_{L\beta}$. The current balancing approach processes only a fraction of the total power harvested and requires fractionally rated power converters [15,55]. The current balancing stage processes the differential power from two solar fields .The Group 3 & 4 also have a similar current balancing converter. The

negative output terminals of Group 1&2 and Group 3&4 are connected together to form terminal "c" in Figure. 30. The two positive output terminals "a" and "b" are connected to a voltage-balancing converter as shown in Figure. 30. The function of the voltage balancing stage is to processes the differential power of the two parallel sets: Group 1&2 and Group 3&4 by suitable PWM control of switches S_1 and S_2. The capacitor $C_{\alpha\beta}$ in steady state holds the difference in voltage (V_α -V_β) as shown in Figure. 30. The combination of current and voltage balancing concept presented, guarantees each of the PV plant Groups 1-to-4 to operate at their individual MPPT point, thereby achieving overall maximum power harvesting under partial shading and temperature difference. The overall advantages of the proposed two-stage differential power converter are summarized below:

- Both the current and voltage balancing stages process fractional power to achieve maximum power under partial shading conditions.

- The current balancing stage employs fractionally rated higher voltage and lower current switches while the voltage balancing stage employs higher current lower voltage switches.

- High efficiency is achieved due to fractional power processing compared to other schemes.

- Fewer power processing blocks and lower VA rating of the converter.

- The proposed approach is scalable to several MW rated solar power systems that consists of many groups of PV plants as shown in
  Figure. 31.

- The approach allows for homogeneous and heterogeneous PV power plants employing PV panels from different manufactures.

3.2 Two Stage Differential Converter Analysis

The current balancing stages consist of two PV power plants Groups 1&2 and Groups 3&4 connected in series with their center point ground (Figure. 30). As illustrated in Figure. 30, the current balancing stage for Group 1&2 consists of a half-bridge inverter with switches $S_{1\beta}$ and $S_{2\beta}$ operated in PWM with a duty cycle. When the switch $S_{1\beta}$ is on we have,

$$V_{1\beta} = L_\beta \frac{di_{L_\beta}}{dt} \tag{3.1}$$

and the inductor L_β can be expressed as,

$$L_\beta = \frac{\delta_\beta * V_{1\beta}}{f_{sw}.\Delta I_{L_\beta}} \tag{3.2}$$

Where δ_β is the PWM duty cycle, ΔI_{L_β} is the current ripple and f_{sw} is the switching frequency. The average inductor current $I_{L\beta}$ can be controlled by adjusting the on and off times i.e. duty cycle δ_β of switches $S_{1\beta}$ and $S_{2\beta}$.

Since,

$$I_{1\beta} - I_{2\beta} = I_{L\beta} \tag{3.3}$$

By controlling $I_{L\beta}$ the PV plant Group 1&2 output currents can be controlled thereby regulating their individual MPPT operating points. Further, the total output power of Group 1&2 can be expressed as,

$$V_\beta * I_\beta = V_{1\beta} * I_{1\beta} + V_{2\beta} * I_{2\beta} \tag{3.4}$$

Similar equations can be written for Group 3&4.

Operation of the Voltage Balancing Stage

The voltage balancing stage ensures MPP voltage achieved on each connected PV string by controlling the voltage $V_{\alpha\beta}$ across the capacitor $C_{\alpha\beta}$ as shown in Figure. 30. Voltage balancing stage acts as controllable voltage source to fix the voltage between the two PV strings ($String_\alpha$ and $String_\beta$).

The voltage balancing stage extracts the maximum power available from each string by adjusting the duty ratio between S_1 and S_2 as shown in Figure. 30 such that,

$$\delta_{s1} + \delta_{s2} = 1 \tag{3.5}$$

Where the duty ratio of the voltage balancing stage can be calculated based on the available current extracted out of each of the current balancing stage given by,

$$\delta_{s1} = \frac{I_\beta}{I_\alpha + I_\beta} \tag{3.6}$$

Controlling the ON/OFF time on the switches S_1 and S_2 ensures realizing the MPP voltage on each connected PV string by regulating the voltage magnitude and polarity. MPP voltage is achieved by setting $V_{\alpha\beta}$ equal to the voltage difference between the maximum voltage string available on V_α and V_β as shown in Figure. 30 can be expressed as,

$$V_{\alpha\beta} = V_{\alpha,max} - V_{\beta,max} \tag{3.7}$$

The general equation of the current across the capacitor $C_{\alpha\beta}$ is given by,

$$i_{c_{\alpha\beta}} = C_{\alpha\beta} * \frac{dV_{\alpha\beta}}{dt} = C_{\alpha\beta} * \frac{\Delta V_{\alpha\beta}}{\delta_{S1} T} \tag{3.8}$$

51

Such that,

$$i_{c_{\alpha\beta}} = I_\alpha - I_\beta \tag{3.9}$$

To design the capacitor value needed for the voltage balancing stage, the following formula can be used,

$$C_{\alpha\beta} = (I_\alpha) \frac{\delta_{S1}}{f_{sw} \Delta V_{\alpha\beta}} \tag{3.10}$$

Where f_{sw} is the converter switching frequency and $\Delta V_{\alpha\beta}$ is ripple required on the capacitor.

The inductors (L_1, L_2) can be expressed as,

$$L_1 = \left| -V_{Plant} + V_\beta \right| * \frac{(1 - \delta_{s1})}{f_{sw} * \Delta I_{L_\beta}} \tag{3.11}$$

Similar equation can be written for L_2

Similarly, to current balancing stage, the voltage balancing stage decoupled the two input voltages from both $String_\alpha$ and $String_\beta$. Each string operates independently from other. The plant output voltage V_{Plant} can be expressed as,

$$V_{Plant} = \frac{P_{Plant}}{I_{Plant}} = \frac{P_{in\alpha} + P_{in\beta}}{I_\alpha + I_\beta} \tag{3.12}$$

$$V_{Plant} = \frac{(V_{1\alpha} I_{1\alpha} + V_{2\alpha} I_{2\alpha}) + (V_{1\beta} I_{1\beta} + V_{2\beta} I_{2\beta})}{I_\alpha + I_\beta} \tag{3.13}$$

The proposed architecture is scalable to multiple inputs with effective localized power management ability for multi-strings PVs, residential, and large-scale PV power plants. The bulk

power is processed once with fraction losses. The balancing capacitors $C_{\alpha\beta}, C_{\alpha\delta}$, $C_{\beta\delta}$ play a vital role in balancing the voltages between different strings to achieve the MPP, while L_α, L_β, and L_δ play a vital role in balancing the current between the PV groups at input as shown in Figure. 31. This proposed approach effectively eliminated the DC/DC converter needed to track the MPPT.

3.3 Control Strategy

To achieve the maximum power point for the system, Figure. 32 presents the system control strategy needed. Figure. 32 shows the system expected instantaneous available power by calculating the expected maximum current and voltage. Base on the expected values of current and voltage, the current balancing stage is operated, and the voltage balancing stage is operated.
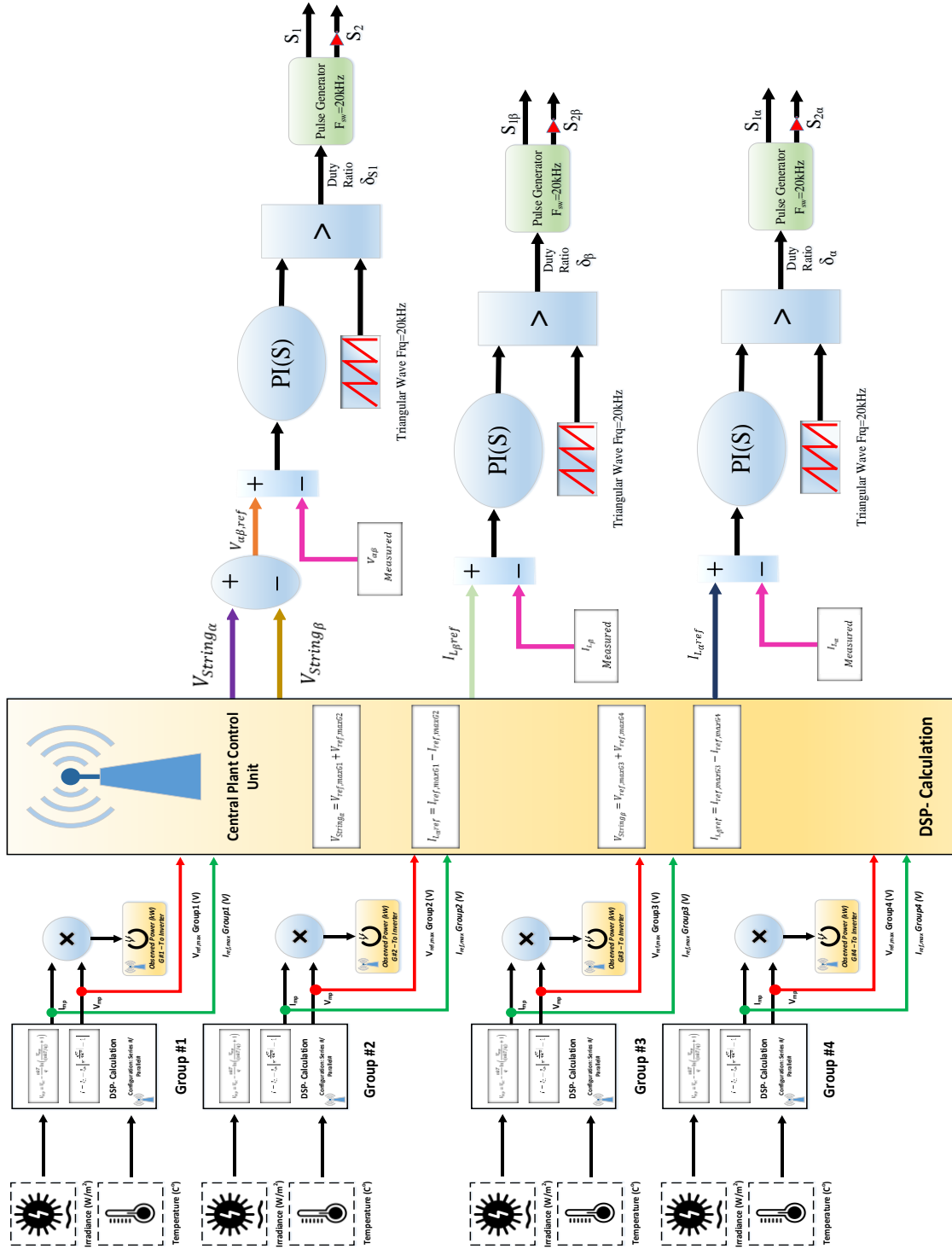
Figure. 32 System Control Strategy to achieve maximum power in for the voltage and current balancing stages.

3.4 Design Example

In this section, 1.1MW homogenous and heterogeneous PV plants' designs are illustrated using the proposed approach shown in Figure. 30.

3.4.1 Homogeneous PV Plant Design:

A homogenous PV plant is defined as a plant that has equal number of series/parallel-connected modules per group from a single manufacturer. In this example, a 1.1 MW PV plant design is explored. Table 4 shows the overall plant capacity, and PV module manufacturer.

Table 4 Homogenous PV Plant Design Specifications (Figure. 30 Two-Stage Differential Power Converter for Large Scale PV Power Plants)

Homogenous PV Plant Design	
PV Module**	SunPower SPR-305-WHT; Each module rated at $V_{mp} = 55$ V and $P_{max} = 305$ Watts (Appendix I Fig. 9 has data points for other operating conditions).
Configured in 4 Groups (1,2,3,4)**	Each Group has 24 Series/ 40 Parallel modules with rated power = 293 kW
Total Plant Capacity for 4 Groups (MW)**	1.1 MW
Switching frequency of current balancing stage	20 kHz
Inductor L_α, L_β assuming a current ripple (ΔI_{L_β}, ΔI_{L_α}) of 10% (Eq. 2)	1.65mH
Switching frequency of voltage balancing stage	20 kHz
Capacitor $C_{\alpha\beta}$ assuming a voltage ripple ($\Delta V_{\alpha\beta}$)of 10% (Eq. 10)	40uF
Inductor L_1, L_2 assuming Current ripple (ΔI_{L_β}, ΔI_{L_α}) of 10% (Eq. 11)	100uH
*** Condition at 25C^0 and 1 kW/m^2*	

The module I-V/P-V curves are shown in the Appendix I. As illustrated in Figure. 30, Group-1 through Group-4 are assumed to be under different operating conditions due to environmental factors. Figure.33.a and Figure.33.b show the operating characteristics of each group at different temperature and insolation conditions. From the literature review its proven that there is a single unique operating condition i.e. voltage/current for each group to extract maximum power. Table 5 tabulates these operating conditions. Both current/voltage balancing converters in Figure. 30 are operated with their specific switching duty cycles such that the available maximum power is extracted. Figure. 34 to Figure. 36 illustrate these results. The proposed converter topology in Figure. 30 is therefore capable of operating a large-scale PV plant grouped in four, at different maximum power point as shown in Figure 34.(a). Figure.31 extends the topology reach to several multiple groups.
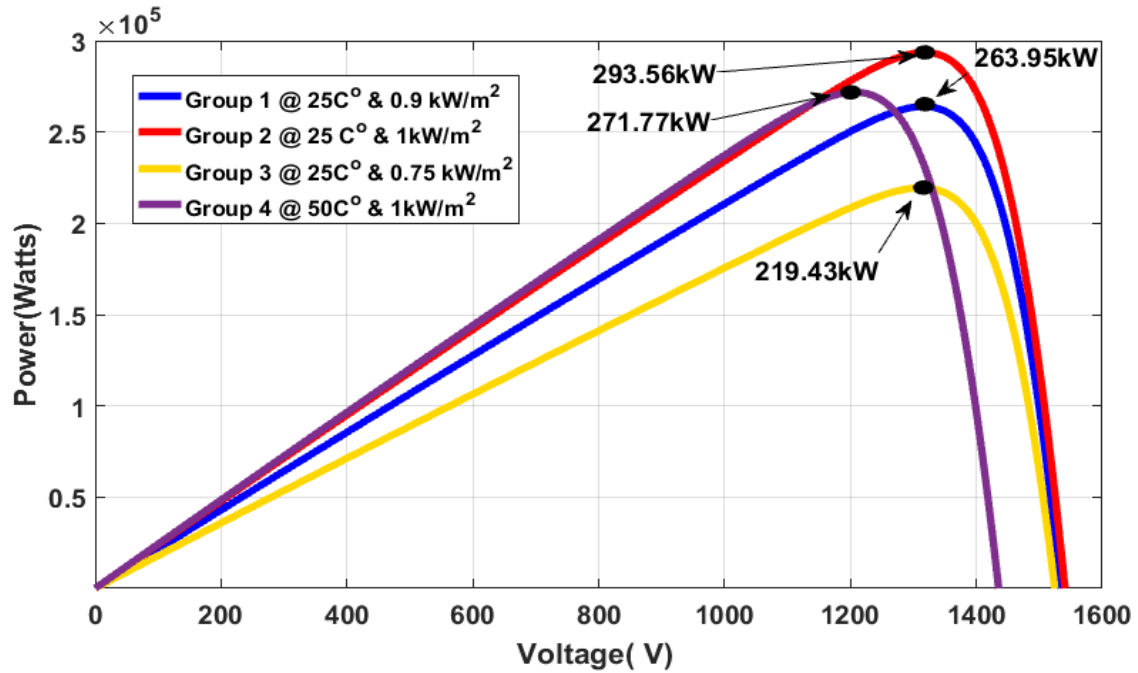
(a)
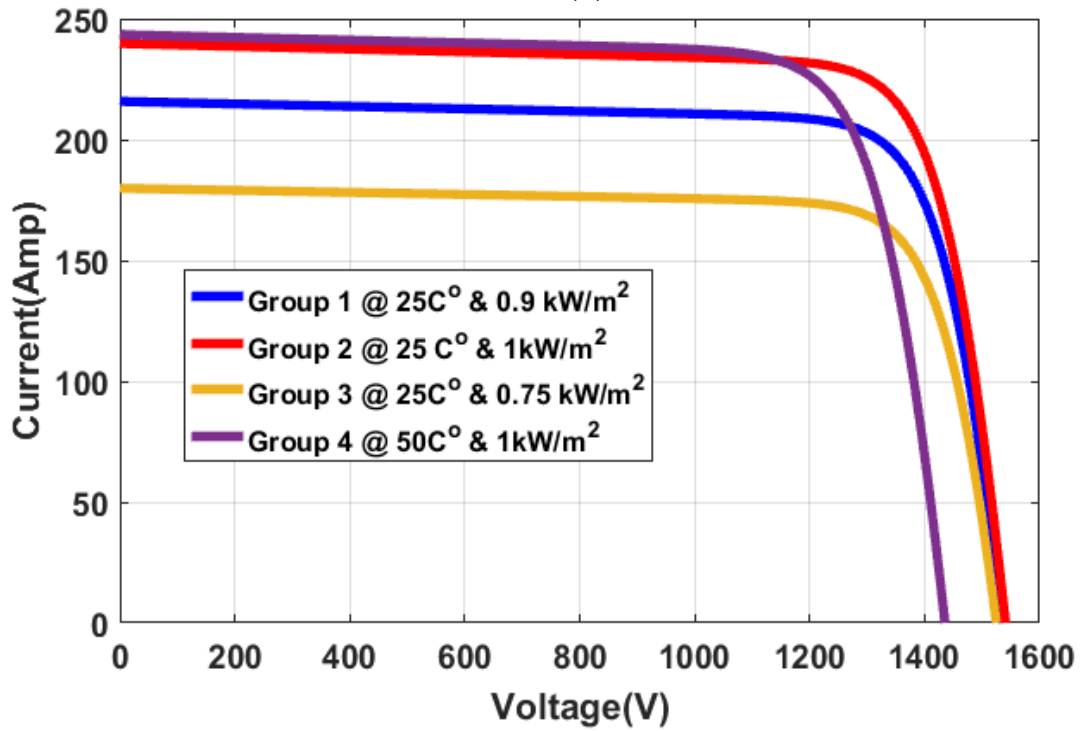
(b)

Figure. 33 Groups Specific Operational Curves (a) P-V Curve (b) I-V Curve
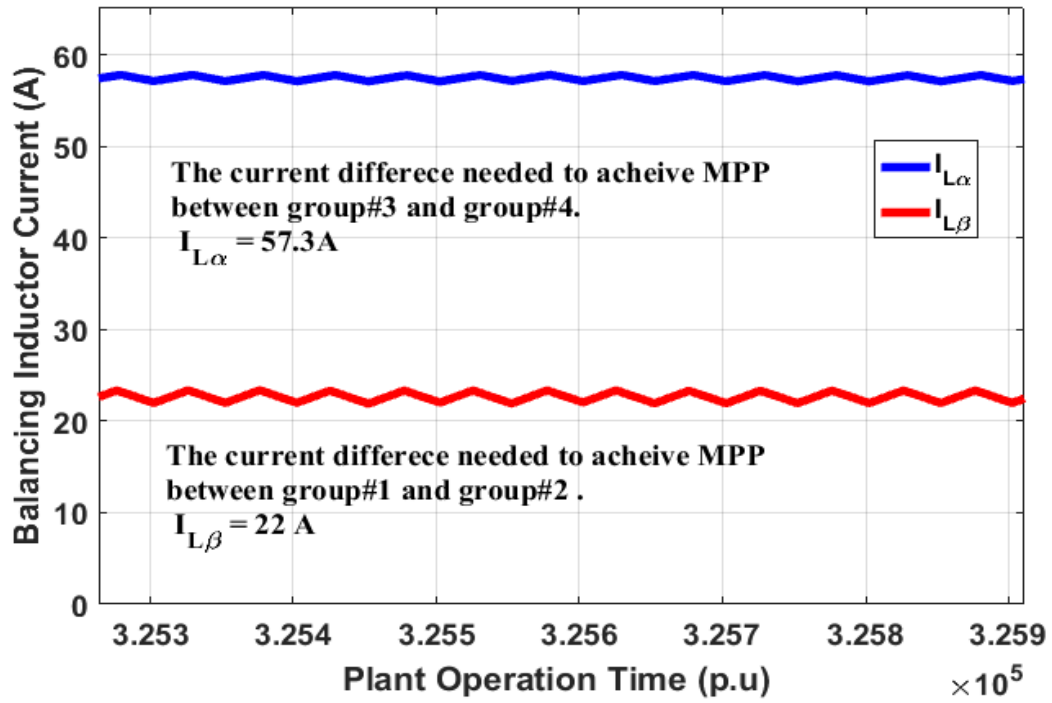
Figure. 34 Maximum balancing currents for the proposed plant design in Figure. 29 needed to achieve the independent maximum operating point (a) the inductor current ($I_{L\alpha}$) , (b) the inductor current ($I_{L\beta}$).

The voltage difference needed to acheive MPP beteeen Group 1 and Group 2 (String$_\beta$) and Group 3 and Group 4 (String$_\alpha$). The need voltage balance required is -114.3 which is the difference the maximum available voltage in String$_\alpha$ and in String$_\beta$ as show in Fig.2
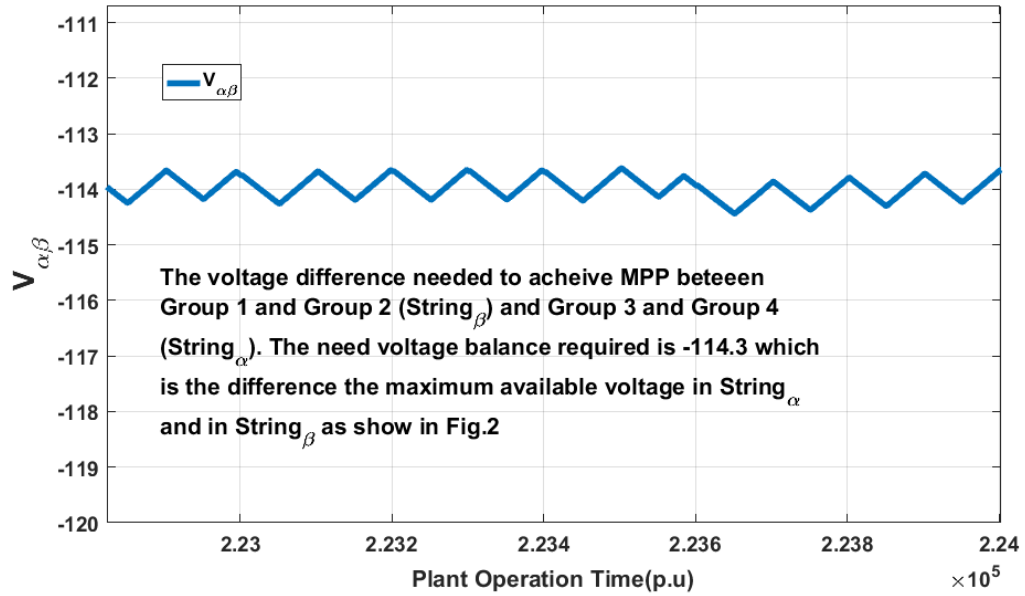
Figure. 35 Maximum balancing voltage (V$_{\alpha\beta}$) for the proposed plant design in Fig. 29 needed to extract the maximum available power.
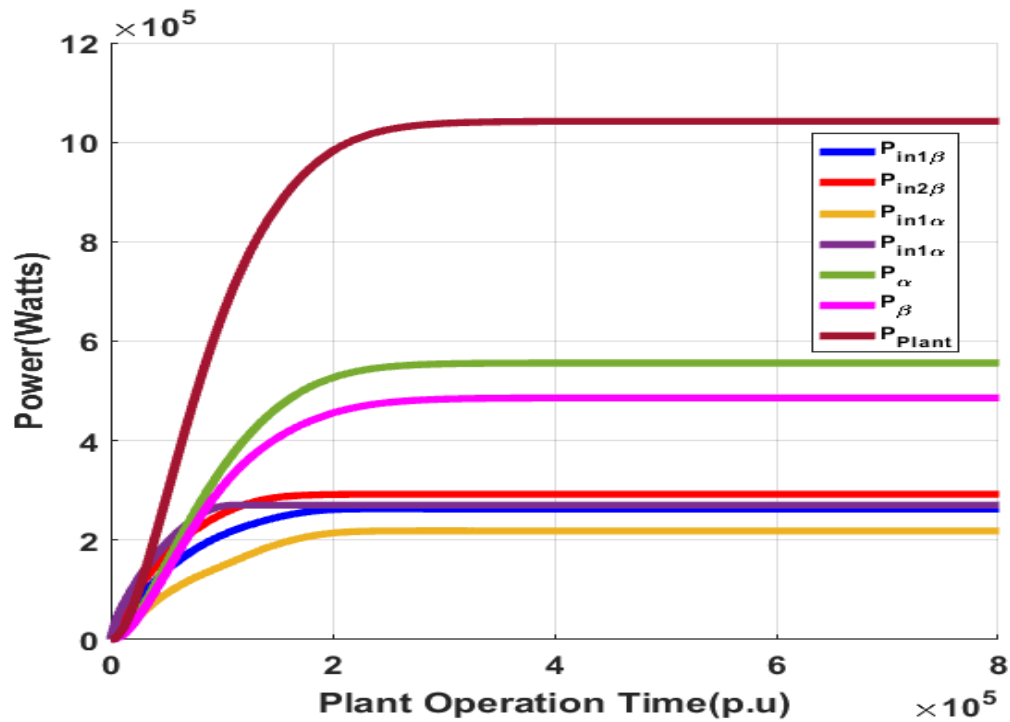
Figure. 36 The harvested power from each group under different environmental condition

59

Table 5 Detailed operational analysis of the proposed two-stage differential mode power converter for large scale PV plant as shown in Figure. 30.

String	Group #	Voltage(V) / Current(A)	Balancing Current (A) / String Voltage (V)	String Currents (A)	Voltage Balancing (V)	Available Solar Power	Balancing Converter Rating — Current Stages	Balancing Converter Rating — Voltage Stage
String β	G1	$V_{1\beta}$= 1323 V / $I_{1\beta}$= 199 A	$I_{L\beta}$=22 A	I_{β}= 210 A	$V_{\alpha\beta}$= -114 V	556 kW	29 kW (5.24%)	24 kW (2.3%)
String β	G2	$V_{2\beta}$= 1325 V / $I_{2\beta}$=221 A	V_{β}=2648V					
String α	G3	$V_{1\alpha}$=1319 V / $I_{2\alpha}$=166 A	$I_{L\alpha}$= 57 A	I_{α}= 193 A		486 kW	76 kW (15.5%)	
String α	G4	$V_{2\alpha}$=1215 V / $I_{2\alpha}$=223 A	V_{α}=2534 V					

From Table 5, it is clear that the current balancing stage for String$_\beta$ and String$_\alpha$ handle currents of $I_{L_\beta} = 22$A and $\Delta I_{L_\alpha} = 57.3$A a fraction of the total current. Further, the voltage balancing circuit is shown to operate at $V_{\alpha\beta} = -144$ V, which is again a much smaller value. Therefore, the amount of volt-amps processed by current/voltage balancing stages is small for the realistic example of operation at different temperature and insolation conditions.

3.4.2 Heterogeneous PV Plant Design:

Heterogeneous PV plant is defined as a plant with different number of series-parallel connected modules from more than one manufacturer. In this example, a 1.1 MW PV plant design is explored. Table 6 shows the overall plant capacity, the PV module manufacturers, and configurations.

Table 6 Heterogonous PV Plant Design Specifications (Figure. 30)

Heterogonous PV Plant Design	
PV Module Group (1,2)**	SunPower SPR-305-WHT; Each module rated at V_{mp} = 54.7 V and P_{max} = 305 Watts (Appendix I Fig. 9 has data points for other operating conditions).
Group (1,2)** Configuration	Each Group has 24 Series/ 40 Parallel modules with rated power = 294 kW
PV Module Group (3,4)**	Shanghai Topsolar Green Energy TSM72-156M [47] 305W; Each module rated at V_{mp} = 36.2 V and P_{max} = 305 Watts (Appendix I Fig. 10 has data points for other operating conditions).
Group (3,4)** Configuration	Each Group has 34 Series/ 27 Parallel modules with rated power = 292 kW
Total Plant Capacity for 4 Groups (MW)**	1.1 MW
Switching frequency of current balancing stage	20 kHz
Inductor L_α, L_β assuming a current ripple (ΔI_{L_β}, ΔI_{L_α}) of 10% (Eq. 2)	1.65mH
Switching frequency of voltage balancing stage	20 kHz
Capacitor $C_{\alpha\beta}$ assuming a voltage ripple ($\Delta V_{\alpha\beta}$)of 10% (Eq. 10)	40uF
Inductor L_1, L_2 assuming Current ripple (ΔI_{L_β}, ΔI_{L_α}) of 10% (Eq. 11)	100uH
** *Condition at $25C^0$ and 1 kW/m^2*	

The module I-V/P-V curves are shown in the Appendix I in Fig. 10. As illustrated in Figure. 30, Group-1 through Group-4 are assumed to be under different operating conditions due to environmental factors. In addition, since the plant is heterogeneous; therefore, Groups (1, 2) have different series-parallel configuration than Groups (3, 4). The groups' operation curves are shown in Figure. 37.a and Figure. 37.b. Similar to homogenous plants, heterogeneous plants have unique

operating conditions i.e. voltage/current for each group has to be matched to extract the maximum power available.

Since the operating curves in Figure. 37.a and Figure. 37.b are similar in characteristics to these in Figure.33.a and Figure.33.b, each converter operates at their specific duty cycles such that the available maximum power is extracted. Therefore, the proposed converter topology in Figure. 30 is capable of operating a heterogeneous large-scale PV plant grouped in four, at different maximum power point as shown in Appendix I.
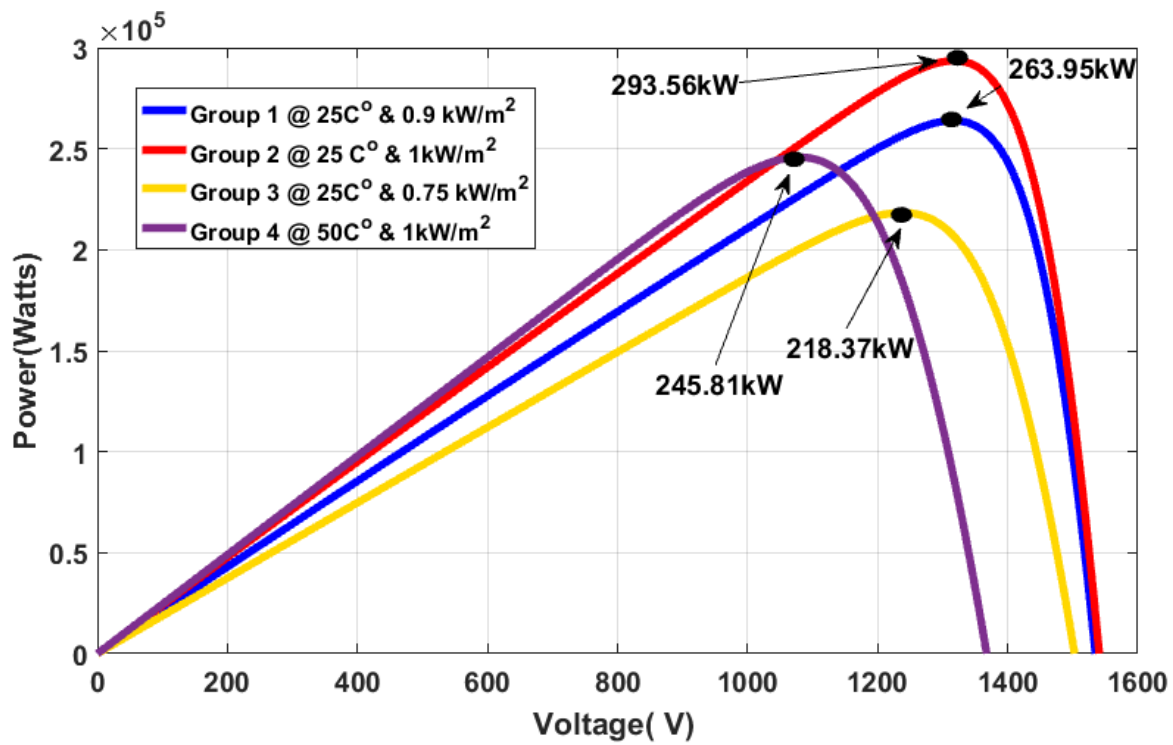
(a)
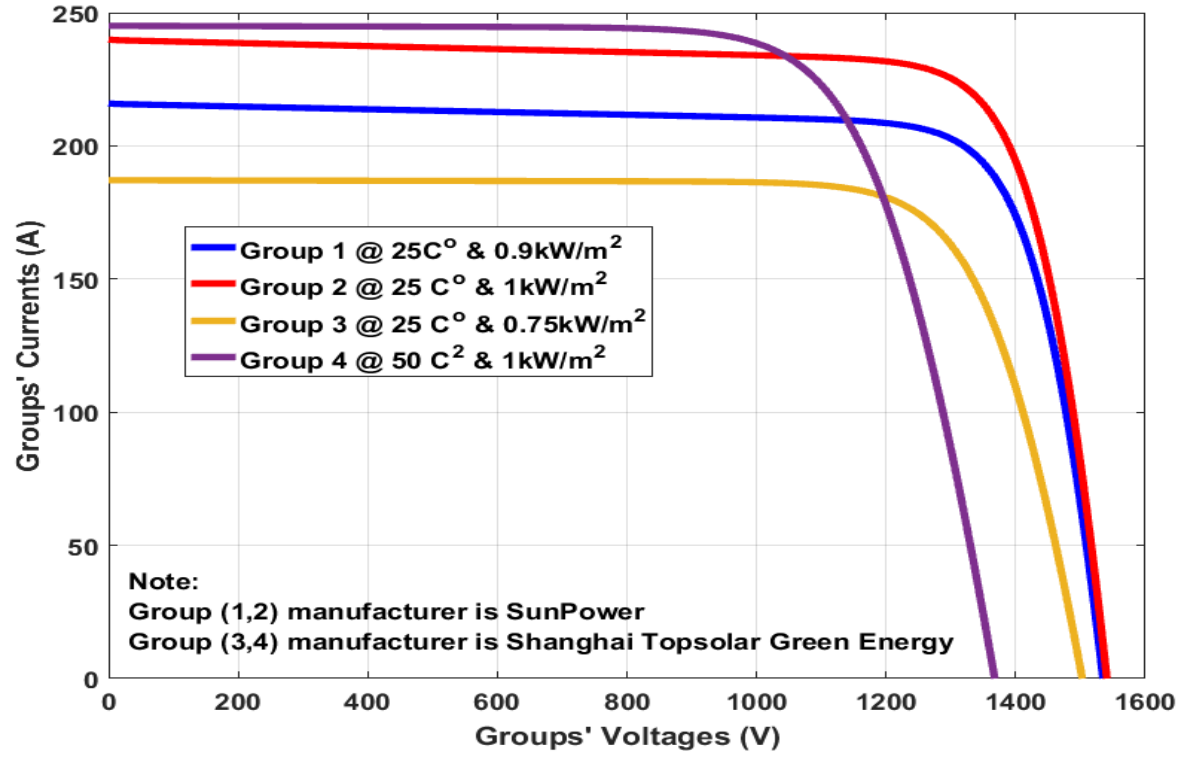
(b)

Figure. 37 Groups Specific Operational Curves (a) P-V curve (b) I-V curve.

3.5 Conclusion

In this section a new two-stage differential converter to enable higher energy yield for large scale solar power plants has been proposed. It has been shown that current balancing and voltage balancing schemes process fractional power and allow groups of PV fields to operate at their maximum power when subjected to environmental conditions. The proposed approach has been shown to be scalable to MW rated PV plants subdivided into many groups. Further, it has been shown that the approach can accommodate PV panels from different manufacturers. A design example and simulation results demonstrate the effectiveness of the scheme for a 1 MW plant.

63

IV. APPLICATION-III: DUAL PHASE OUTPUT 4-LEG INVERTER WITH ACTIVE DECOUPLING AND INTEGRATED POWER OPTIMIZER FOR OFF-GRID APPLICATIONS

4.1 Introduction

The solar market has been growing quickly and consistently, averaging 59% growth each year over the past decade [48]. Approximately 1.2 billion people who still lack electricity worldwide, the clear majority lives in rural areas [49]. In remote areas of developing countries e.g Chile, Ecuador, Peru, and India, where grid expansion is unviable, off-gird Photovoltaic (PV) systems can be alternative solution to meet their demands [50]. This increases the needs for dynamic power electronics solutions that are flexible enough to integrate and manage multiple distributed PV power generation (DPG) points with the different types of off-grid loads without affecting reliability and power quality. Furthermore, operating multiple voltage sources in parallel pose control and load sharing challenges [51]. The solution would be a system optimizes power harvesting and invert power from variable DC-AC while maintains operation at maximum power point (MPP) and reduces the effects of partial shading. Reference [19,35] discusses several commercially viable PV plants architectures and recommends a string inverter as the most efficient solution with distributed MPPT. String inverters and other type of inverters have an inherent problem of unbalanced instantaneous power between the dc side and ac side of the converter, which is time varying with a double line frequency variation [22].

To actively compensate for twice the frequency power ripple in the dc-link, reference [52] presents several techniques that actively decouple the double line frequency for only single-phase outputs using different types of power electronics circuits and controllers. The majority of the presented solutions are developed for unidirectional power flow and only a few addressed split DC inputs. A common approach introduces third leg on the inverter side to transfer the power ripples. Reference [53] analyzes a new single-phase three-leg inverter with a single additional leg for active decoupling; however, the approach only demonstrates compensation of the double line frequency power ripple for linear loads.

This section proposes an off-grid integrated dual phase output inverter with active power decoupling and power optimization, which is a viable solution to the problem of double line frequency ripple for a typical home/building [54]. The proposed system dynamically optimizes power consumption by actively mitigating the power ripples on the AC side and efficiently manages the input power between the PV power plant and the battery pack. The main advantages of the proposed overall system:

- Actively compensates for the double line frequency power ripple for different load conditions e.g. non-linear, balanced and unbalanced loads with dual phase output designed for 120V and 240V.

- Mitigates the double line frequency power ripple generated from each phase using a robust control topology resulting in a smaller size dc-link capacitor

- Dynamic power optimization technique allows charging and discharging of voltage input energy storage units.

65

- Increased operational flexibility, full utilization of the input power resources, and cost effectiveness.

4.2 Active Decoupling Techniques from the literature

This section focuses on reviewing several active decupling techniques used for PV systems in solving the problem of double line frequency, reducing the DC-link capacitor size needed, and achieving higher energy densities[53].

4.2.1 General Solution

A typical single-phase voltage source inverter presented in Figure. 38. A huge electrolytic C_{link} capacitor used to eliminate the double-line frequency power ripple generated due to the load. The ac side voltage and current are presented in the following equations 4.1 and 4.2.

$$V_{ac}(t) = V_{ac} \sin \omega t \tag{4.1}$$

$$i_{ac}(t) = I_{ac} \sin(\omega t + \varphi) \tag{4.2}$$

Where V_{ac} and i_{ac} are the peak values for the voltage and the current at the ac side of the circuit, and ω is the angular frequency of the load, and φ is the phase difference between the voltage and current. On the other hand, the DC side would have the following instantaneous power equation as shown in equation 4.3 and presented in

Figure. **39**.

$$P_{dc}(t) = P_{ac}(t) + P_L(t) \tag{4.3}$$

$$= V_{ac}(t)i_{ac}(t) + V_L(t)i_{ac}(t) \tag{4.4}$$

$$= \frac{V_{ac}I_{ac}}{2} \cos \varphi - \frac{V_{ac}I_{ac}}{2} \cos(2\omega t + \varphi) + \frac{1}{2}L\omega I_{ac}^2 \sin(2\omega t + 2\varphi) \tag{4.5}$$

$$= P_{constant} + P_{ripple} \tag{4.6}$$

Where the double-line frequency P_{ripple} is made of the ripple power from both ac side and dc side, $P_{constant}$ is power consumed by the load, and L is the inductor of the filter at the ac side. The $P_{constant}$ is always positive as shown in

Figure. 39 when the system operated in invertor mode and the power flow from the dc side to the ac side. If the proposed system in Figure. 38 acts like a rectifier then $P_{constant}$ is negative. Since the ripple power from the filter inductor is less one tenth of the total power ripple, therefore, it can be neglected for simplicity.

For the capacitor to compensate for the total power ripples, the following power equation for the energy stored across the capacitor:

$$P_{Clink} = V_{clink} i_{clink} = \frac{1}{2} C_{link} \frac{d(V_{clink}(t)^2)}{dt} = P_{ripple} \tag{4.7}$$

Where, V_{clink} is the voltage across the decoupling capacitor and the i_{clink} is the current across the decoupling capacitor.

Solving equation 4.7, the following solution produced,

$$V_{clink}(t)^2 = A + \frac{V_{ac}I_{ac}}{2\omega C_{link}} \sin(2\omega t + 2\varphi) \tag{4.8}$$

A is the time-constant value since the voltage ripple value is above zero. Therefore, if A is:

$$A = \frac{V_{ac}I_{ac}}{2\omega C_{link}} \tag{4.9}$$

Then,

$$V_{clink}(t) = A_1 \sin(\omega t + \varphi_1) \tag{4.10}$$

The complete solution for the differential equation when $A > \frac{V_{ac}I_{ac}}{2\omega C_{link}}$ is as shown in

equation 4.11:

$$V_{clink}(t) = A_0 + \sum_{k=2}^{n} A_k \sin(k\omega t + \varphi_k)$$ (4.11)

Such that n= 2,3,4…etc. The $V_{clink}(t)$ has high value harmonics at higher orders and these will introduce to the system the circulated unwanted power ripples. In order for us to get rid of the circulated double-line frequency ripples, the voltage across the decoupling leg should be match the following equation 4.10.

$$V_{clink}(t) = A_0 + A_2 \sin(2\omega t + \varphi_2)$$ (4.12)

Therefore, three general solutions found:

$$Solution\ 1 - \quad V_{clink}(t) = A_1 \sin(\omega t + \varphi_1)$$ (4.13)

$$Solution\ 2 - \quad V_{clink}(t) = A_0 + A_2 \sin(2\omega t + \varphi_2) \quad \text{For } A_0 \gg A_2$$ (4.14)

$$Solution\ 3 - V_{clink}(t) = |A_1 \sin(\omega t + \varphi_1)|$$ (4.15)

Each of the proposed solutions would have waveform to compensate for the generated ripple as shown in Figure. 40. Based on the three general solutions each of them would have a specific value for the required capacitance value for the Clink such that the double-line frequency ripple compensated.
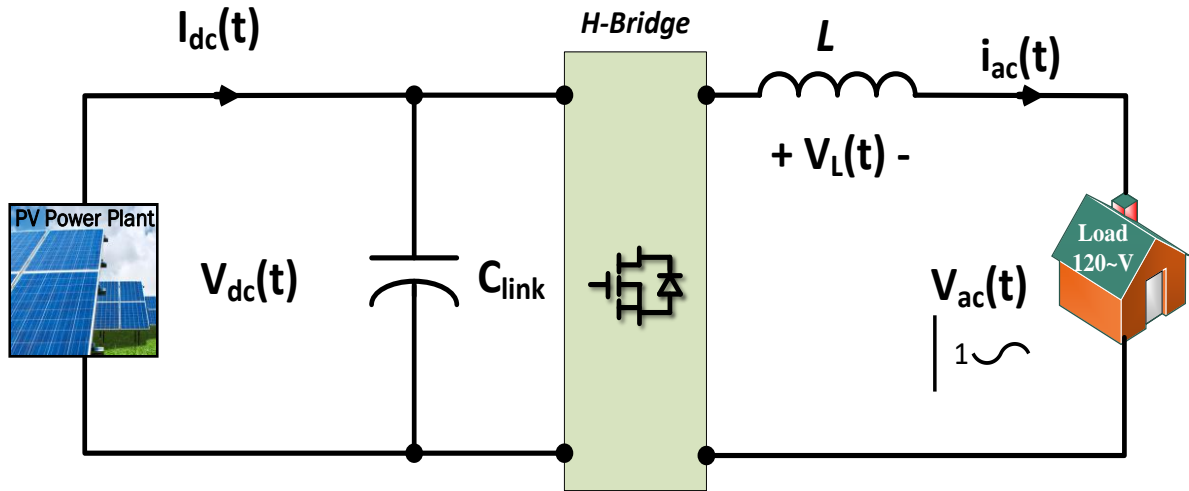
Figure. 38 Single Phase PV system with double-line frequency compensator where typical H-bridge rectifier plugged in.
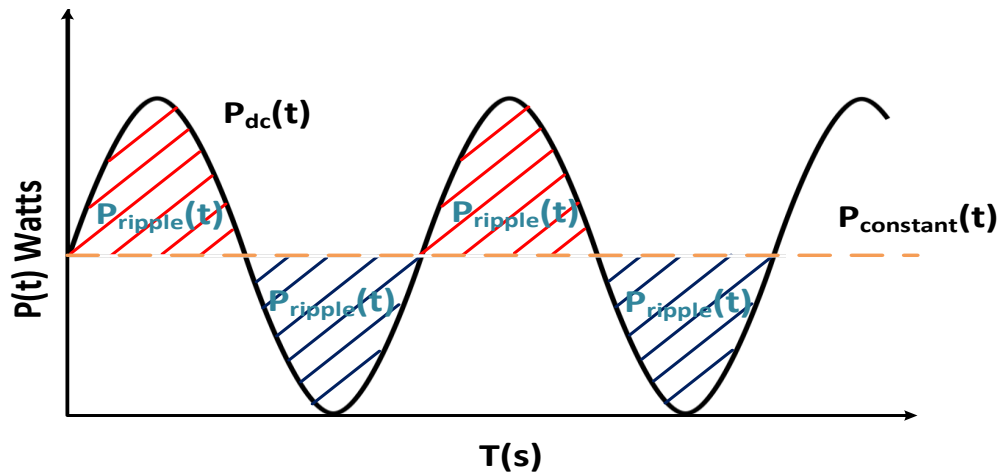
Figure. 39 Power ripple generated due to the double-line frequency in a single-phase system and the instantaneous power $P_{dc(t)}$ between the DC and AC side.
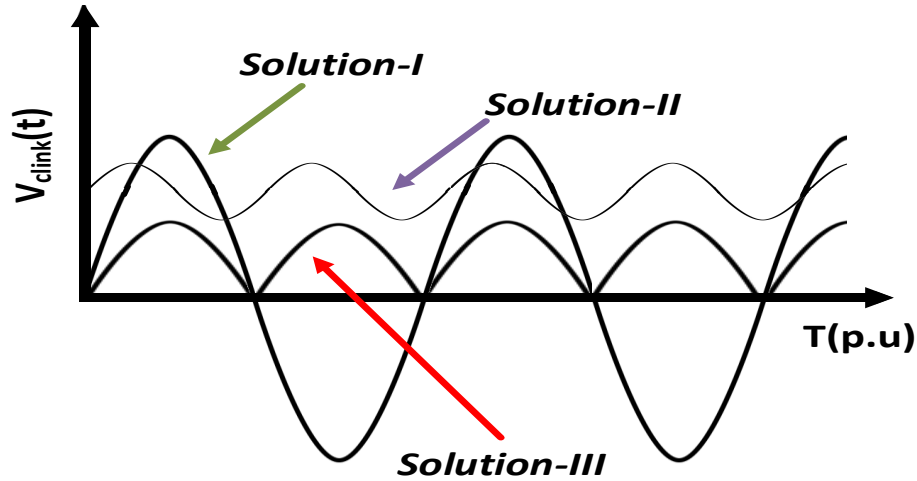
Figure. 40 Required Voltage Solutions for decoupling the power ripples due to the double-line frequency effect.

4.3 Active Decoupling 4 Leg Inverter Modeling and Control

The active decoupling is highly needed in residential, commercial, and industrial power applications such as grid-connected inverters from renewable energy sources, uninterruptible power supplies, light-emitting diodes driver where the double line frequency ripple became serious issue to be addressed in single-phase rectifiers and inverters. A typical solution for the problem is to plug in a big capacitor size and most of the used capacitors are bulky electrolytic capacitors. These electrolytic capacitors have short life times and result in low efficiency systems. Therefore, research picked up on developing control techniques that reduce the size of the capacitor, build compact systems, and enable developing higher energy density systems as shown in Figure. 41.
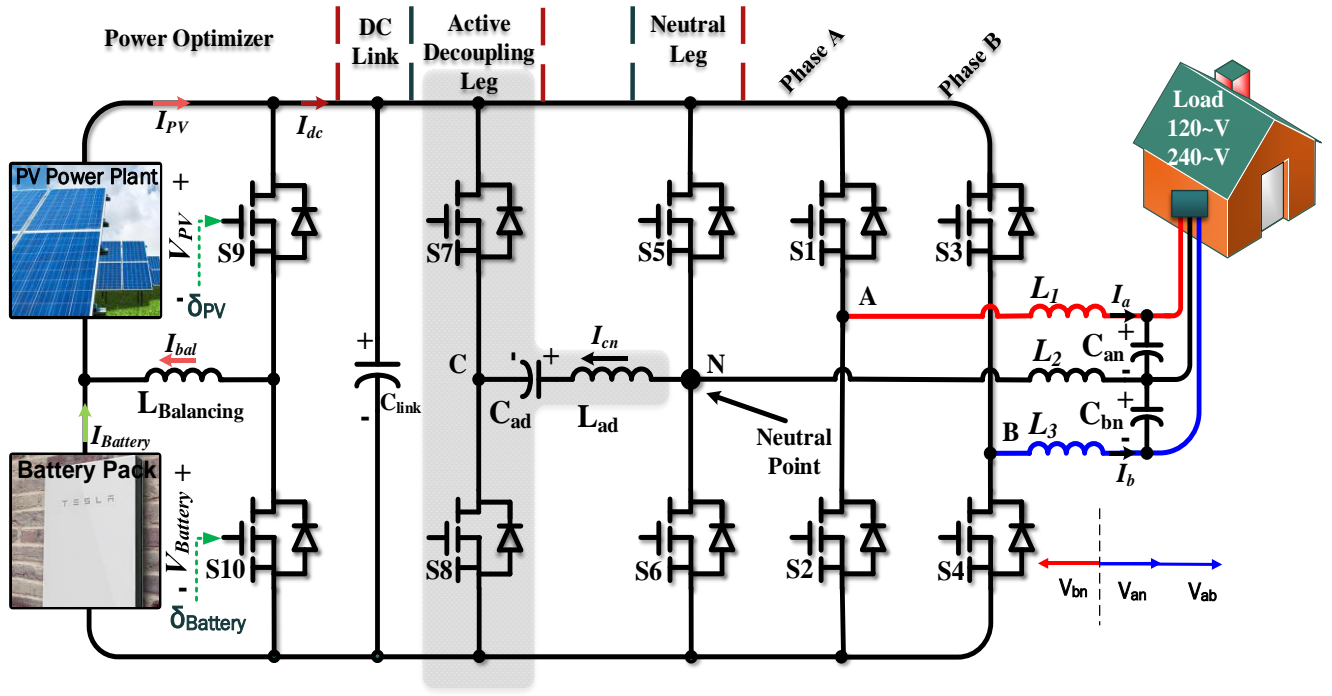
Figure. 41 Proposed dual phase four leg inverter with active decoupling and integrated power optimizer.

To actively decouple power ripples generated by different load conditions, the currents across phase A and B are shown in equations 4.16 and 4.17, and the generated power ripples across phase A and B are calculated as shown in equations 4.18 and 4.19,

$$i_a = I_{a,max} \sin(\omega t + \phi_a) \tag{4.16}$$

$$i_b = I_{b,max} \sin(\omega t + \phi_b) \tag{4.17}$$

$$P_{an} = -\frac{V_{an}I_a}{2}\cos(2\omega t + \phi_a) \tag{4.18}$$

$$P_{bn} = -\frac{V_{an}I_b}{2}\cos(2\omega t + \phi_b) \tag{4.19}$$

Since leg C is the compensating leg, the total power ripple generated by Phase A and B should be processed through Leg C as shown in Figure. 41.Therefore, the voltage V_{cn} and current I_{cn} is determined by equation 4.20, and 4.21 respectively. The current and voltage in the decoupling phase consist of two components, α and β, which correspond with the double line frequency ripple generated from phase A and B respectively such that the necessary compensating power ripples in the active decoupling leg (CN) is set to equation 4.22. The resulting power equation has a third component that depends on the magnitude and phase of both the α and β components. These components must sum to the value of the second harmonic components across phase A and B. The solutions of these equations are reported below and shown in Figure. 42.

$$I_{cn} = I_\alpha \sin\left(\omega t + \theta_\alpha - \frac{\pi}{2}\right) - I_\beta \sin\left(\omega t + \theta_\beta - \frac{\pi}{2}\right) \qquad (4.20)$$

$$V_{cn} = V_\alpha \sin(\omega t + \theta_\alpha) - V_\beta \sin(\omega t + \theta_\beta) \qquad (4.21)$$

$$P_{cn} \approx \frac{\omega C V_\alpha^2}{2} \cos\left(2\omega t + 2\theta_\alpha - \frac{\pi}{2}\right) + \frac{\omega C V_\beta^2}{2} \cos\left(2\omega t + 2\theta_\beta - \frac{\pi}{2}\right) +$$

$$\frac{2\omega C V_\alpha V_\beta}{2} \cos\left(2\omega t + \theta_\alpha + \theta_\beta - \frac{\pi}{2}\right) \qquad (4.22)$$

Thus, for the controller to adjust itself to achieve the right V_{cn} and I_{cn}, the above equations when solved algebraically, will give the phase and magnitude needed for each compensation component (α and β) to achieve active ripple cancelation base on equations 4.23, 4.24, 4.25, and 4.26.

$$\theta_\alpha = \frac{\phi_a}{2} + \frac{\pi}{4} \qquad (4.23)$$

$$\theta_\beta = \frac{\phi_b}{2} + \frac{\pi}{4} \qquad (4.24)$$

$$V_\alpha = \sqrt{\frac{V_{AN}I_{A,max}\sqrt{\cos(\theta_\beta - \theta_\alpha)}}{(1+\frac{I_{B,max}}{I_{A,max}})\omega C}} \tag{4.25}$$

$$V_\beta = \sqrt{\frac{V_{AN}I_{B,max}\sqrt{\cos(\theta_\beta - \theta_\alpha)}}{(1+\frac{I_{A,max}}{I_{B,max}})\omega C}} \tag{4.26}$$
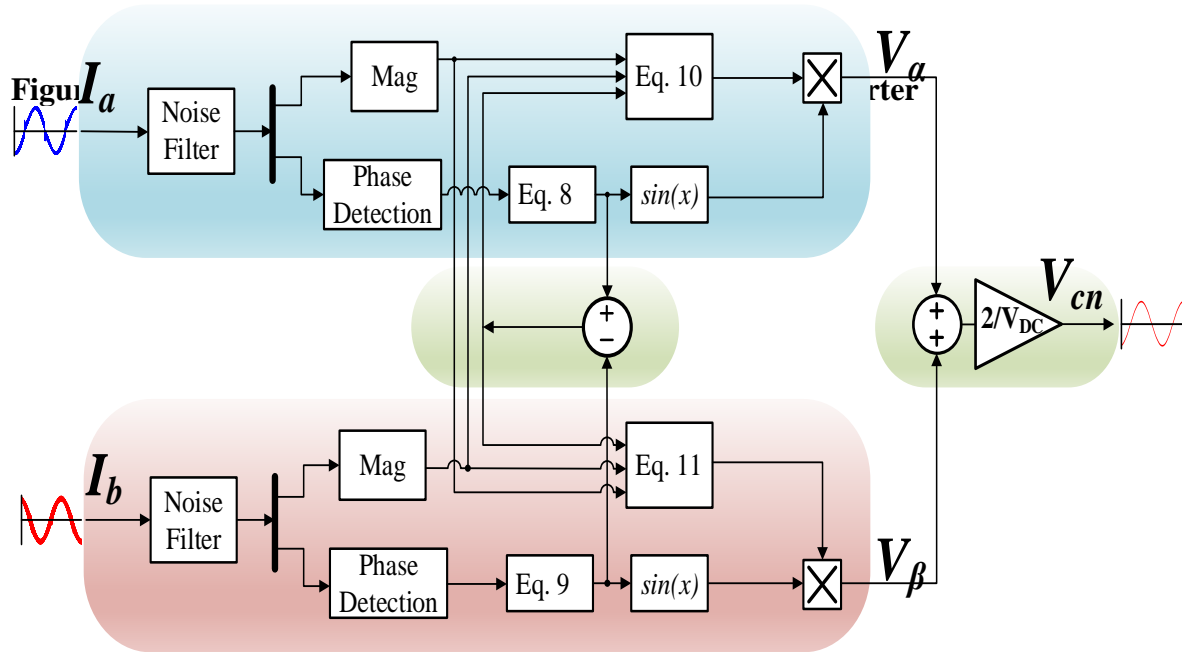
4.3.1 Power Optimizer (PO) Modeling and Control

The proposed PO interfaces the two input sources with a single output via the half bridge and the balancing inductor shown in Figure. 43. By measuring the voltage across the two inputs (V_{PV}, and $V_{Battery}$), the duty ratio for S9 and S10 can be determined using equation 4.27 such that $\delta_{PV} + \delta_{Battery} = 1$. The $L_{Balancing}$ inductor value can be calculated using equation 4.28. I_{bal} is the reference current for different power optimizing states as shown in Table 7. According to equations 4.29,

and 4.30 inductors current (I$_{bal}$) decouples the series connected power inputs. Each state can be achieved with simple PI controller to achieve the required I$_{bal}$ value.

$$\delta_1 = \frac{V_{pv}}{V_{Battery}+V_{pv}} = \frac{V_{pv}}{V_{dc}} \tag{4.27}$$

$$L_{balancing} = \frac{D_{1\alpha} * V_{pv}}{F_{sw} * \Delta I_L} \tag{4.28}$$

$$\boldsymbol{I_{pv}} = \frac{P_{pv}}{V_{pv}}, \ \boldsymbol{I_{battery}} = \frac{P_{battery}}{V_{battery}} , \boldsymbol{I_{bal}} = I_{pv} - I_{battery} \tag{4.29}$$

$$I_o = \delta_{pv} * I_{pv} + \delta_{Battery} * I_{Battery} \tag{4.30}$$

State A

PV ON/ Battery Off
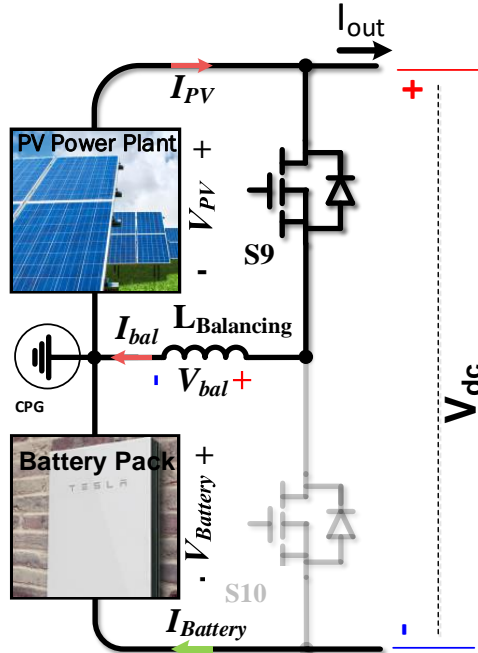
State B
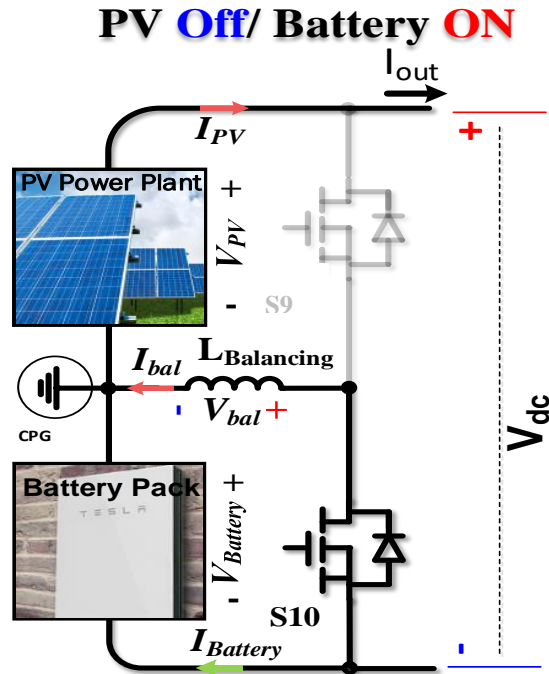
Figure. 43 Switching states of the power optimizer allowing each source to operate independently in respective to their available power level by switching between state (a) and state (b) Optimizing States

Table 8 The current balancing states for the power optimizer circuit shown in Figure. 43.

I_{bal} Current Polarity	PO Operational State
$I_{bal}>0$	$P_{PV}>P_{Battery}$
$I_{bal}>0$	$P_{PV}=P_{Battery}$
$I_{bal}<0$	$P_{PV}<P_{Battery}$

4.4 Design Example

A design example for the proposed system four-leg inverter shown in Figure. 41 at 2kW is introduced with specifications in Table 9. A design procedure is shown to compute various values. All the circuit inductors are assumed to be designed for a 20% current ripple and their selected value is 250 µH using equation 4.31. The capacitors (C_{an}, C_{bn}) are designed to form an output filter such that all high frequency ripples above 5 kHz (f_{sw}/20) are eliminated using equation 4.32. Per the given design constrains the calculated values of C_{an}, C_{bn} are 5 µF was found sufficient to filter the voltage ripples on the output.

The decoupling capacitor (C_{ad}) is designed for the maximum instantaneous power that is needed to match the maximum instantaneous output power using equation 4.33. The full rated load condition without any phase shifts is considered the worst-case scenario when double of the output current has to be processed through the decoupling leg; therefore, the decoupling capacitor (C_{ad}) is designed for this case to be able to handle all other conditions. The calculated value for C_{ad} is 300 µF.

$$L_{min} \geq \frac{V_{DC}}{8\Delta I_L f_{sw}} \tag{4.31}$$

$$C_{min} \geq \frac{1}{\omega^2 L} \tag{4.32}$$

$$C_{ad} = \frac{V_{an,max}(I_{a,max} + I_{b,max})}{\omega V_{cn,max}^2} \tag{4.33}$$

The size of the decoupling capacitor is largely determined by the DC input voltage, which sets the upper limit on the RMS output voltage ($V_{an,max}$). This voltage level also limits the DC voltage utilization in the decoupling leg, similarly to the single-phase topology discussed in [4]. Because of this, the current driven through the neutral leg (I_{cn}) is twice as high as the current driven

in the output phases (I_a, I_b). Based on these assumptions equation 4.33 can be re-written to be a function of the DC input voltage (V_{dc}). Equation 4.34 gives the minimum decoupling capacitor value (C_{ad}) for a given DC input voltage (V_{dc}), given the output current and frequency.

$$C_{ad} = \frac{2(I_{a,max} + I_{b,max})}{\omega V_{DC}}$$

(4.34)

Table 9 Specification and Values for design example for dual phase four leg inverter with active decoupling and integrated power optimizer.

Design Parameters	
Power Rating	2 kW
Switching(f_{sw})/Output Frequency(f_{out})	100 kHz / 60 Hz
DC Bus Voltage	400 V_{DC}
$V_{an,max}$/$V_{bn,max}$/$V_{ab,max}$	120 V_{rms}/120 V_{rms}/240 V_{rms}
Inductor Current Ripple (ΔI_L) (All)	20% of Avg. (1.67 A)
Output LC Filter Cutoff Frequency	f_{sw}/20
C_{link}	50 μF (for 1% input voltage ripple)
Inductors (L_1, L_2, L_3,L_{ad})	250 μH
C_{ad}	300 uF
C_{an},C_{bn}	5uF
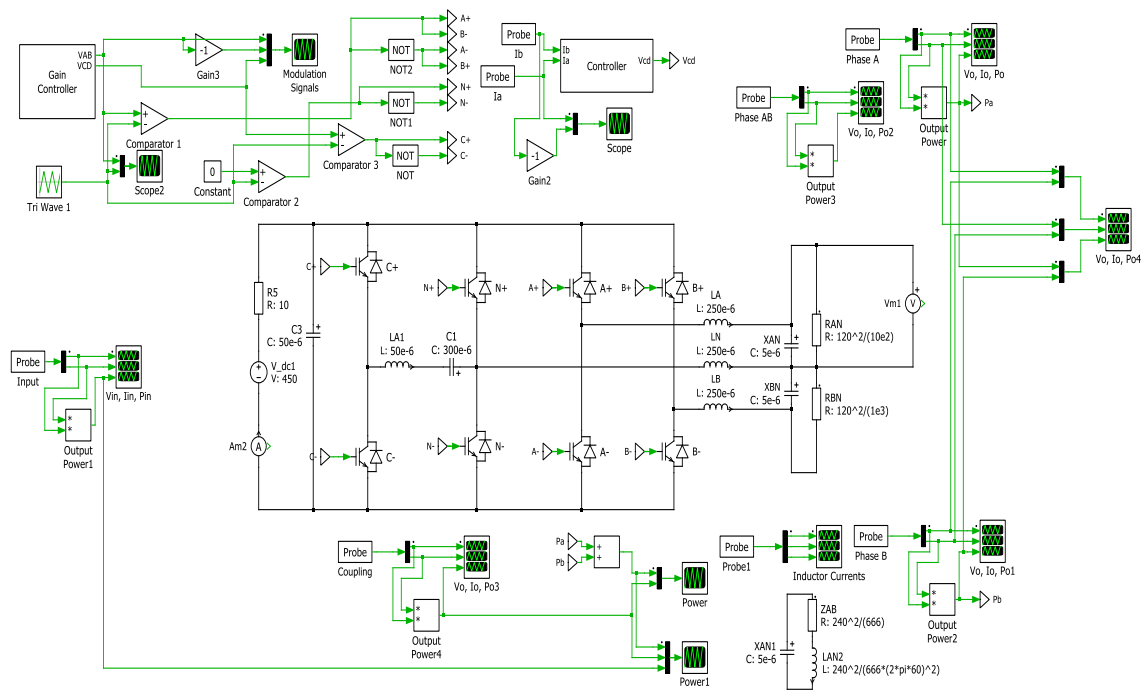
Figure. 44 PLECS Simulation Diagram for the 4-Leg Inverter with Active Decoupling

Figure. 45 PLECS controls simulation diagram for the 4-leg inverter with active decoupling
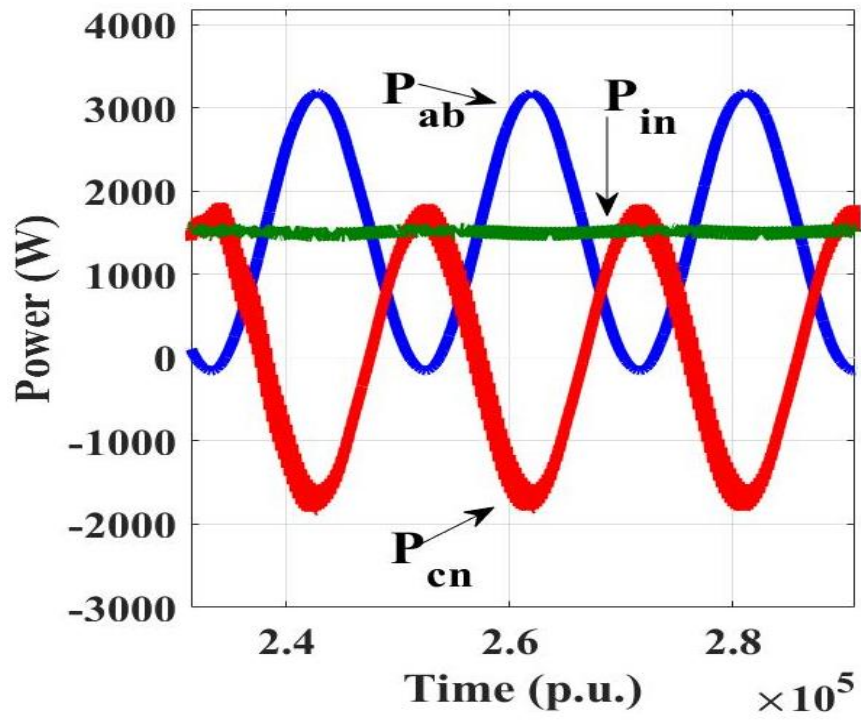
a) Φ=45 lagging
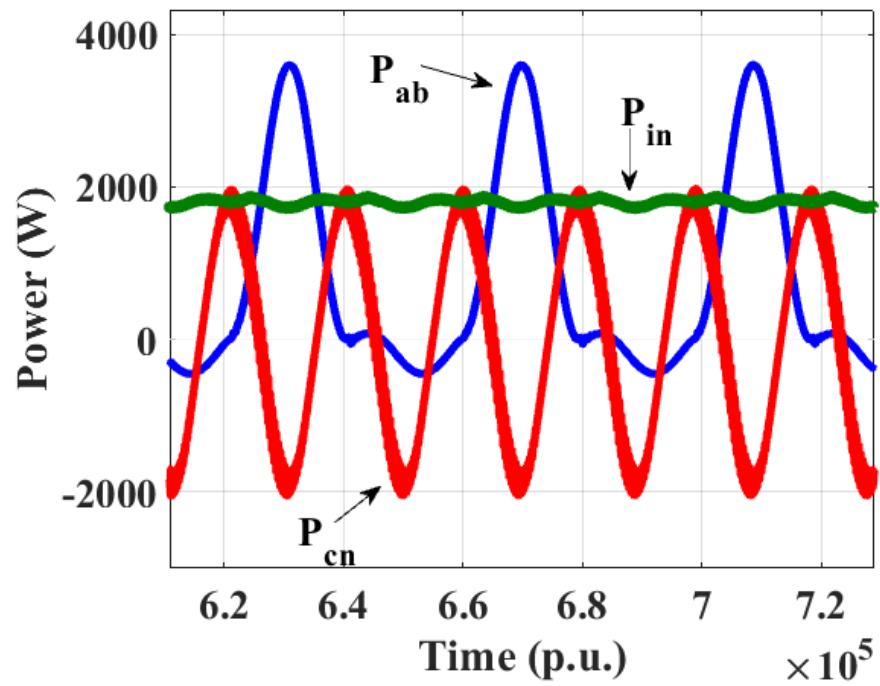
b) Nonlinear
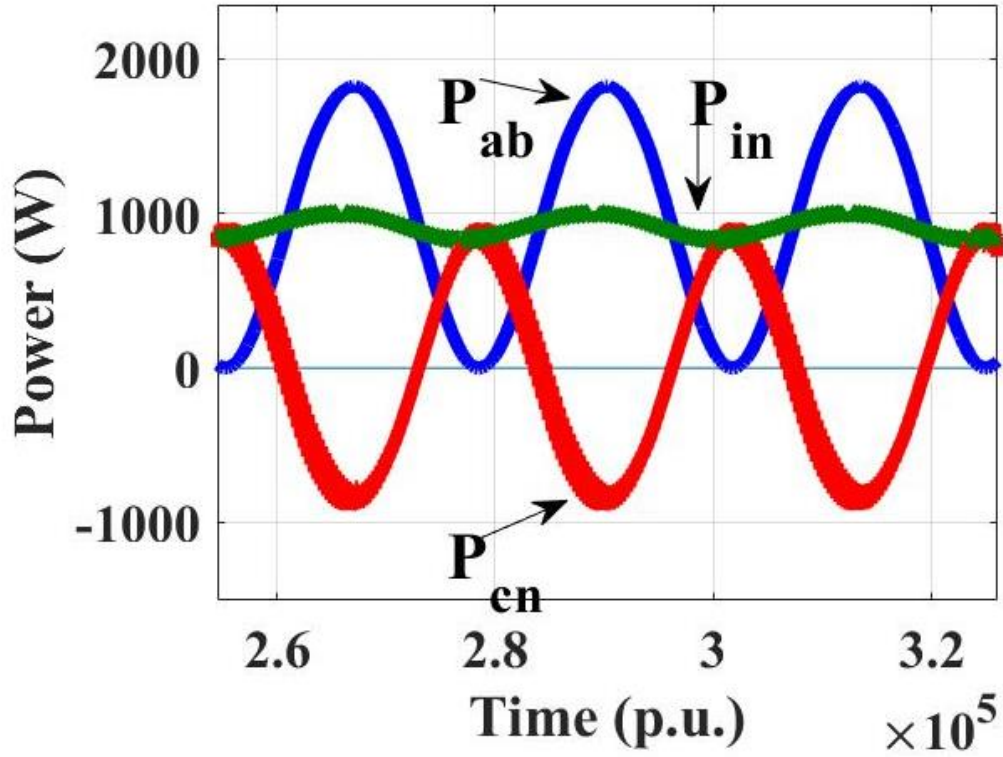
c) One Load Disconnected

Figure. 46 Simulation results of the proposed topology (Figure. 41). (a) Total power output for Phase A and B (P_{ab}), the active decoupling leg power (P_{cn}) and P_{in} is the input dc power. Notice the cancellation of the double line frequency power ripple in Pin. (b) same as (a) for nonlinear load condition; (c) results when Phase A is open circuit.

For extreme load conditions, the proposed approach in Figure. 41 was simulated using PLECS. In the obtained simulation results in Figure.45, P_{ab} represents the summation of the power across Phase a and Phase b. For Figure.45.a, the circuit tested at power factor of 0.7 which is a common industrial practice, and P_{in} shows a pure DC input with no circulating harmonics. Figure.45.b a full diode rectifier was connected to phase a and phase b which is typical home/building load condition, P_{in} shows significantly low 2nd harmonic of <0.1%. Figure.45.c

represents phase a at 100% while phase b at 0% load, the P_{in} has minor 2nd harmonic of <0.5% which is below the accepted IEEE standard 1547, and 2030.

Figure.47 shows the response of the proportional resonant controller of the topology to load stepping of a single output leg from 50% load to 100% load. The key figure for the controller is the overshoot of the response. The overshoot of the current is around 0.1 A, which is less than 2% of the final value. The overshoot in the input voltage is also very low at less than 0.25% of the final value of the step. The distortion in the input current and voltage quickly converge to zero in less than 2 milliseconds. For solar applications, this response time will be insignificant.
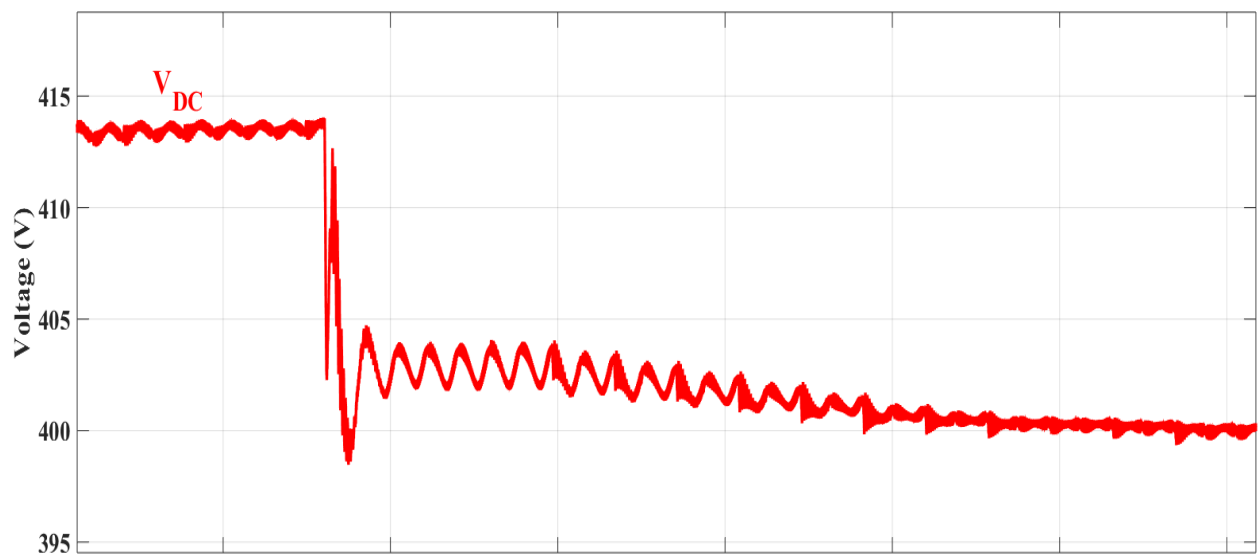
(a)
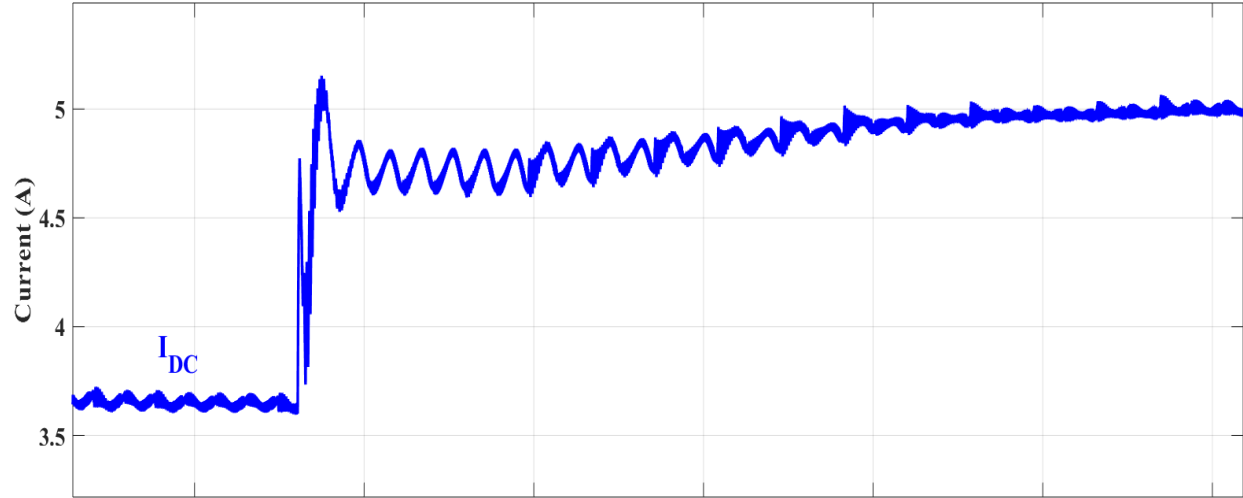
(b)

Figure. 47 Transient response to load stepping at the output from 75% total load to full load. (A) Input Voltage Stepping: Input Voltage steps down from 414 V to 400 V (B) Input Current steps up from 3.6 A to 5.0 A.

For the disucced load stepping, it can be noticed the voltage changes from 414 V to 400 V as input which is very important for the inverter modulation for the designed closed loop controller. The system response was with minimal overshoot and the designed PI controller responose was sufficient to accommodate these changes.

Figure. 48 shows the overall system power responose where the load between Phase A and

Phase B has been stepped and P_{CN} processed the additional generated power ripples due to the double-line frequnecy effect. Consequently, the input DC power P_{IN} has increased with minimally seen effects of the circulated harmonics. There is always a room of improvement for the designed controller in order to minimze the produced current overshoot and make it to smoother respone time.

Output Power vs. Balancing Power and Input Power Transient Response to Load Stepping
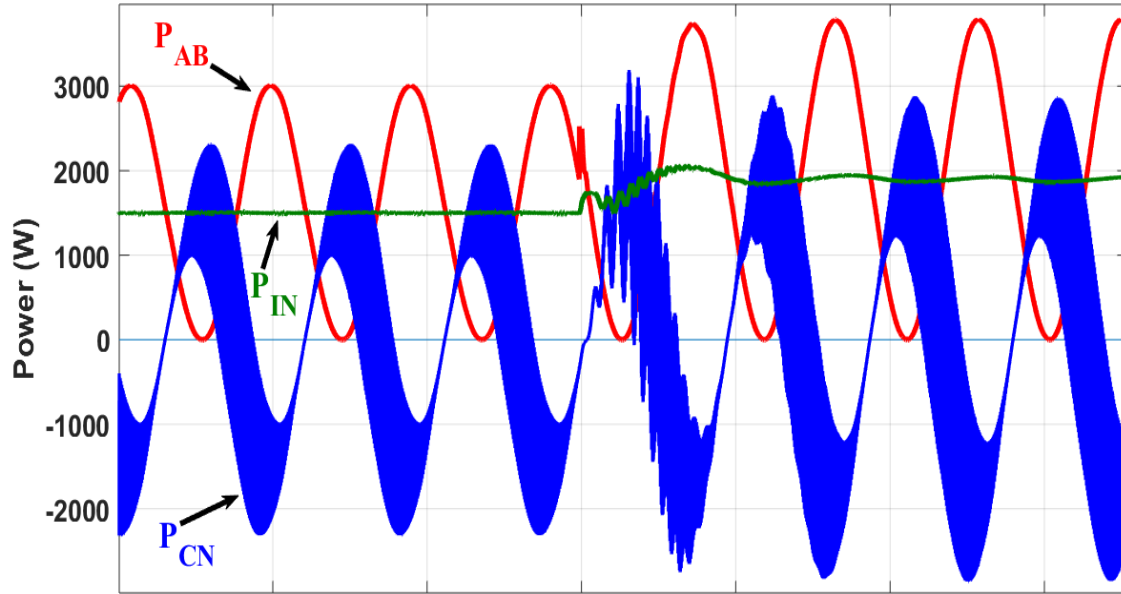
Figure. 48 Output, Input, and Balancing Power Transient Response to Load Stepping of Output Impedance of One Load from 50% load to 100% load.

As it can be seen from

Figure. 49, the generated modulation signals have no over modulation regions when the load stepped up from 75% load condition to 100% full load at rated power. The modulation signals are the references signals needed to generate the proper switching states to achieve the required V_{CN} voltage across the active decoupling leg.
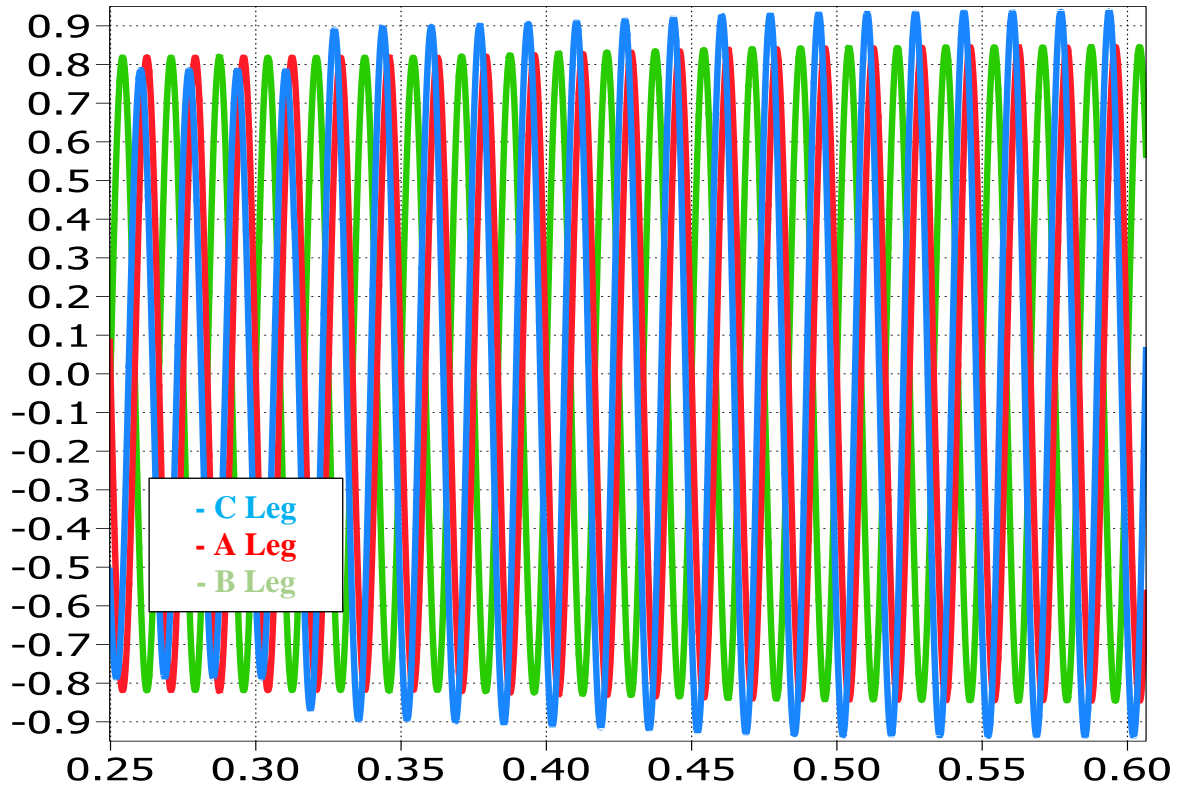
Figure. 49 The generated modulation signals for the designed 4-leg inverter with active decoupling

Figure.50 presents the currents across Phase A, Phase B, and the neutral leg Phase N. I_a is stepping by 50% to achieve a full load condition where both phases A&B are balanced and fully rated. Consequently, the current through the neutral leg on Phase N has lower Peak-to-Peak value due to the fact both phases are balanced.
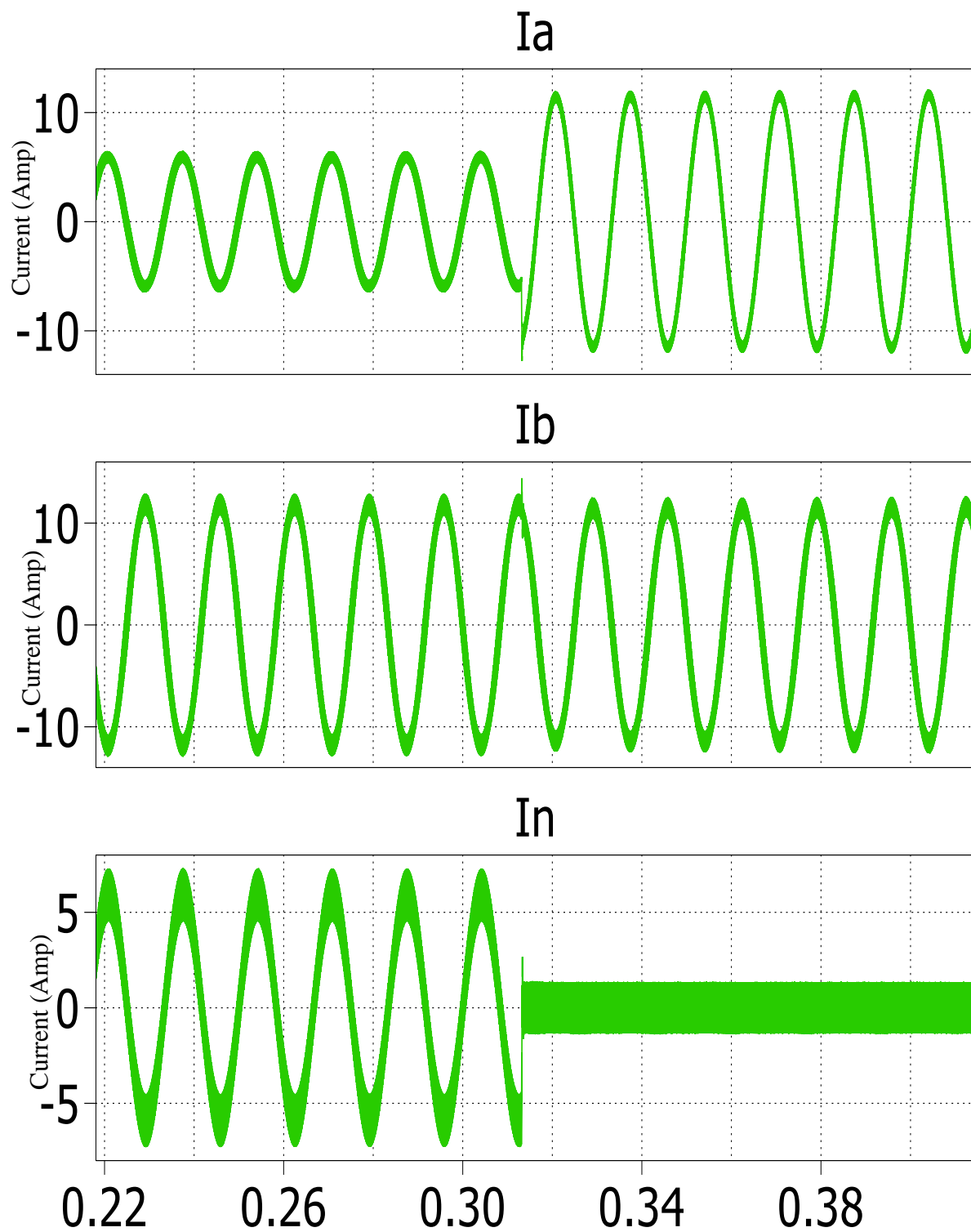
Figure. 50 The inductor currents on Phase A, Phase B, and Phase N when the load stepped from 75% to 100 % full load balanced.

4.5 Experimental Results

A small-scale laboratory prototype for Figure. 41 was developed and was tested for functionality as shown in Figure.51. The designed prototype is set for input voltage DC supply of 218 and the load voltage was set for 60 Vrms with total power rating of 180W. The small-scale laboratory prototype is built using GaN FETs half bridge modules (LMG3410) from Texas Instruments with integrated gate drives. The ratings of passive elements as shown in Figure. 41 as following: DC link capacitor (C_{link}) size is 75 uF, the decupling capacitor (C_{ad}) is 150 uF, and the decupling inductor (L_{ad}) is 100 uH presented all in Figure.51. The topology was tested in an open-loop configuration at worst case scenario when loads are balanced at full rating. The results are presented in Figure.52. and Figure.53.

The input current of the topology had very low distortion, while processing the reactive power generated by the loads through the decoupling leg current as shown in Figure. 52. The voltages produced across each of the phase legs displayed low distortion as shown in Figure.53.

The relationship between the current and voltage across the decoupling capacitor was confirmed to be about 90 degrees, which confirmed the simplifying assumption made earlier. The current and voltage in the decoupling leg ($V_{cn}, I_c = I_{cn}$), shown in Figure.53, accounts for the total reactive power in the circuit. The amplitude of the capacitor voltage also approaches the magnitude of the phase voltages, which is the maximum voltage level in the decoupling leg. Due to this, the decoupling current is almost twice the value of the output currents across each load.
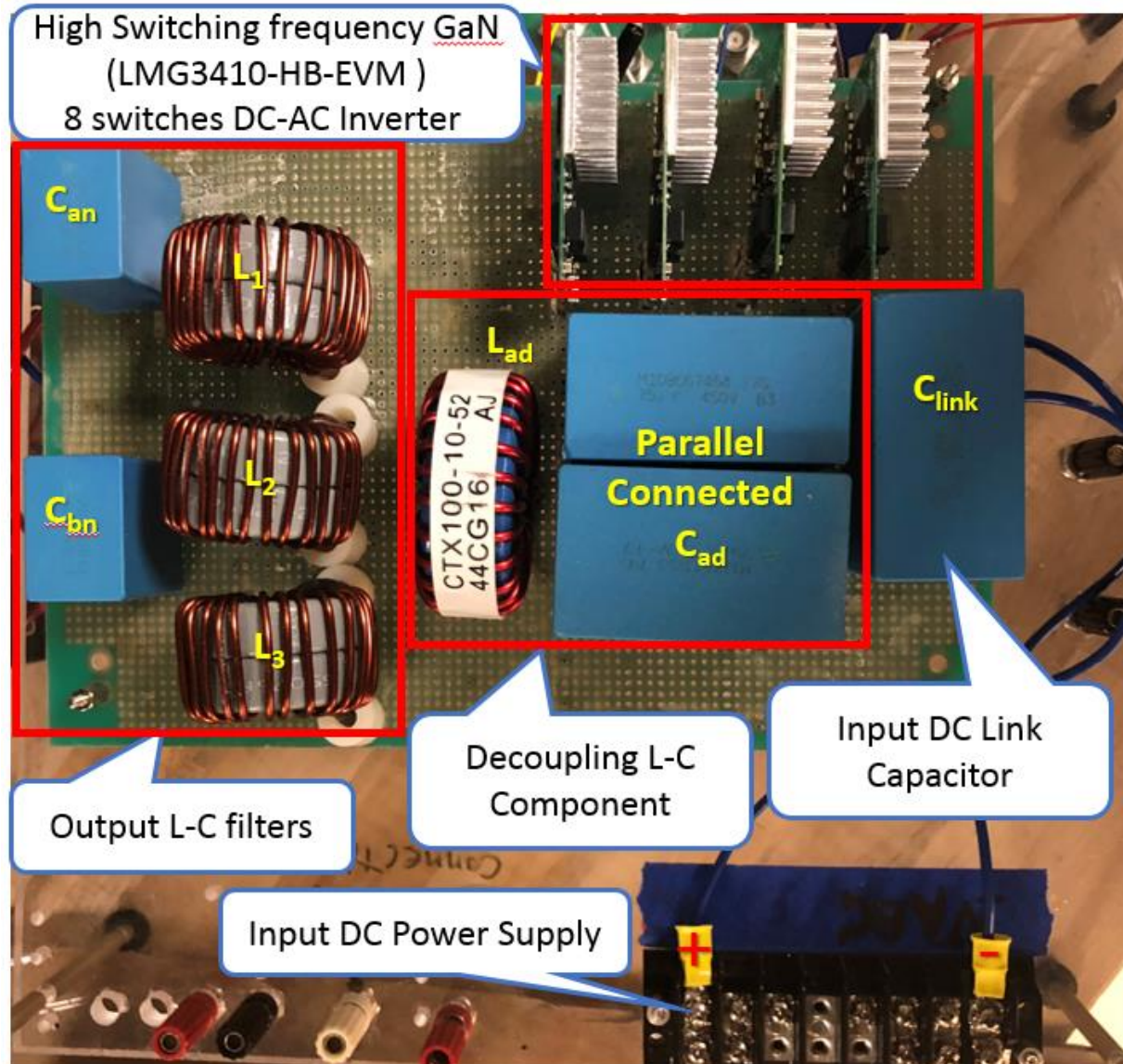
Figure. 51 Four Leg Inverter Board hardware setup based on Texas Instrument LMG3410-HB-EVM half bridgeboard
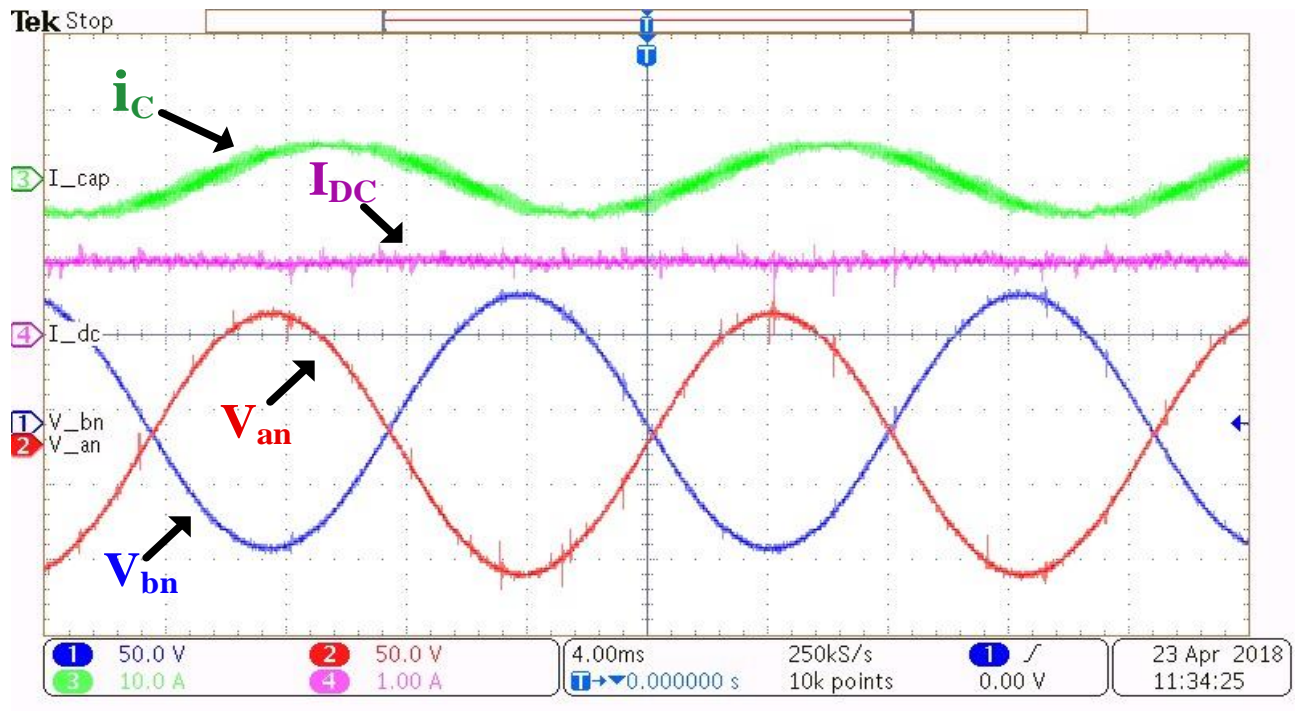
Figure. 52 Open loop testing for balanced load condition. Input current is shown to have less than 5% distortion and decoupling capacitor current is processing the reactive power from the load. The output voltages are at 60 V$_{RMS}$ with low distortion.
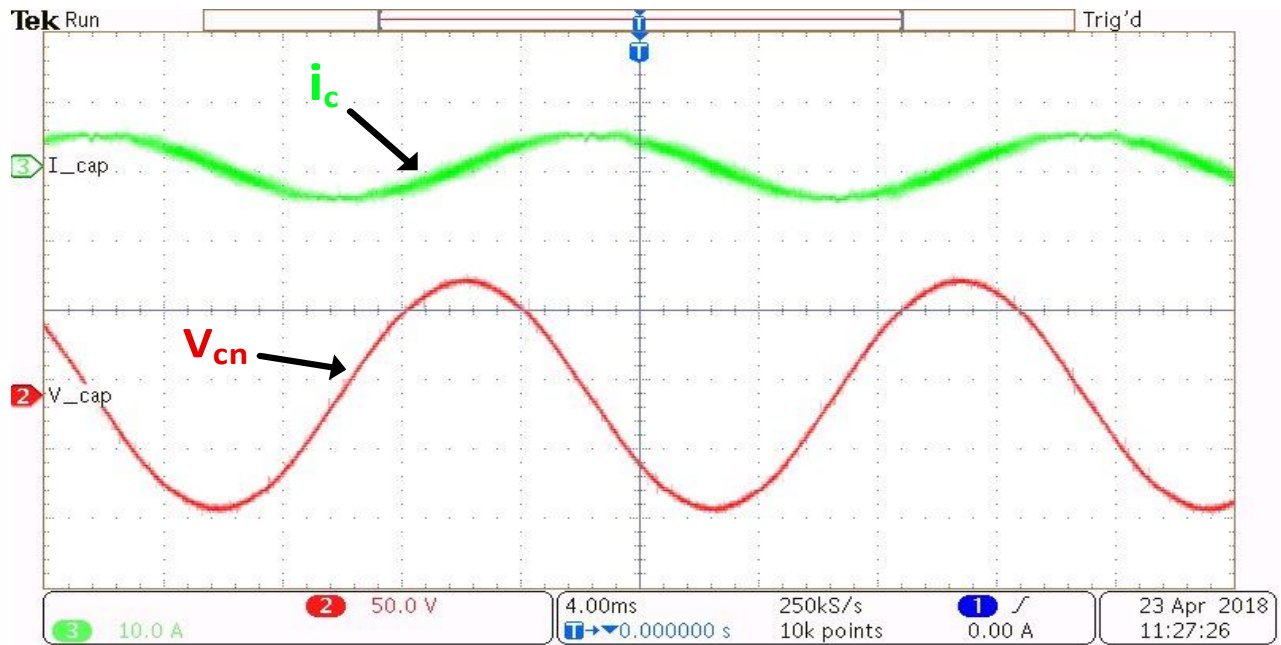
Figure. 53 Open-loop testing for balanced load condition. The decoupling capacitor current and voltage are displayed at 90 degrees phase shift. The decoupling capacitor voltage is almost the same level as the output phase voltages to process the reactive power of the loads.

4.6 Conclusion

A dual phase output inverter with active decoupling and integrated power optimizer has been presented along with its control strategy. One limitation of the topology is the DC voltage utilization in the decoupling leg. The simulation results show that the system has eliminated the double line frequency for different load conditions. More importantly, the system dynamics ease further the interface with the output loads and help to optimize source power utilization with the inverter operation. A design example of 2 kW was presented along with proper element sizing. The scaled down laboratory setup proved the effectiveness of the proposed decoupling method.

V.   CONCLUSIONS AND FUTURE WORK

The dissertation discussed several approaches to enable further the growth of solar energy using PV systems. The main application of this work is large-scale PV systems and off-grid circuit designs. The work emphasis is on processing fractional power from the total power plant by introducing new design architectures.

The first design architecture rethinks large-scale PV plants string designs where several PV modules connected in series. The new proposed voltage balancing architecture balances the voltage between the strings by processing fractional power through the passive elements. The proposed approached compared to other fully rated architectures. The approach liberates the converter from centralized control by enabling power management on the string level. Thus, the approach enables higher energy yields, less losses, faster tracking, and higher reliability. Moreover, the approach is proven to be scalable for unlimited number of strings. This approach introduces a completely new solution for handling power for large-scale PV plant. Simulation dn experimental results for the voltage balancing approach has been conducted to validate the approach.

Furthermore, the voltage balancing approach has been merged with current balancing approach to effectively handle different environmental conditions in a large-scale PV power plant. The new two stage fraction rated approached introduces a new dynamic way of managing future PV power plants. The architecture always enables harvesting maximum power while it communicates with the inverter to tune for maximum power availability to the grid. The first stage is the current balancing where a fractional power is processed through the passive elements to harvest maximum power. Further, the second stage is the voltage balancing where the voltage of

the strings is balancing so that no power is lost during the operation. Simulation and experiment results has been conducted to verify the concept.

Both approaches have shown that PV system has a higher reliability when distributed power electronic management architectures is introduced. The system can locate the maximum power point faster than traditional approaches because it relies on environmental information from the internet to generate reference voltages and currents to guide the current balancing, and voltage balancing stages. No string power is lost due to the voltage difference between these strings as well as no current limitation on the series connected modules.

Finally, the dual phase-output 4-leg inverter integrated with a power optimizer explored a new way of feeding off-grid applications. The inverter actively decoupled the power ripples generated from the double line frequency in the system by introducing a half bridge that processes the ripple through passive elements. The closed loop control mechanism has shown its effectiveness to compensate for different load conditions (non-linear, linear, balanced, and non-balanced) with ability to feed two phases at once. As well as the current balancing stage with multiple functionalities has been introduced and verified in simulation and experiment results.

As future work, the fractional rated converters open new research opportunities for different types of applications for different power ratings. It would be interesting to explore introducing a hybrid approach of integrating different types of renewable inputs to the topology since it processes only a fraction of the power to achieve the same objective of a fully rated converters.

Since these systems are part of distributed power electronics energy management tools. They already position themselves uniquely in the PV market, it would be interesting to integrate machine learning to the system to offer a new approach in driving PV power plants.

REFERENCES

[1]   R. Fu, D. Feldman, R. Margolis, M. Woodhouse and K. Ardani, "U.S. Solar Photovoltaic System Cost Benchmark: Q1 2017," NREL, Golden, 2017.

[2]   I. Fraunhofer Institute for Solar Energy Systems, "PHOTOVOLTAICS REPORT," Frauhofer ISE, 2018.

[3]   P. Mazumdar, P. N. Enjeti and R. S. Balog, "Analysis and design of smart PV modules," *2013 Twenty-Eighth Annual IEEE Applied Power Electronics Conference and Exposition (APEC)*, Long Beach, CA, 2013, pp. 84-91.

[4]   M. Kasper, D. Bortis and J. W. Kolar, "Classification and Comparative Evaluation of PV Panel-Integrated DC–DC Converter Concepts," *IEEE Transactions on Power Electronics* , vol. 29, no. 5, pp. 2511-2526, 2014.

[5]   S. M. a. A. A.-D. Rahila Abdul-Kalaam, "Review of Maximum Power Point Tracking Techniques for Photovoltaic System," *Global Journal of Control Engineering and Technology,* vol. 2, pp. 8-18, 2016.

[6]   A. K. Abdelsalam , A. M. Massoud, S. Ahmed and P. N. Enjeti, "High-Performance Adaptive Perturb and Observe MPPT Technique for Photovoltaic-Based Microgrids," *IEEE Transactions on Power Electronics* , vol. 26, no. 4, pp. 1010 - 1021, 2011.

[7]   C. Yang and K. Smedley , "A cost-effective single-stage inverter with maximum power point tracking," *Power Electronics IEEE Transaction,* vol. 19, no. 5, pp. 1289-1294, 2004.

[8]   N. Fenua, D. Granozio, G. Petrone, G. Spagnuolo and M. Vitelli, "Optimized one-cycle control in photovoltaic grid connected applications," *IEEE Transactions on Aerospace and Electronic Systems,* vol. 42, no. 3, pp. 954-972, 2006.

[9] M. Fortunato, . A. Giustiniani, G. Petrone, . G. Spagnuolo and M. Vitelli, "Maximum Power Point Tracking in a One-Cycle-Controlled Single-Stage Photovoltaic Inverter," *IEEE TRANSACTIONS ON INDUSTRIAL ELECTRONICS,* vol. 55, no. 7, pp. 2684-2693, 2008.

[10] H. AK, I. Muta, T. Hoshino and M. Osakada, "Maximum PhotoVoltaic Power Tracking: an algroithim for rapidly changing atmospheric conditions," *IEEE Proceedings on Generation, Transmission and Distribution,* vol. 142, pp. 59-64, 1995.

[11] T. J. Flack and B. N. Pushpakaran, "GaN technology for power electronic applications: a review," *Journal of Electronic Materials ,* vol. 45, pp. 2673-2682, 2016.

[12] R. S. Pengelly, S. M. Wood, J. W. Milligan, S. T. Sheppard and W. L. Pribble, "A review of GaNon SiC high electron-mobility power transistors and MMICs," *IEEE Transactions on Microwave Theory and Techniques,* vol. 60, pp. 1764-1783, 2012.

[13] S. Bush, "GaN-on-Si power transistors from French lab Leti," ElectronicsWeekly.com, Surrey, 2015.

[14] T. Ueda, "Reliability issues in GaN and SiC power devices," *2014 IEEE International Reliability Physics Symposium*, Waikoloa, HI, 2014, pp. 3D.4.1-3D.4.6.

[15] J. T. Hawke, H. S. Krishnamoorthy and P. N. Enjeti, "A Family of New Multiport Power-Sharing Converter Topologies for Large Grid-Connected Fuel Cells," *IEEE Journal of Emerging and Selected Topics in Power Electronics,* vol. 2, no. 4, pp. 962-971, Dec 2014.

[16] J. Hawke, H. Krishnamoorthy and P. Enjeti, "A multiport power sharing converter topology for renewable-to-grid interface," in *IEEE Energy Conversion Congress and Exposition (ECCE)*, Pittsburgh, PA, 2014.

[17] M. H. T. K. a. H. W. T. Shimizu, "Generation control circuit for Photovoltaic Modules,"
IEEE Transaction in Power Electronics , vol. 16, no. 3, pp. 293-300, 2001.

[18] K. M. Paasch, M. Nymand and S. . B. Kjaer, "Long term energy yield measurements of a
string- vs. central inverter concept tested on a large scale PV-plant," in *EPE'15 ECCE-
Europe*, Geneva, Switzerland, 2015.

[19] M. S. Agamy, . M. Harfman-Todorovic, A. Elasser, S. Chi, R. L. Steigerwald, J. A.
Sabate, A. J. McCann, L. Zhang and F. . J. Mueller, "An Efficient Partial Power
Processing DC/DC Converter for Distributed PV Architectures," *IEEE Transactions on
Power Electronics,* vol. 29, no. 2, pp. 674-686, Feb 2014.

[20] A. E. I. Inc., "Choosing 600 Vs 1000 VDC in PV Projects," Fort Collins, Colarado , 2014.

[21] S. Moskowitz, "The The Next Opportunity for Utility PV Cost Reductions: 1,500 Volts
DC," GTM a wood Machenzie Bussines , 14 May 2015. [Online]. Available:
https://www.greentechmedia.com/articles/read/the-next-opportunity-for-utility-pv-cost-
reductions-1500-volts-dc#gs.z2V1FuU. [Accessed 5 1 2018].

[22] E. Serban, M. Ordonez and C. Pondiche, "DC-Bus Voltage Range Extension in 1500 V
Photovoltaic Inverters," *IEEE Journal of Emerging and Selected Topics in Power
Electronics,* vol. 3, no. 4, pp. 901-917, 2015.

[23] E. . V. Paraskevadaki and S. . A. Papathanassiou, "Evaluation of MPP Voltage and Power
of mc-Si PV Modules in Partial Shading Conditions," *IEEE Transactions on Energy
Conversion,* vol. 26, no. 3, pp. 923-932, April 2011.

[24] R. Ramaprabha and B. L. Mathur, "A Comprehensive Review and Analysis of Solar Photovoltaic Array Configurations under Partial Shaded Conditions," *International Journal of Photoenergy,* vol. 2012, p. 16, 2012.

[25] H. Patel and V. Agarwal, "MATLAB-based modeling to study the effects of partial shading on PV array characteristics," *IEEE TRANSACTIONS ON ENERGY CONVERSION,* vol. 23, no. 1, pp. 302-310, 2008.

[26] S. B. Balathandayuthapani, C. S. Edrington and S. D. Henry, "Analysis and Control of a Photovoltaic System: Application to a High-Penetration Case Study," *IEEE Systems Journal,* vol. 6, no. 2, pp. 213-219, June 2012.

[27] P. S. Shenoy, K. A. Kim, B. B. Johnson and P. T. Krein, "Differential Power Processing for Increased Energy Production and Reliability of Photovoltaic Systems," in IEEE Transactions on Power Electronics, vol. 28, no. 6, pp. 2968-2979, June 2013

[28] A. Bidram, A. Davoudi and R. S. Balog , "Control and Circuit Techniques to Mitigate Partial Shading Effects in Photovoltaic Arrays," *IEEE Journal of Photovoltaics ,* vol. 2, no. 4, pp. 532-546, Oct 2012.

[29] A. Morrison, J. W. Zapata, S. Kouro, M. A. Perez, T. A. Meynard and H. Renaudineau, "Partial power DC-DC converter for photovoltaic two-stage string inverters," *2016 IEEE Energy Conversion Congress and Exposition (ECCE)*, Milwaukee, WI, 2016, pp. 1-6.

[30] D. S. Inverters, D. Borup, H. Grau and B. Lave, "STRING INVERTERS FOR PV POWER PLANTS," in *European PV Solar Energy Conference and Exhibition* , Hamburg, 2009.

[31] W. Xiao, "Classification of Photovoltaic Power Systems," in *Photovoltaic power system : modeling, design, and control*, Sydney , Wiley , 2017, pp. 25-46.

[32] IFC, Ed., "Utility-Scale Solar Photovoltaic Power Plants In partnership with A Project Developer's Guide," World Bank Group.

[33] D. Picault, B. Raison and S. Bacha, "Guidelines for evaluating grid connected PV system topologies," 2009 IEEE International Conference on Industrial Technology, Gippsland, VIC, 2009, pp. 1-5.

[34] D. Ahmadi, S. A. Mansouri and J. Wang, "Circuit topology study for distributed MPPT in very large scale PV power plants," 2011 Twenty-Sixth Annual IEEE Applied Power Electronics Conference and Exposition (APEC), Fort Worth, TX, 2011, pp. 786-791.

[35] J. R. R. Zientarski, J. R. Pinheiro, M. L. d. S. Martins and H. L. Hey, "Understanding the partial power processing concept: A case-study of buck-boost dc/dc series regulator," *2015 IEEE 13th Brazilian Power Electronics Conference and 1st Southern Power Electronics Conference (COBEP/SPEC)*, Fortaleza, 2015, pp. 1-6.

[36] J. Leonard, T. Salem, R. Hadidi, B. Gislason, J. C. Fox and M. H. McKinney, "Design and commissioning of 2.5 MW DC supply for evaluating megawatt scale smart solar inverters," *2016 IEEE Industry Applications Society Annual Meeting*, Portland, OR, 2016, pp. 1-5.

[37] ABB, "ABB inverter station PVS800-IS – 1.75 to 2 MW," *ABB inverter station PVS800-IS – 1.75 to 2 MW*. 2017.

[38] R. Inzunza, R. Okuyama, T. Tanaka, and M. Kinoshita, "Development of a 1500Vdc photovoltaic inverter for utility-scale PV power plants," *2015 IEEE 2nd International Future Energy Electronics Conference (IFEEC), 2015.*

[39] A. Mohamed, M. Elshaer and O. Mohammed, "Bi-directional AC-DC/DC-AC converter for power sharing of hybrid AC/DC systems," *2011 IEEE Power and Energy Society General Meeting*, Detroit, MI, USA, 2011, pp. 1-8.

[40] K. Hashmi, M. M. Khan, S. Habib, and H. Tang, "An Improved Control Scheme for Power Sharing between Distributed Power Converters in Islanded AC Microgrids," *2017 International Conference on Frontiers of Information Technology (FIT), 2017.*

[41] A. S. Morsy, Sinan A. Sabeeh Al-Obaidi and P. Enjeti, "A new approach for increasing energy harvest in large scale PV plants employing a novel voltage balancing topology," *2017 IEEE Energy Conversion Congress and Exposition (ECCE), Cincinnati, OH, 2017, pp. 4055-4060.*

[42] K. M. Paasch, M. Nymand and S. . B. Kjær, "Long term energy yield measurements of a string- vs. central inverter concept tested on a large scale PV-plant," *in EPE'15 ECCE-Europe, Geneva, Switzerland, 2015.*

[43] H. Choi, M. Ciobotaru, M. Jang and V. G. Agelidis, "Performance of Medium-Voltage DC-Bus PV System Architecture Utilizing High-Gain DC–DC Converter," *in IEEE Transactions on Sustainable Energy, vol. 6, no. 2, pp. 464-473, April 2015.*

[44] Advances in Utility-SCal PV Plants: Key Lessons Learned. 2017. First Solar [Online]. Available: http://sites.ieee.org/scv-photovoltaic/files/slides/20171101-Advances-in-Utility-Scale-PV-Plants-Key-Lessons-Learned.pdf

[45] F. Blaabjerg, Y. Yang, D. Yang and X. Wang, "Distributed Power-Generation Systems and Protection," *in Proceedings of the IEEE, vol. 105, no. 7, pp. 1311-1331, July 2017*

[46] D. Mitchell and S. Mitchell, "Sunpower SPR-305-WHT-U (305W) Solar Panel," Trina Solar TSM-230 PA05.05 (230W) SolarPanel.[Online].Available:http://www.solardesigntool.com/components/module-panel-solar/Sunpower/514/SPR-305-WHT-U/specification-data-sheet.html. [Accessed: 08-Jul-2018].

[47] "PV Modules," SolarHub - PV Module Details: TSM72-156M 305W - by Shanghai Topsolar Green Energy. [Online]. Available:http://solarhub.com/product-catalog/pv-modules/35783-TSM72-156M-305W-Shanghai-Topsolar-Green-Energy. [Accessed: 08-Jul-2018].

[48] S. E. I. Association, "Solar Industry Data" [Online]. Available: https://www.seia.org/solar-industry-data

[49] International Energy Agency (IEA). World Energy Outlook. Electricity Access Database. 2015.Available:http://www.worldenergyoutlook.org/resources/energydevelopment/energy accessdatabase/

[50] Sarah Feron, Raul R. Cordero, and Fernando Labbe, "Rural Electrification Efforts Based on Off-Grid Photovoltaic Systems in the Andean Region: Comparative Assessment of Their Sustainability," *Sustainability, vol. 9, no. 10, p. 1825, Nov. 2017.*

[51] Anil Tuladhar, "Power management of an off-grid PV inverter system with generators and battery banks," *IEEE Power and Energy Society General Meeting, 2011.*

[52] Ahmed. S. Morsy and P. N. Enjeti, "Comparison of Active Power Decoupling Methods for High-Power-Density- Single Phase Inverters Using Wide-Bandgap FETs for Google Little Box Challenge," *IEEE Journal of Emerging and Selected Topics in Power Electronics , vol. 4, no. 3, pp. 790-798, 2016.*

[53] Z. HAIYU , L. Xiao, B. Ge and R. S. Balog, "Capacitance, dc Voltage Utilizaton, and Current Stress: Comparison of Double-Line Frequency Ripple Power Decoupling for Single-Phase Systems " *IEEE Industrial Electronics Magazine , pp. 37-49, 2017.*

[54] S. A. Sabeeh Al-Obaidi, K. C. Hodge and P. Enjeti, "A Dual-Phase Output 4-Leg Inverter with Active Decoupling and Integrated Power Optimizer for Off-Grid Applications," *2018 9th IEEE International Symposium on Power Electronics for Distributed Generation Systems (PEDG)*, Charlotte, NC, 2018, pp. 1-6.

[55] Sinan Al-Obaidi, and Prasad Enjeti. "IEEE ENERGY CONVERSION CONGRESS & EXPO (ECCE)." IEEE, New Two Stage Differential Mode Power Converter for Large Scale PV Plants, 2018, pp. 1250–1256.

APPENDIX

This section presents SunPower PV module SPR-305WHT-U and Shanghai Topsolar Green Energy PV module TSM72-156M I-V and P-V curves. Further information can be found in references [46, 47].

Array type: SunPower SPR-305-WHT-U; 24 series modules; 40 parallel strings

(a)

(b)
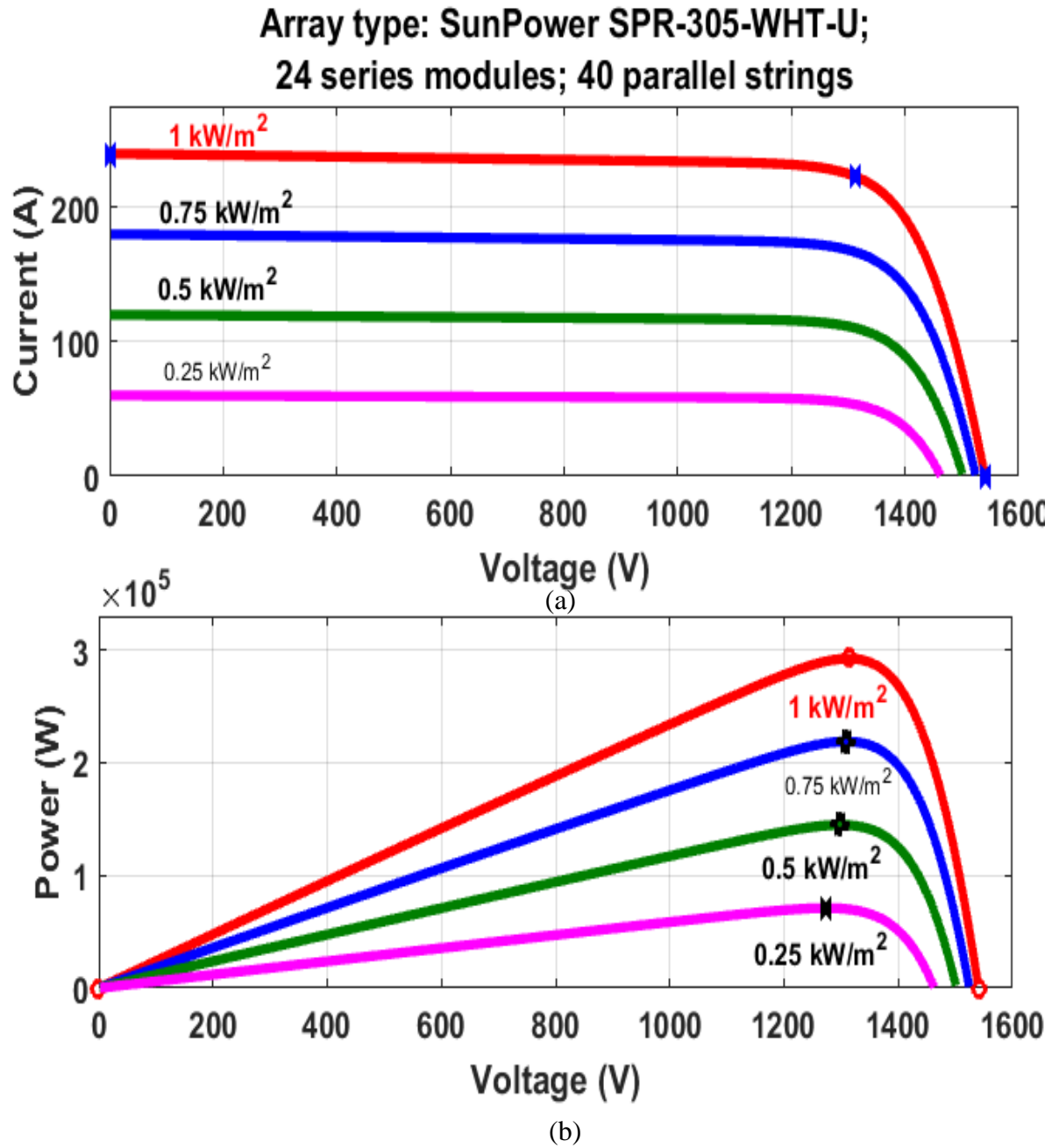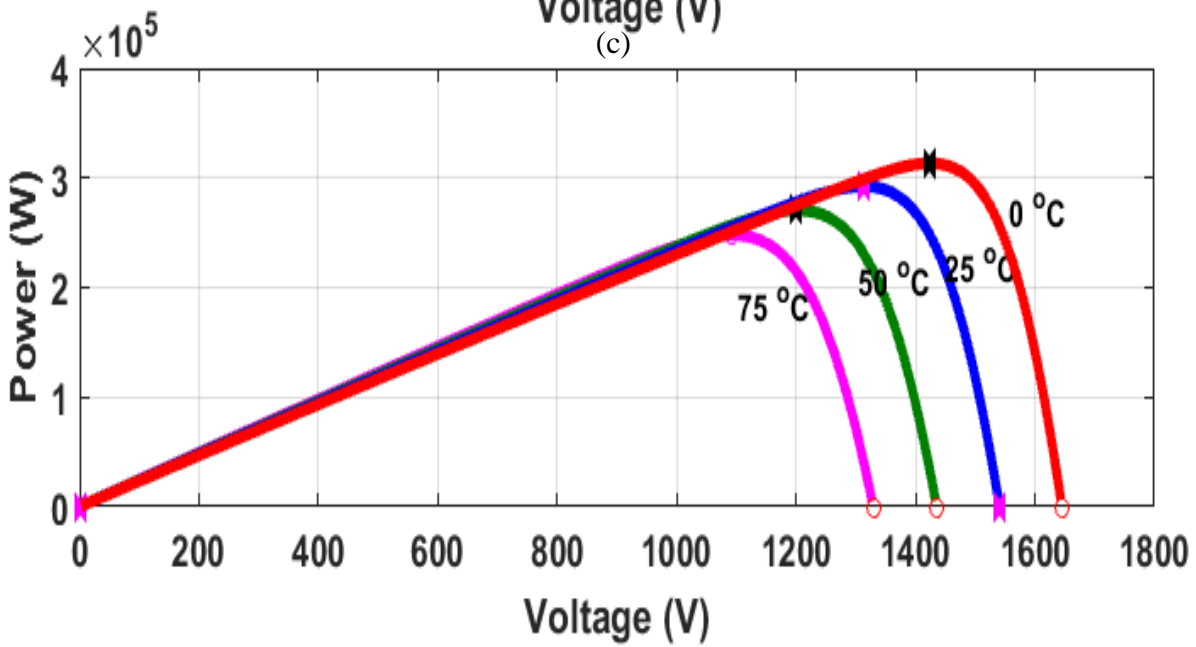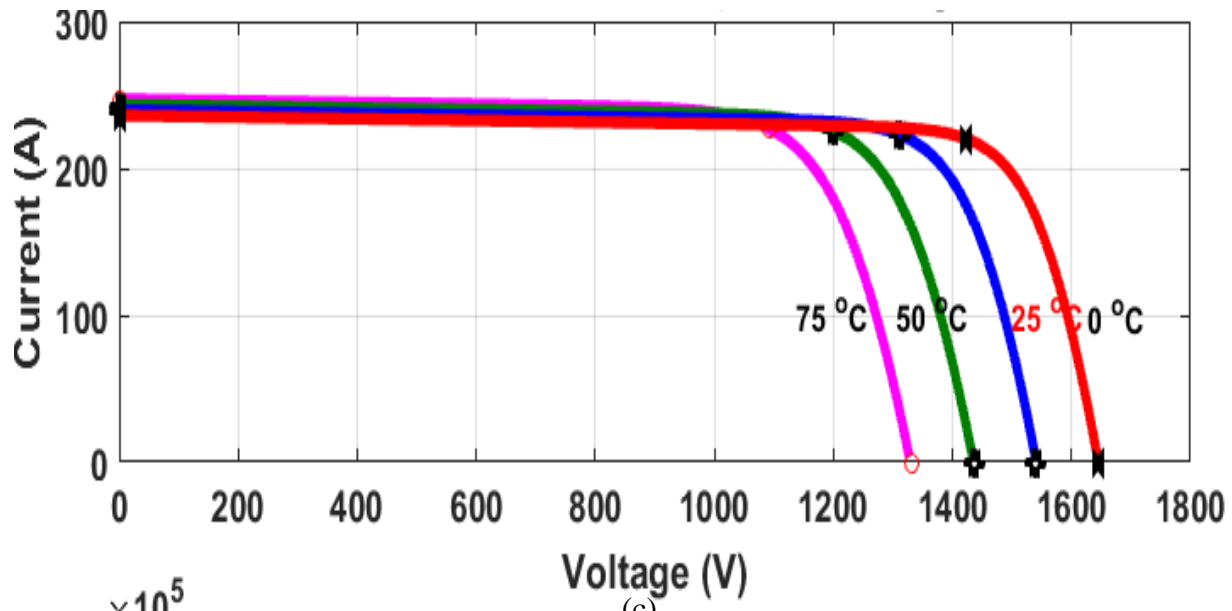
Figure. 54 Sun-Power SPR-305WHT Groups 1,2,3,4 Modules Characteristics with configurations of 24 series/ 40 Parallel: (a) I-V curve and (b) P-V curve under different shading conditions. (c) I-V curve and (d) P-V curve for different temperatures.

Array type: Shanghai Topsolar Green Energy TSM72-156M 305W; 34 series modules; 27 parallel strings

(a)

(b)

(c)

103
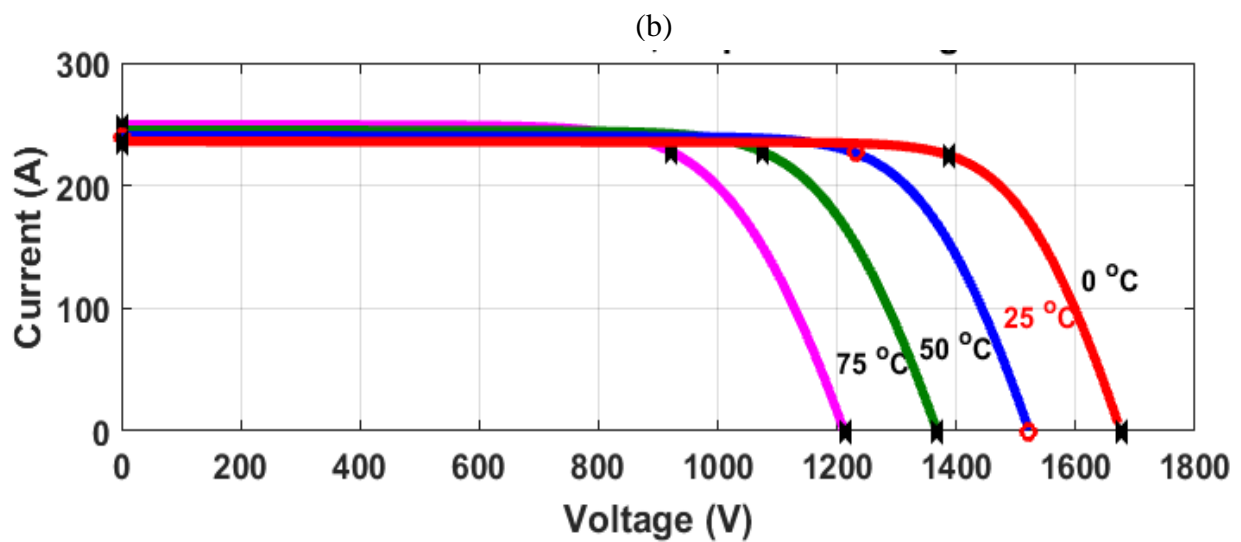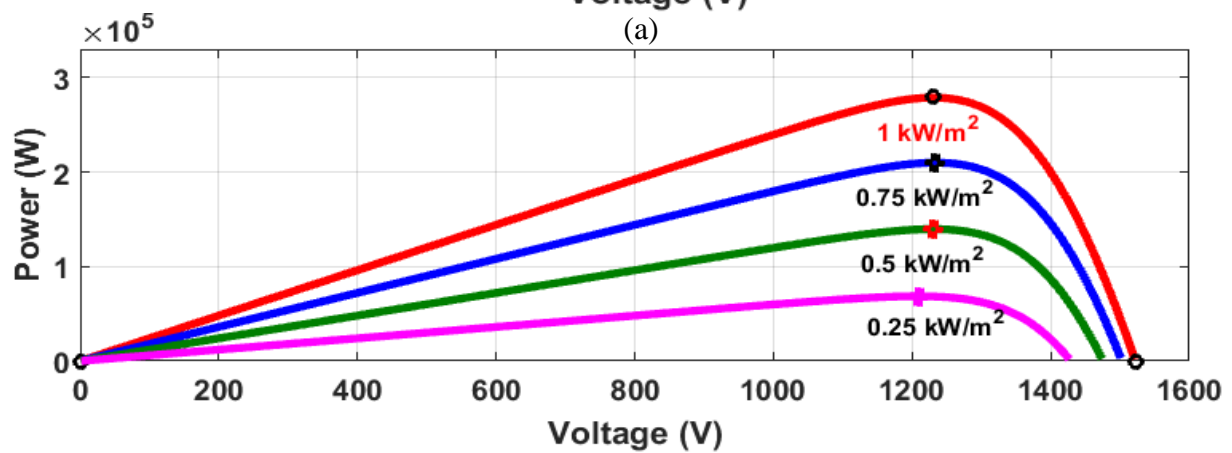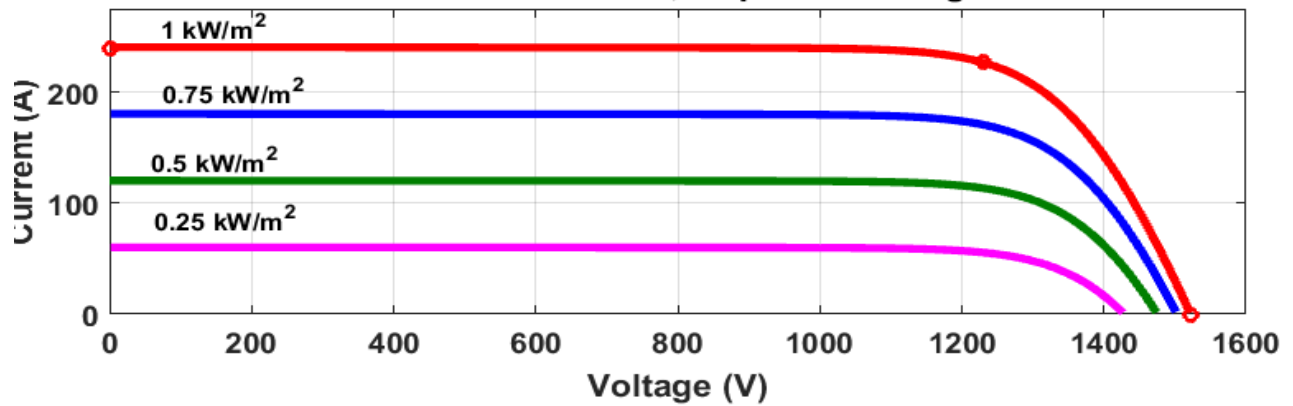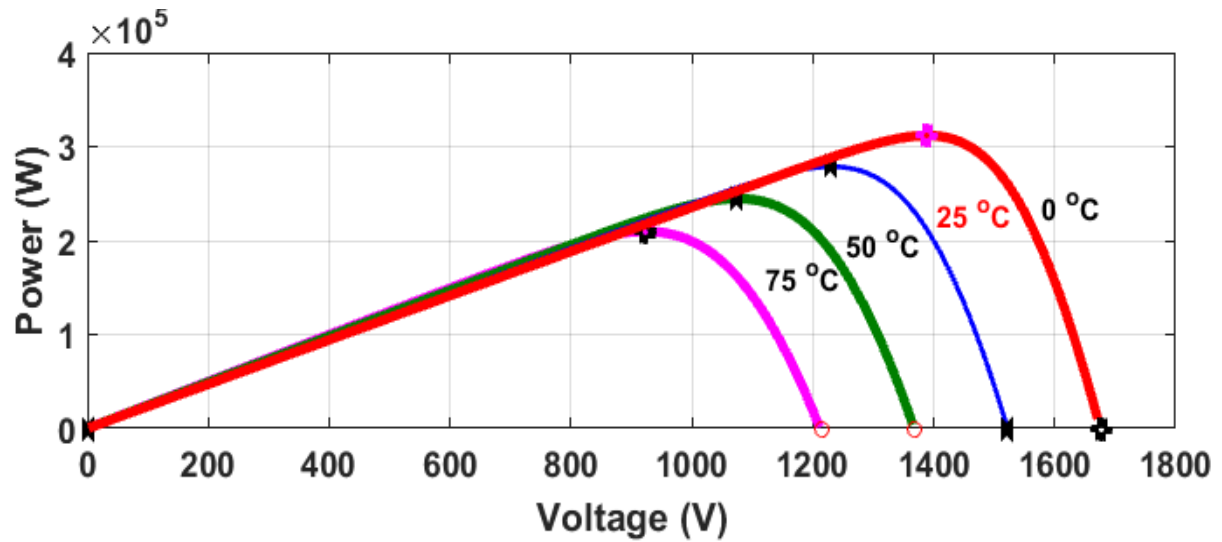
(d)

Figure. 55 Shanghai Topsolar Green Energy TSM72-156M 305W Groups 3 & 4 Modules Characteristics with configurations of 16 series/ 27 Parallel: (a) I-V curve and (b) P-V curve under different shading conditions. (c) I-V curve and (d) P-V curve for different temperatures.

The following data sheets are used for building the voltage balancing approach in section-I and the two-stage differential mode converter in section II.

Littelfuse | Power Semiconductors

SiC MOSFET

LSIC1MO120E0080, 1200 V, 80 mOhm, TO-247-3L

LSIC1MO120E0080 1200 V N-channel, Enhancement-mode SiC MOSFET **HF** RoHS

Product Summary

Characteristics	Value	Unit
V_{DS}	1200	V
Typical $R_{DS(ON)}$	80	mΩ
I_D ($T_C \leq 100$ °C)	25	A

Circuit Diagram TO-247-3L

D (2, Tab)

G (1)

* Body diode

S (3)

1 2 3

Features

- Optimized for high-frequency, high-efficiency applications
- Extremely low gate charge and output capacitance
- Low gate resistance for high-frequency switching
- Normally-off operation at all temperatures
- Ultra-low on-resistance

Environmental

- Littelfuse "RoHS" logo = RoHS RoHS conform
- Littelfuse "HF" logo = **HF** Halogen Free
- Littelfuse "Pb-free" logo = Pb-free lead plating

Applications

- High-frequency applications
- Solar Inverters
- Switch Mode Power Supplies
- UPS
- Motor Drives
- High Voltage DC/DC Converters
- Battery Chargers
- Induction Heating

Maximum Ratings

Characteristics	Symbol	Conditions	Value	Unit
Continuous Drain Current	I_D	V_{GS} = 20 V, T_C = 25 °C	39	A
		V_{GS} = 20 V, T_C = 100 °C	25	
Pulsed Drain Current [1]	$I_{D(pulse)}$	T_C = 25 °C	80	A
Power Dissipation	P_D	T_C = 25 °C, T_J = 150 °C	179	W
Operating Junction Temperature	T_J		-55 to 150	°C
Gate-source Voltage	$V_{GS,MAX}$	Absolute maximum values	-6 to 22	V
	$V_{GS,OPTR}$	Transient, <1% duty cycle	-10 to 25	
	$V_{GS,OP}$	Recommended DC operating values	-5 to 20	
Storage Temperature	T_{STG}	-	-55 to 150	°C
Lead Temperature for Soldering	T_{sold}	-	260	°C
Mounting Torque	M_D	M3 or 6-32 screw	0.6	Nm
			5.3	in-lb

Footnote 1: Pulse width limited by $T_{J,max}$

Thermal Characteristics

Characteristics	Symbol	Value	Unit
Maximum Thermal Resistance, junction-to-case	$R_{th,JC,max}$	0.7	°C/W
Maximum Thermal Resistance, junction-to-ambient	$R_{th,JA,max}$	40	°C/W

Electrical Characteristics (T_J = 25 °C unless otherwise specified)

Characteristics	Symbol	Conditions	Min	Typ	Max	Unit
Static Characteristics						
Drain-source Breakdown Voltage	$V_{(BR)DSS}$	V_{GS} = 0 V, I_D = 250 µA	1200	-	-	V
Zero Gate Voltage Drain Current	I_{DSS}	V_{DS} = 1200 V, V_{GS} = 0 V	-	1	100	µA
		V_{DS} = 1200 V, V_{GS} = 0 V, T_J = 150 °C	-	2	-	
Gate Leakage Current	$I_{GSS,F}$	V_{GS} = 20 V, V_{DS} = 0 V	-	-	100	nA
	$I_{GSS,R}$	V_{GS} = -10 V, V_{DS} = 0 V	-	-	100	
Drain-source On-state Resistance	$R_{DS(ON)}$	I_D = 20 A, V_{GS} = 20 V	-	80	100	mΩ
		I_D = 20 A, V_{GS} = 20 V, T_J = 150 °C	-	105	-	
Gate Threshold Voltage	$V_{GS,th}$	V_{DS} = V_{GS}, I_D = 10 mA	1.8	2.8	4.0	V
		V_{DS} = V_{GS}, I_D = 10 mA, T_J = 150 °C	-	1.9	-	
Gate Resistance	R_G	f = 1 MHz, V_{AC} = 25 mV	-	1.0	-	Ω

Electrical Characteristics (T_J = 25 °C unless otherwise specified)

Characteristics	Symbol	Conditions	Value			Unit
			Min	Typ	Max	
Dynamic Characteristics						
Turn-on Switching Energy	E_{ON}	V_{DD} = 800 V, I_D = 20 A, V_{GS} = -5/+20 V, $R_{G,ext}$ = 2 Ω, L = 1.4 mH	-	270	-	μJ
Turn-off Switching Energy	E_{OFF}		-	60	-	
Total Per-cycle Switching Energy	E_{TS}		-	330	-	
Input Capacitance	C_{iss}	V_{DD} = 800 V, V_{GS} = 0 V, f = 1 MHz, V_{AC} = 25 mV	-	1825	-	pF
Output Capacitance	C_{OSS}		-	75	-	
Reverse Transfer Capacitance	C_{RSS}		-	15	-	
C_{OSS} Stored Energy	E_{OSS}		-	25	-	μJ
Total Gate Charge	Q_g	V_{DD} = 800 V, I_D = 20 A, V_{GS} = -5/+20 V	-	95	-	nC
Gate-source Charge	Q_{gs}		-	29	-	
Gate-drain Charge	Q_{gd}		-	39	-	
Turn-on Delay Time	$t_{d(on)}$	V_{DD} = 800 V, V_{GS} = -5/+20 V, I_D = 20 A, $R_{G,ext}$ = 2 Ω, R_L = 40 Ω, Timing relative to V_{DS}	-	10	-	ns
Rise Time	t_r		-	10	-	
Turn-off Delay Time	$t_{d(off)}$		-	16	-	
Fall Time	t_f		-	6	-	

Reverse Diode Characteristics

Characteristics	Symbol	Conditions	Value			Unit
			Min	Typ	Max	
Diode Forward Voltage	V_{SD}	I_S = 10 A, V_{GS} = 0 V	-	3.8	-	V
		I_S = 10 A, V_{GS} = 0 V, T_J = 150 °C	-	3.4	-	
Continuous Diode Forward Current	I_S	V_{GS} = 0 V, T_C = 25 °C	-	-	35	A
Peak Diode Forward Current [1]	I_{SP}		-	-	85	
Reverse Recovery Time	t_{rr}	V_{GS} = -5 V, I_S = 20 A, V_R = 800 V, dI/dt = 5.3 A/ns	-	25	-	ns
Reverse Recovery Charge	Q_{rr}		-	185	-	nC
Peak Reverse Recovery Current	I_{rrm}		-	16	-	A

Footnote 1: Pulse width limited by $T_{J,max}$

Figure 1: Maximum Power Dissipation (T$_J$ = 150 °C)
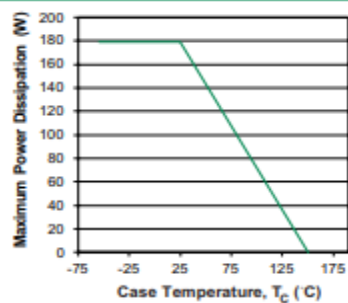
Figure 2: Transfer Characteristics (V$_{DS}$ = 10 V)
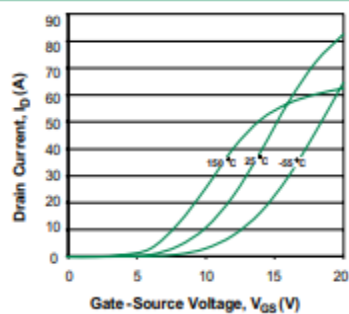
Figure 3: Output Characteristics (T$_J$ = 25 °C)
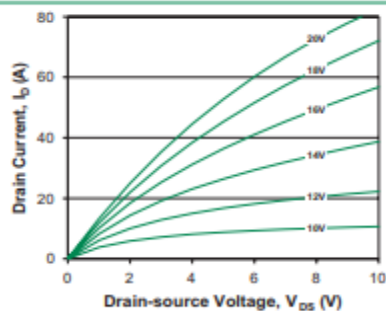
Figure 4: Output Characteristics (T$_J$ = 150 °C)
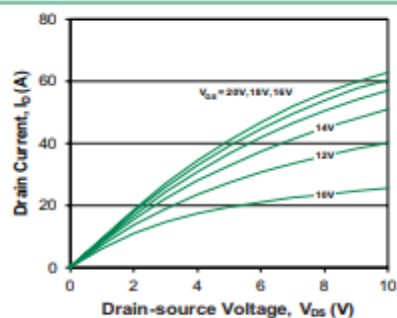
Figure 5: Output Characteristics (T$_J$ = -55 °C)
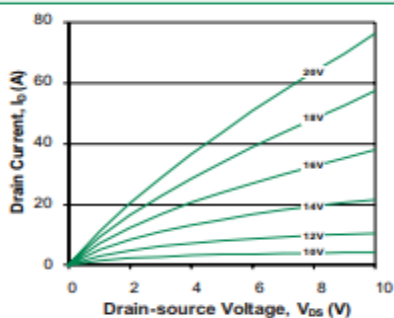
Figure 6: Reverse Conduction Characteristics (T$_J$ = 25 °C)
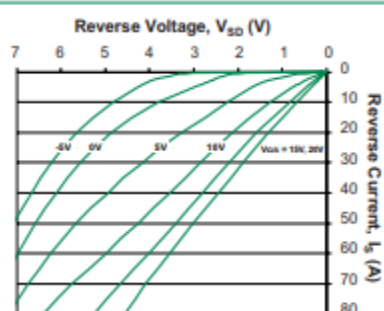
Figure 7: Reverse Conduction Characteristics (T_J = 150 °C)
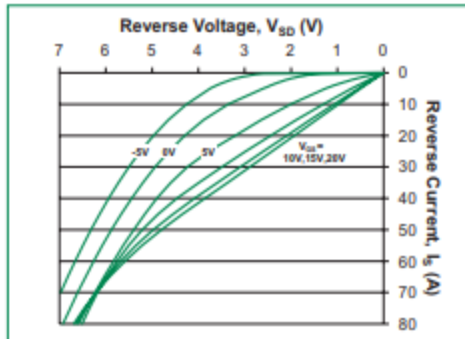
Figure 8: Reverse Conduction Characteristics (T_J = -55 °C)
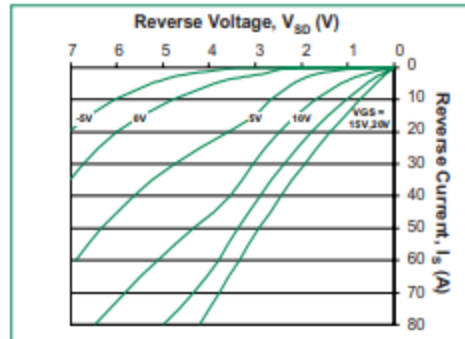
Figure 9: Transient Thermal Impedance
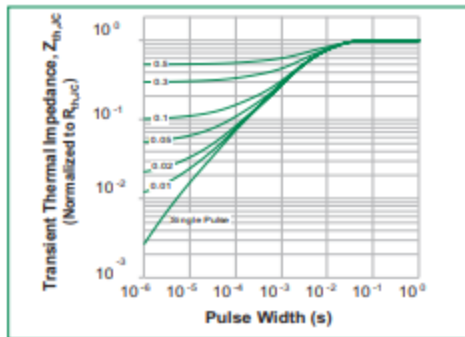
Figure 10: Safe Operating Area (T_C = 25 °C)
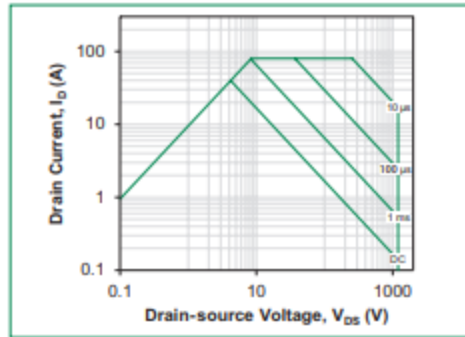
Figure 11: On-resistance vs. Drain Current
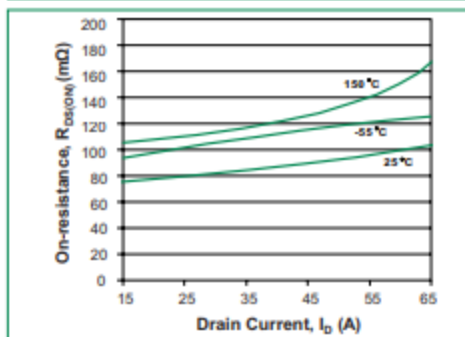
Figure 12: Normalized On-resistance
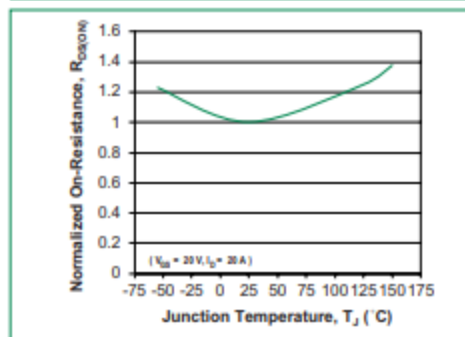
Figure 13: Threshold Voltage
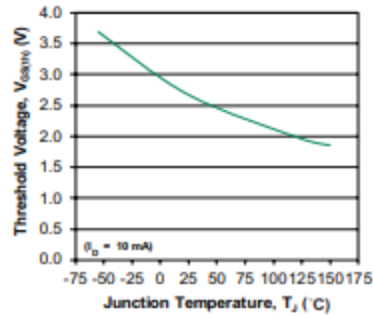
Figure 14: Drain-source Blocking Voltage
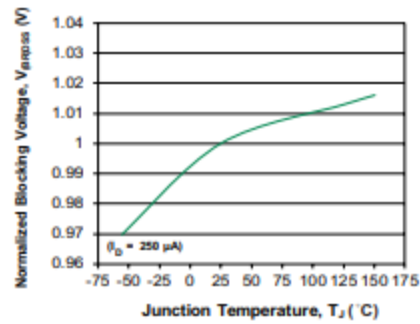
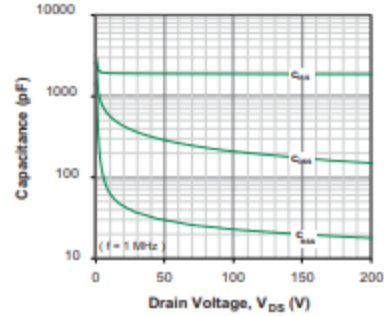**Figure 15: Junction Capacitances**
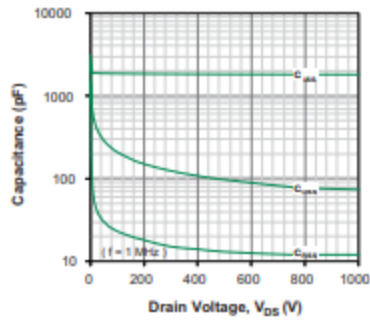
Figure 16: Junction Capacitances
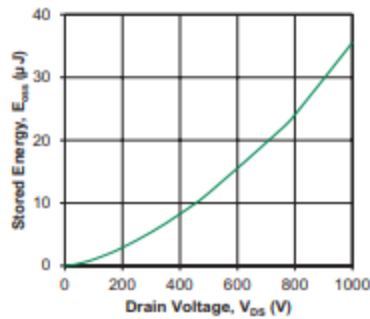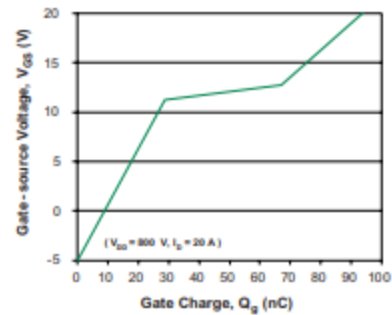

Figure 17: C_{OSS} Stored Energy E_{OSS}

Figure 18: Gate Charge
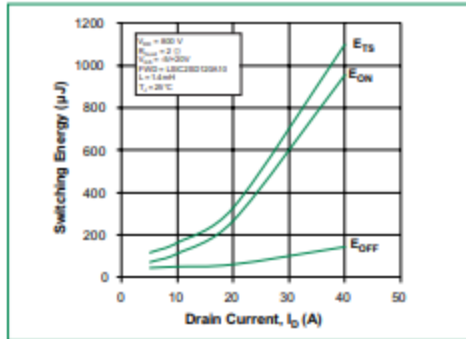
Figure 19: Switching Energy vs. Drain Current

Figure 20: Switching Energy vs. Gate Resistance
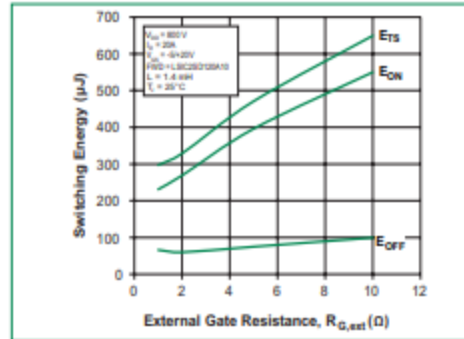
Package Dimensions TO-247-3L



BACK SIDE

SECTION C-C, D-D, E-E
NOT TO SCALE
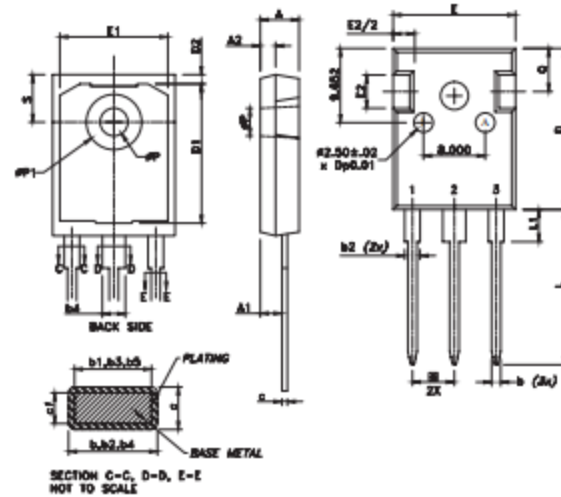
Recommended Hole Pattern Layout

UNIT: mm

Notes:
1. Dimensions are in millimeters
2. Dimension D, E do not include mold flash. Mold flash shall not exceed 0.127 mm per side measured at outer most extreme of plastic body.
3. øP to have a maximum draft angle of 38.1 mm to the top of the part with a maximum hole diameter of 3.912 mm.

Symbol	Millimeters		
	Min	Nom	Max
A	4.902	5.029	5.156
A1	2.253	2.380	2.507
A2	1.854	1.981	2.108
D	20.828	20.955	21.082
E	15.773	15.900	16.027
E2	4.191	4.318	4.445
E2/2	1.473	1.524	1.575
e		5.436	
L	20.066	20.193	20.320
L1	3.937	4.191	4.445
øP	3.556	3.067	3.658
Q	5.486	5.613	5.740
S	6.045	6.172	6.299
b	0.991	-	1.397
b1	0.991	1.199	1.346
b2	1.651	-	2.387
b3	1.651	1.999	2.336
b4	2.591	-	3.429
b5	2.591	3.000	3.378
c	0.381	0.635	0.889
c1	0.381	0.610	0.838
D1	17.399	17.526	17.653
D2	1.067	1.194	1.321
E1	13.894	14.021	14.148
øP1	7.061	7.188	7.315

Part Numbering and Marking System

SIC1MO120E0080
LF
YYWWD
ZZZZZZ-ZZ
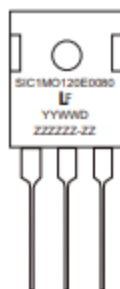
SIC	=	SiC
1	=	Gen1
MO	=	MOSFET
120	=	Voltage Rating (1200 V)
E	=	TO-247-3L
0080	=	R$_{DS(ON)}$ (80 mOhm)
YY	=	Year
WW	=	Week
D	=	Special Code
ZZZZZZ-ZZ	=	Lot Number

Packing Options

Part Number	Marking	Packing Mode	M.O.Q
LSIC1MO120E0080	SIC1MO120E0080	Tube	450

Packing Specification TO-247-3L

NOTE:

1. All pin plug holes are considered critical dimension
2. Tolerance is to be ±0.010 unless otherwise specified
3. Dimension are in inch (and millimeters).

Dual Channel SiC MOSFET Driver

Gate Driver for 1200V, 62mm SiC MOSFET Power Module

Features

- 2 output channels
- Integrated isolated power supply
- Direct mount low inductance design
- Short circuit protection
- Under voltage protection

For use with Cree Modules

- CAS300M12BM2, 1200V, 300A module.
- CAS120M12BM2, 1200V, 120A module.

Applications

- Driver for SiC MOSFET modules in industrial applications.
- DC Bus voltage up to 1000V

Part Number	Package	Marking
CGD15HB62P1	PCBA	CGD15HB62P1

Absolute Maximum Ratings

Symbol	Parameter	Value	Unit	Test Conditions	Note
V_s	Power Supply Voltage	16	V		
V_{iH}	Input signal voltage HIGH	5	V		
V_{iL}	Input signal voltage LOW	0	V		
$I_{O.pk}$	Output peak current	±9 (±2)	A	Gate drive capable of 9A, but 10Ω of gate resistance lowers peak to 2A	
P_{O_AVG}	Ouput power per gate	1.8	W		
F_{Max}	Max. Switching frequency	64	kHz		
V_{DS}	Max. Drain to source voltage	1200	V		
V_{isol}	Input to output isolation voltage	±1200	V		
dv/dt	Rate of change of output to input voltage	50,000	V/µs		

![CREE logo]

W	Weight	44	g		
MTBF	Mean time between failure	1.5×10^6	h		
T_{op}	Operating temperature	-35 to 85	ºC		
T_{stg}	Storage temperature	-40 to 85	ºC		

Characteristics

Symbol	Parameter	Value			Unit	Test Conditions	Notes
		Min	Typ	Max			
V_S	Supply voltage	14	15.0	16	V		
V_i	Input signal voltage on/off		5/0		V		
I_{SO}	Supply current (no load)		72		mA	25C	
	Supply current (max.)		300	360		f=64khz, 25C	
V_{iT+}	Input threshold voltage HIGH	3.5			V		
V_{iT-}	Input threshold voltage LOW			1.5	V		
R_{in}	Input resistance		48		kΩ		
C_{io}	Coupling capacitance		10		pf		
t_{don}	Turn on propogation delay		300		nS	Time from when input pin goes high until driver output goes high	Fig.3, 4
t_{doff}	Turn off propogation delay		300		nS	Time from when input pin goes low until driver output goes low	Fig.3, 4
t_{Rout}	Output voltage rise time		65		nS	V_{OUT} time from 10% to 90% with R_G = 0ohms, C_{LOAD} = 40,000pf	Fig. 5
t_{Fout}	Output voltage fall time		50		nS	V_{OUT} time from 90% to 10% with R_G = 0ohms, C_{LOAD} = 40,000pf	Fig. 5
R_{GON}	Turn-on gate resistor		10		Ω		
R_{GOFF}	Turn-off gate resistor		10		Ω		
V_{GATEON}	Gate voltage at turn-on		+20		V		
$V_{GATEOFF}$	Gate voltage at turn-off		-5		V		
t_{SC}	Short Circuit Response Time		1.5		µS	Total time from when short circuit current begins flowing until it is interrupted	
$V_{DS,TRIP}$	V_{DS} monitoring threshold		4.7		V	V_{DS} value that causes the driver to trip on overcurrent	
t_{FLT_DLY}	Fault Delay Time		425		nS	Time from when desat pin=9V until the gate output begins turning off	

114

CREE ⬧

t$_{FLT\_SIG}$	Transmission delay of fault state			2.25	µS	Time delay from desat pin=9V until fault status pin is pulled low	
t$_{err}$	Pulse width for resetting fault	800			nS	Time reset pin must be held low to reset driver	
	Test voltage (60Hz/1min), Primary to secondary		4000		V		
	Test voltage (60Hz/1min), Secondary to secondary		4000		V		
	Creepage distance, Primary to secondary		7.6		mm		
	Creepage distance, Secondary to secondary		6.7		mm		
	Clearance distance, Primary to secondary		4.0		mm		
	Clearance distance, Secondary to secondary		6.7		mm		

Block Diagram
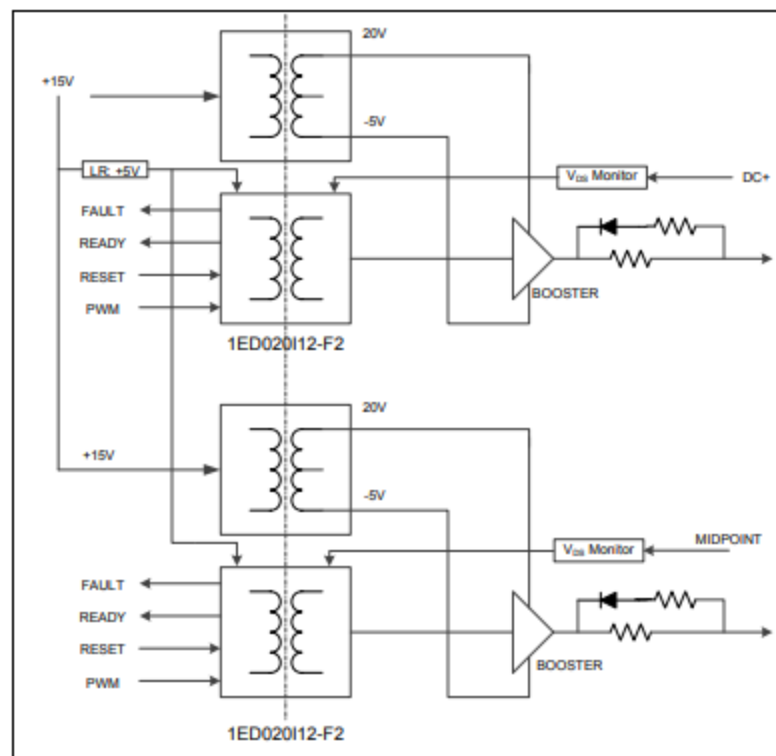
Figure 1. Block Diagram

115

CREE◆

Driver Interface
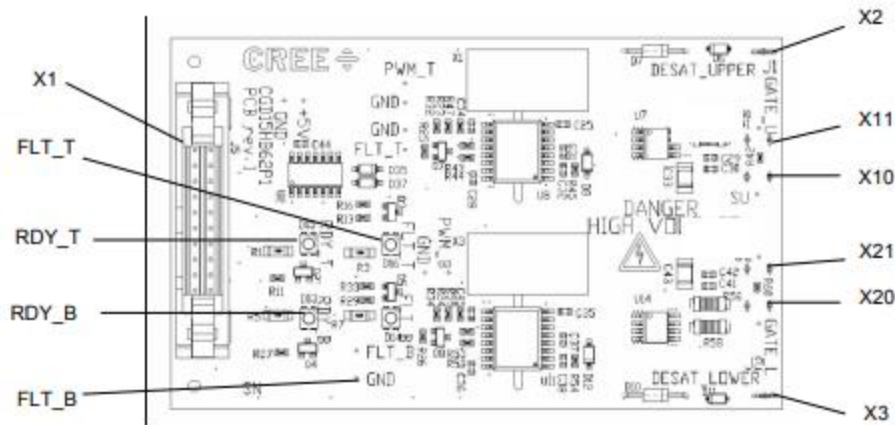
Figure 2. Top View

X1 – 20 pos connector (FCI p/n# 71918-120LF)

| 1	COMMON	2	GATE UPPER
3	COMMON	4	RESET UPPER
5	COMMON	6	READY UPPER
7	COMMON	8	FAULT UPPER
9	COMMON	10	GATE LOWER
11	COMMON	12	RESET LOWER
13	COMMON	14	READY LOWER
15	COMMON	16	FAULT LOWER
17	COMMON	18	VCC IN
19	COMMON	20	VCC IN
X2	Desat top switch connector	X3	Desat lower switch connector
LED Status Indicators			
FLT_T	Red LED illuminated indicates there is a fault on the top channel	**FLT_B**	Red LED illuminated indicates there is a fault on the bottom channel
RDY_T	Green LED illuminated indicates top channel is powered and ready	**RDY_B**	Green LED illuminated indicates top channel is powered and ready

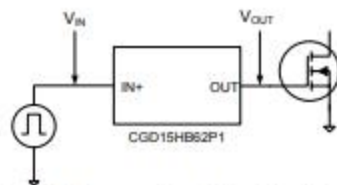116
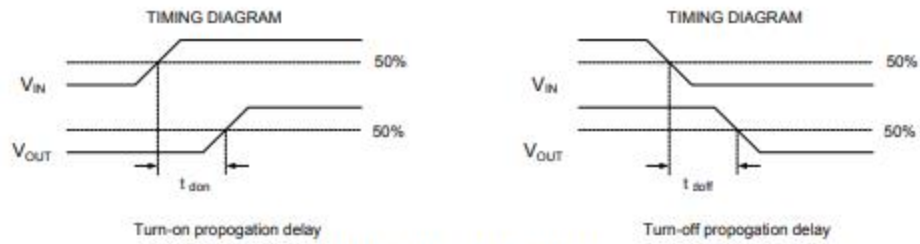
Figure 3. Propagation Delays

Figure 4. Propagation Delay Test Circuit

Figure 5. Output Voltage Rise and Fall Times

117

Mounting Instructions

Designed to directly mount to Cree 62mm style power modules. Four (4) mounting holes for 4x M4-8, Nylon screws are provided to secure the board to a bracket or enclosure (0.5 Nm) for additional support.

External wires with spade style connectors (part numbers listed below) should be used to connect the Desat detect pins (X2 & X3) from the module to the gate drive board.

Connectors (female) that fit Desat blade terminal
Right angle connector: TE Connectivity   61070-1
Straight connector: Molex   19002-0013

Figure 6. CGD15HB62P1 Mounted with Desat Connections

Top View

Side View
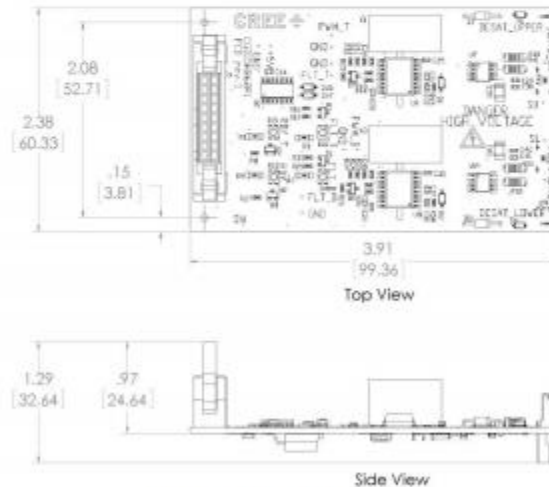
Mechanical Units: inches [mm]